Tuning Gas Adsorption and Separation Performances of ZIF-8 by [BMIM][PF_6] Incorporation

by

Fatma Pelin Kınık

A Thesis Submitted to the

Graduate School of Engineering

in Partial Fulfillment of the Requirements

for the Degree of

Master of Science

In

Chemical and Biological Engineering

Koç University

July 2017

Koç University

Graduate School of Sciences and Engineering

This is to certify that I have examined this copy of a master's thesis by

Fatma Pelin Kınık

and have found that it is complete and satisfactory in all respects,

and that any and all revisions required by the final

examining committee have been made.

Committee Members:

_____

Assoc. Prof. Seda Keskin Avcı (Advisor, Koç University)

_____

Asst. Prof. Alper Uzun (Advisor, Koç University)

_____

Prof. A. Levent Demirel (Koç University)

_____

Assoc. Prof. Uğur Ünal (Koç University)

_____

Prof. Ramazan Yıldırım (Boğaziçi University)

Date: _____

ABSTRACT

Natural gas which is mainly composed of CH_4 is a cleaner energy source with higher H/C ratio compared to fossil fuels. Natural gas is generally stored as compressed natural gas (CNG) and liquefied natural gas (LNG) to provide high densities of CH_4, however these storage techniques are expensive and unsafe. Moreover, natural gas has some impurities such as CO_2 and N_2 which may cause corrosion and low energy density. For an efficient gas storage and separation process, high capacity adsorbent materials have been used. Metal organic frameworks (MOFs) have drawn attention as porous adsorbent materials as a result of their remarkable structural characteristics, such as high surface area, high porosity, and low density as well good thermal and mechanical stability. To improve performances of MOFs, incorporation of ionic liquid (IL) into their structure has been suggested as a new approach.

In the first part of this thesis, an imidazolium-based IL ([BMIM][PF_6]) was incorporated into a MOF (ZIF-8) to investigate the effect of an IL incorporation on the gas adsorption and separation performance of a pure MOF. Gas adsorption measurements for CO_2, CH_4, and N_2 were performed in combination with atomically-detailed simulations and density functional theory (DFT) calculations. Results suggest that IL–MOF interactions strongly affect the gas affinity of materials at low pressure. Direct interactions between IL and MOF lead to at least a doubling of CO_2/CH_4 and CO_2/N_2 selectivities of ZIF-8. In the second part, five different phosphonium-based ILs ([P_{4444}][TOS], [P_{4441}][$MeSO_4$], [$P_{(14)666}$][TMPP], [$P_{(14)666}$][Br], and [$P_{(14)666}$][DCA]) were incorporated into ZIF-8 and [$P_{(14)666}$][DCA] was incorporated into CuBTC. The aim was to investigate the effect of different families of ILs and MOFs on the gas uptake and selectivity and extend the knowledge on IL/MOF composites. Similar performance measurements were conducted on these phosphonium-based IL/MOF composites. Results show that while phosphonium-based ILs could improve the gas capture performances of MOFs, none of them could increase selectivity of MOFs remarkably.

The results show that incorporation of IL into MOF structure is a promising way to improve the gas adsorption and separation performances of pure MOFs. With the help of the results obtained in this thesis study, it is possible to extend the number of IL/MOF composites prepared by using different kinds of ILs and MOFs, and they can be investigated for different gas separation applications.

ÖZET

Doğal gaz, temel olarak metandan oluşan ve yüksek H/C oranına sahip olan, fosil yakıtlara kıyasla daha temiz bir enerji kaynağıdır. Doğal gazın yüksek yoğunlukta depolanması amacıyla sıkıştırılmış doğal gaz (CNG) ya da sıvılaştırılmış doğal gaz (LNG) yöntemleri kullanılmakta, ancak bu yöntemler hem maliyetli hem de düşük güvenlikli olmaktadır. Doğal gaz, içerisinde CO_2 ve N_2 gibi safsızlıklar bulundurmakta ve asidik yapıdaki CO_2 korozyona ve düşük enerji yoğunluğuna neden olmaktadır. Ekonomik ve güvenli bir şekilde gaz depolama ve ayırma işlemlerinin gerçekleşebilmesi için yüksek kapasiteli adsorbent malzemeler kullanılmaktadır. Metal organik kafesli yapılar (MOFlar), yüksek yüzey alanı, yüksek gözeneklilik, düşük yoğunluk ve yüksek termal ve mekanik dayanklılık gibi özellikleri nedeniyle ilgi çeken, gözenekli adsorbent malzemelerdir. MOFların gaz depolama ve ayırma performanslarını geliştirmek için yapılarına iyonik sıvılar (ILler) katılması yeni bir yöntem olarak belirlenmiştir.

Bu tezin ilk kısmında, imidazolyum temelli bir IL ([BMIM][PF_6]), bir MOF'un (ZIF-8) içerisine katılmış ve IL ilavesinin MOF'un gaz yakalama ve ayırma performansı üzerine etkisi araştırılmıştır. Malzemelerdeki CO_2, CH_4 ve N_2 gazlarının adsorpsiyon miktarları ölçülmüş ve malzemelerin simülasyonları ve yoğunluk fonksiyonel teorisi (DFT) hesaplamaları yapılmışır. Sonuçlara göre IL-MOF arasındaki etkileşimler, malzemelerin gazlara olan ilgisini düşük basınçta etkilemektedir. IL-MOF arasındaki direkt etkileşimler, saf ZIF-8'in CO_2/CH_4 ve CO_2/N_2 seçiciliklerini en az iki katına çıkarmıştır. İkinci kısımda, 5 farklı fosfonyum temelli IL ([P_{4444}][TOS], [P_{4441}][$MeSO_4$], [$P_{(14)666}$][TMPP], [$P_{(14)666}$][Br], and [$P_{(14)666}$][DCA]) ZIF-8 içerisine, [$P_{(14)666}$][DCA] ise CuBTC içerisine katılmıştır. Amaç, farklı IL ve MOF ailelerinin gaz yakalama ve ayırma performansları üzerindeki etkisini araştırmak ve IL/MOF kompozit malzemeleri hakkındaki bilgi birikimini arttırmaktır. Aynı gas adsorpsiyonu ölçümleri, fosfonyum temelli IL/MOF kompozit malzemeleri için tekrarlanmıştır. Sonuçlar fosfonyum temelli IL'lerin MOF'ların gaz yakalama performanslarını arttırırken gaz ayırma performansları üzerinde önemli bir etkisi olmadığını göstermiştir.

Bu sonuçlar, MOF'ların yapısına IL'lerin katılmasının MOF'ların gaz yakalama ve ayırma performanslarını iyileştirdiğini göstermektedir. Bu çalışmadan elde edilen sonuçların yardımıyla değişik IL'ler ve MOF'lar kullanılarak IL/MOF kompozit malzemelerinin sayılarını arttırmak ve bu malzemeleri farklı gaz ayırma uygulamalarında kullanmak mümkündür.

ACKNOWLEDGEMENTS

First, I would like to express my sincere gratitude to my advisors Dr. Alper Uzun and Dr. Seda Keskin for their kind supervision and support. It has been a great chance for me to work with them and I am extremely grateful for their assistance and suggestions throughout my study. I owe special thanks to Dr. Ramazan Yıldırım, Dr. Levent Demirel, and Dr. Uğur Ünal for being my committee members and their valuable time.

This project is funded by Tübitak 1001 Program (project number: 114R093). I sincerely acknowledge the support from Koç University Seed Program, and Koç University-Tüpraş Energy Center (KÜTEM).

I am very thankful to Koç University Surface Science and Technology Center (KUYTAM) coordinators Barış Yağcı, Ceren Yılmaz Akkaya, Gülsu Şimşek, and Amir Motallebzadeh for their help in SEM, XRD, XRF, and BET measurements.

Being a member of NEMO and Uzun Lab has become one of the greatest things in my life. I had the opportunity to meet great people and create a strong bond of friendship. I would like to thank Çiğdem Altıntaş for her endless help, love, care, and support. I do not even want to think about how our office would be without her. I am also very thankful to her for the computational simulations in this thesis study. I would like to thank Burak Koyutürk that he has been a great friend and colleague for me since the beginning of my master's study. I would like to thank İlknur Eruçar for her help, moral support, and being a role model for me. I would like to also thank Zeynep Sümer, Vahid Nozari, Ayda Nemati, Özge Kadıoğlu, Derya Dokur, Elda Adatoz, and Muhammad Zeeshan for their great friendship and support. I am also very grateful to Benay Uzer, Onur Dereli, and Mert Bayer for spending great times with me in two years. I would also like to thank the members of Uzun Lab for their help, support, and friendship. I am very thankful to Volkan Balci for the DFT calculations in this thesis study. I am grateful to Ahsan Jalal and Melike Babucci for their limitless help and support in the laboratory.

My deepest gratitude goes to my family, Necmiye, Ali, and Aylin Kınık, for the support, sympathy, and love they showed me throughout my life. This study could not be completed without their guidance and understanding. I also would like to thank my boyfriend Arda Uran for supporting me in every case emotionally and intellectually.

TABLE OF CONTENTS

LIST OF TABLES

LIST OF FIGURES

NOMENCLATURE

BET: Brunauer–Emmett–Teller

GCMC: Grand canonical Monte Carlo

IL: Ionic liquid

MOF: Metal organic framework

COF: Covalent organic framework

N_i : Adsorbed amount for component i

Q_{st} : Isosteric heat of adsorption (kJ/mol)

SEM: Scanning electron microscope

STP: Standard temperature and pressure

TGA: Thermal gravimetric analysis

XRF: X-Ray Fluorescence

VOC: Volatile organic compound

DFT: Density Functional Theory

KBr: Potassium bromide

V_M: Molar volume

N_M: Monolayer capacity

S_{BET}: BET surface area

N_A: Avogadro number

MD: Molecular dynamics

CNT: Carbon nanotube

T_{onset} : Onset temperature (°C)

T'_{onset} : Derivative onset temperature (°C)

UFF: Universal force field

V_p : Pore volume (cm^3/g)

XRD: X-Ray Diffraction

ZIF: Zeolitic imidazolate framework

ε : LJ potential parameters (J/mol)

μ: Chemical potential (J/mol)

σ : LJ distance parameter (Å)

ρ_{cryst} : Crystal density (g/cm^3)

Chapter 1: Introduction

Fossil fuels, which are main energy sources in both industry and daily life, have been consumed much more rapidly with the growth of population and industrialization. Due to their existence in large amounts on the world and remarkable energy density, over 85% of the global energy need has been fulfilled by fossil fuels currently.[1] However, some environmental and health problems resulting from the hazardous by-products of combustion of fossil fuel such as gaseous pollutants (e.g. CO_2, SO_2, CO, and NO_x) occur increasingly.[2] In the light of these consequences, it is obvious that use of another energy sources is needed. Natural gas, which is composed of 80-95% CH_4 with impurities such as CO_2 and N_2, is a cleaner energy source with higher H/C ratio compared to fossil fuels.[3] It is generally stored as compressed natural gas (CNG) and liquefied natural gas (LNG) to provide high densities of CH_4. Storage of CH_4 in simple tanks requires large volume for high amounts of gases and high pressure to liquefy the gas which may cause safety issues. Moreover, acidic CO_2 in natural gas also causes corrosion and decreases energy density, therefore separation of CO_2 from CH_4 is also significant for improving the quality of natural gas. For these purposes, different methods including cryogenic distillation, membrane-, and adsorption-based gas separations have been studied. Because of its cost-effective and energy-saving nature, adsorption-based gas separation plays a key role in industry. Different adsorbent materials, such as zeolites, activated carbons, silica gels, carbon nanotubes (CNTs), and metal organic frameworks (MOFs) have been widely investigated in the literature in order to separate CO_2 from other gases.[4] Among these porous adsorbents, MOFs have been used extensively as promising alternatives to well-known adsorbent materials.

MOFs are crystalline nanoporous materials composed of metal-based building blocks linked by organic bridging ligands.[5] They have several advantageous structural and physical properties, such as high pore volumes (up to 2.3 cm^3/g), highly ordered pores ranging from micro- to the meso- scale, low densities (0.2-1 g/cm^3), large surface areas (up to 10,000 m^2/g), and acceptable thermal and mechanical stabilities.[6] Because of their interesting characteristics, MOFs have been examined for different kind of applications including gas separation,[5, 7] gas storage,[8-9], catalysis,[10-11] sensing,[12-14] drug delivery,[15] conductivity,[16-17] and biomedical imaging.[18] It is possible to create a large number of MOFs with different crystal structures and chemical properties by combining various metals and organic linkers, which make MOFs excellent alternatives compared to traditional porous materials such as zeolites.[5]

Several experimental studies have been carried out for adsorption-based gas separations using MOFs[5, 19-20] and results suggest that MOFs can replace traditional nanoporous adsorbents because of their higher adsorption selectivities. Recent studies focus on changing the structural features of MOFs, such as surface area, pore volume, and pore chemistry to improve their gas separation performances a step further. Tuning the porous structure of several types of MOFs has been widely investigated by using different methods, such as cation exchange,[21] metal substitution,[22] ligand exchange,[23-25] introducing various functional metals and organic linkers into the structure[26-29], and post-synthesis modification techniques.[30] However, enhancing gas selectivities of MOFs is a never-ending process and different methods are needed to make them preferable in industrial applications. It is possible to create stronger adsorption sites for certain gases by modifying MOFs and therefore their gas separation performances can be improved.[26-27, 29]

Lately, introducing ionic liquids (ILs) into the porous framework of MOFs have drawn attention to enhance both gas adsorption and separation performances of MOFs. ILs, composed of anions and cations, are salts that are liquid below 100 °C. By changing the combinations of these ions, approximately 10^{18} ILs with different characteristics can be obtained.[31] Their unique properties, such as high thermal stability, negligible volatility,

and non-flammability make ILs "green solvents" compared to the conventional organic solvents.[32] ILs have also remarkable ionic and thermal conductivity, chemical stability, and high affinity to certain gases. Therefore, they are desirable materials for several applications, such as chemical reactions, extractions, electrochemical devices (e.g. batteries, fuel cells, solar cells, and capacitors), gas absorption, and catalysis.[33-34] ILs especially have high CO_2 solubility compared to other gases, therefore they are promising materials to be combined with MOFs to increase CO_2 uptakes and selectivities of MOFs. Moreover, they can be used as cavity occupants in the pores of MOFs and their combination can be used for desired gas separation applications.[35] Based on these, IL-incorporated MOF composite materials (which will be denoted as "IL/MOF composites" in the following sections) have been recently studied in the literature as a new approach to enhance gas adsorption and selectivity of MOFs.

In this thesis, gas adsorption and separation performances of IL/MOF composites have been investigated using experimental and computational methods. Initially, one of the most studied commercially available MOFs in the literature, ZIF-8 (commercially available as Basolite® Z1200) has been characterized extensively and its CO_2, CH_4, and N_2 adsorption capacities were measured between 0.1-35 bar. ZIF-8 is a zeolite-type material with large pore size of 11.6 Å and narrow pore windows of 3.4 Å.[36] Having high surface area, porous framework structure, hydrophobic property, and water resistance make this material promising in gas separation and storage applications.[37] For studying the effect of IL incorporation, first a widely studied imidazolium based IL, 1-butyl-3-methylimidazolium hexafluorophosphate ([BMIM][PF_6]) was incorporated into ZIF-8 at a specified loading (30 wt%). [BMIM][PF_6] was selected as it is hydrophobic and one of the most commonly studied imidazolium-based ILs.[38] It is also known that $[PF_6]^-$ anion in the IL is a favorable site for CO_2.[39-40] Same characterization and gas adsorption experiments have been performed for [BMIM][PF_6]/ZIF-8 composite and effect of the IL impregnation on the gas adsorption and separation performances has been investigated. Moreover, effect of the interactions between IL and MOF on gas uptakes and selectivities of pristine ZIF-8 was elucidated. Then, five different phosphonium-based ILs were

incorporated into ZIF-8 and CuBTC (commercially available as Basolite® C300) to expand the knowledge about IL/MOF composites and different kinds of IL families. [P_{4444}][TOS]/ZIF-8, [P_{4441}][$MeSO_4$]/ZIF-8, [$P_{(14)666}$][TMPP]/ZIF-8, [$P_{(14)666}$][Br]/ZIF-8, [$P_{(14)666}$][DCA]/ZIF-8, and [$P_{(14)666}$][DCA]/CuBTC composites were prepared in the second part of this thesis study. Like ZIF-8, CuBTC have been extensively studied in the literature because of its promising features such as high surface area and high porosity. It has main channels (9 Å) and tetrahedral-shaped side pockets that are accessible through triangular windows (3.5 Å).[41] Different from ZIF-8, it has open metal centers which is promising for gas adsorption and hydrophilic nature. First, CuBTC has been characterized in deep detail and its CO_2, CH_4, and N_2 adsorption performances were investigated between 0.1-35 bar. Then, all characterization experiments and gas adsorption measurements were also done for each phosphonium-based IL/MOF composite.

In Chapter 2, a detailed literature review about MOFs, imidazolium-based ILs and phosphonium-based ILs, gas separation performances of these materials, and IL/MOF composites are given. The literature review about IL/MOF composites and their applications was published in *ChemSusChem* as a review paper.[42] In Chapter 3, experimental and computational techniques used in this study are provided. In Chapters 4 and 5, characterization experiments, gas uptake measurements and selectivities of imidazolium-based and phosphonium-based IL/MOF composites are presented, respectively. The results discussed in Chapter 4 were published in *ACS Applied Materials and Interfaces* as a research paper[43] and presented in *NanoTR-12* and *AIChE Annual Meeting 2016* conferences as oral presentations. Finally, outcomes of this thesis, challenges and opportunities are summarized in Chapter 6.

Chapter 2: Literature Review*

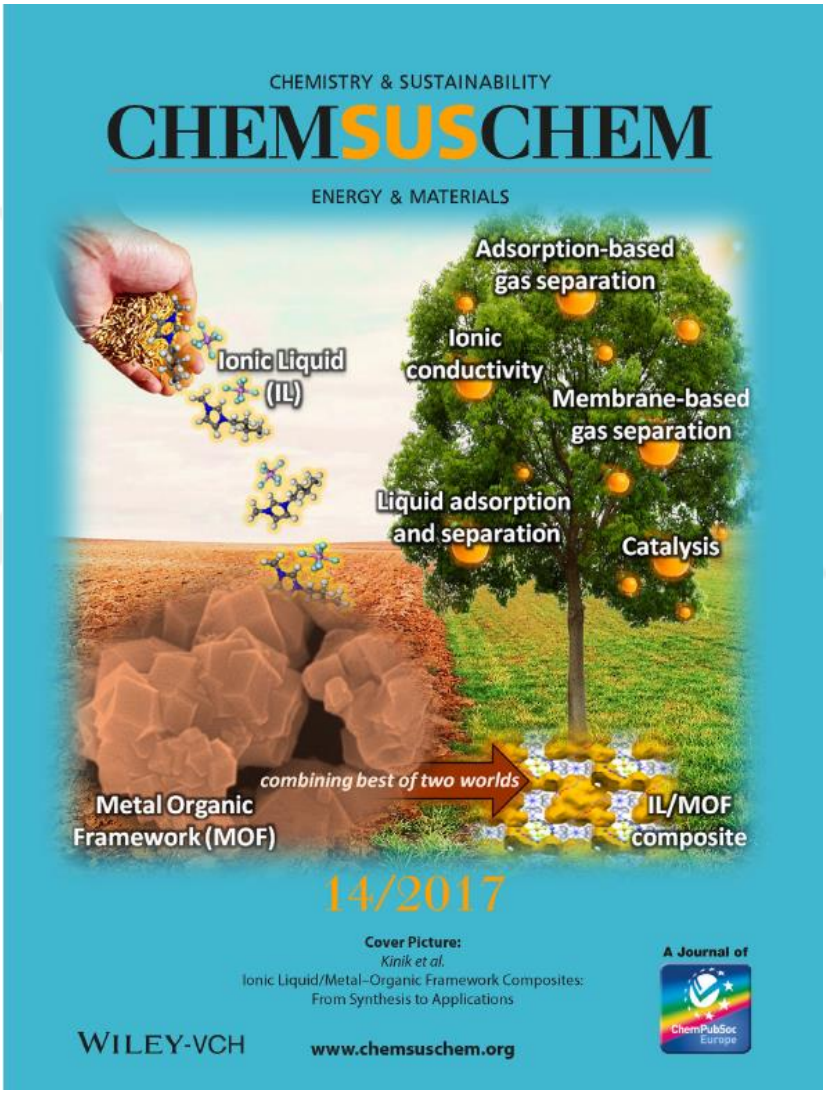

* The literature review about IL/MOF composites given in this chapter was published in ChemSusChem with following reference: Kinik, F. P.; Uzun, A.; Keskin, S., Ionic Liquid/Metal Organic Framework Composites: From Synthesis to Applications. ChemSusChem, **2017**, *10*, 1-23. This chapter is the reformatted version of the mentioned review paper. This paper has been selected as the cover picture to appear in Issue 14/2017 of ChemSusChem.

In this chapter, first structural properties, chemical characteristics of MOFs and their high potential for gas adsorption and separation applications are summarized. In the second part, the physicochemical properties and gas solubility in imidazolium-based and phosphonium-based ILs focusing on CO_2, CH_4, and N_2 gases are explained and their usage in gas separation applications is presented. Finally, utilization of ILs and MOFs together in different applications is covered and previous works related with IL incorporated MOFs are discussed.

2.1. Metal Organic Frameworks (MOFs) for Gas Adsorption and Separation

Because of the increasing consumption of fossil fuels, sustainability of oil reserves has drawn much more attention. As fossil fuels are more used, the CO_2 level in the atmosphere rises and it affects both environment and human health. Therefore, it is crucial to capture CO_2 as well as utilize cleaner fuel candidates such as natural gas and hydrogen (H_2).[44] Gases are generally stored in simple tanks, however it requires large volume for high amounts of gases and high pressure to liquefy the gas which may cause safety issues. The storage of gases in highly porous solids is a current technology which attracts great attention because of its advantages such as high storage density of gases, less safety problems because of the absence of high pressure requirements, and easiness of storing gases in a small amount of solid.[45] Highly porous materials such as zeolites, carbon materials, and polymers have suitable structural and chemical properties for the adsorption and storage of many different gases including CO_2 CH_4, N_2, and H_2. They have well-defined pore sizes, sufficient adsorption capacity, controllable delivery rates, suitable lifetimes, and recharging characteristics.[45] Porous materials are also used in gas separation applications. Among several gas separation techniques such as cryogenic distillation, absorption, and membrane-based separation, adsorption-based gas separation plays a key role in industry because of its cost effective, environmentally friendly, and energy-saving nature. For this process, adsorbent solids such as zeolites, activated

carbons, and silica gels with tailored structures and tunable surface properties have been studied extensively.[4]

Metal organic frameworks (MOFs) have recently appeared as promising alternatives to well-known nanoporous adsorbents because of their high porosities, large surface areas, low densities, good mechanical, and chemical stabilities.[46-48] MOFs are crystalline materials composed of metal cations connected by organic ligands.[5] The most attractive characteristic of MOFs over traditional nanoporous materials is the possibility of creating a large number of materials with different crystal structures and chemical compositions because of the ability to combine various metals and organic linkers.[5] Structural tunability and functionability make MOFs excellent alternatives compared to other porous materials, such as zeolites. Pores of zeolites are restricted by rigid tetrahedral oxide skeletons, therefore it is hard to modify these materials for specific applications, whereas the pore sizes and chemical functionalities of MOFs can be tuned to achieve a desired application.[6] The large versatility in chemical and physical properties of MOFs suggests that it is possible to find an ideal MOF adsorbent for a target gas adsorption and separation process. Several experimental studies have been carried out for adsorption-based CO_2 separations using MOFs[5, 19-20] and the results suggest that MOFs can replace traditional nanoporous adsorbents because of their higher adsorption selectivities. In addition to MOFs, covalent organic frameworks (COFs) have been also considered as promising materials in gas storage and separation applications.[49] COFs have light elements such as H, B, C, N, and O which form strong covalent bonds with each other.[50] COFs have lower densities than MOFs although they have similar characteristics with MOFs such as large surface areas, high pore volumes, and permanent porosity.[51]

2.2. Ionic Liquids (ILs) for Gas Separation

ILs have been also considered as novel materials offering great potential in gas separation applications similar to MOFs. ILs are molten salts in liquid form at low temperatures, usually below 100 °C. They are composed of large asymmetric organic

cations (e.g. imidazolium, pyrrolidinium, pyridinium, tetraalkyl ammonium or tetraalkyl phosphonium) and inorganic (e.g. Cl^-, PF_6^-, BF_4^-) or organic ($[CF_3SO_3]^-$, $[NTf_2]^-$, $[CF_3CO_2]^-$) anions.[52] It is possible to modify the physicochemical properties of ILs by changing the anion-cation pairs, therefore they are referred as "designer solvents".[53] Approximately 10^{18} different anion-cation combinations are possible for IL synthesis.[31] The most widely studied cations and anions of ILs can be seen in Figure 2.1.[54] Imidazolium-based and ammonium-based ILs have been the most studied ones among all ILs while phosphonium-based ILs have been less explored.[55] Therefore, it is important to extend the knowledge about this type of ILs to use them in different kinds of applications.

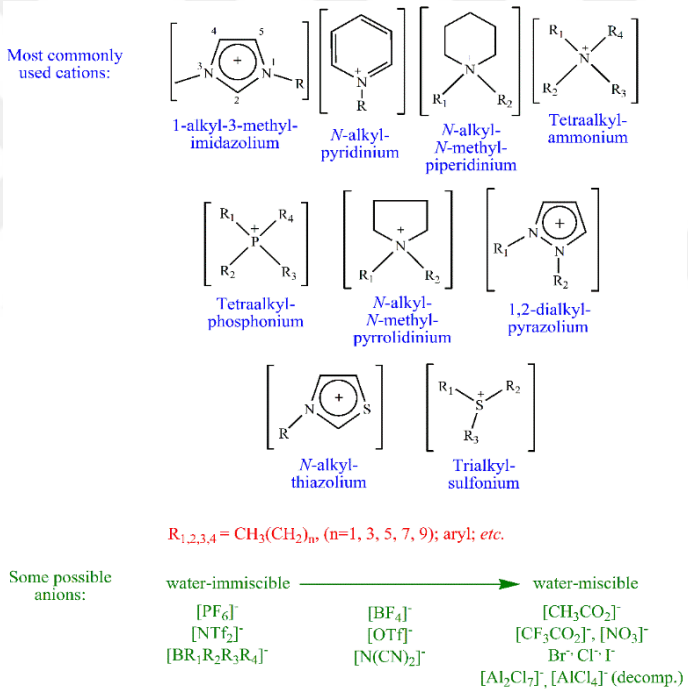

Figure 2.1. The most common anions and cations forming ILs.

Compared to the conventional organic solvents, ILs have more environmentally friendly production methods with many unique properties making them "green solvents". Especially because of their low vapor pressures, ILs have been used as alternative solvents to the volatile organic compounds (VOCs), which are traditional industrial

solvents and the major environmental pollutants.[56] Negligible volatility makes ILs evaporation-proof, resistant to combustion, and favorable for vacuum applications.[57] ILs are miscible with a wide range of organic and inorganic substances with different polarities. This is because while conventional solvents only have hydrogen bonding, dipole-dipole, and van der Waals interactions, ionic interactions (mutual electrostatic attraction or repulsion of charged particles) also exist in ILs which make them very miscible with polar substances.[58] Because of the strong electrostatic forces between the molecular ions of ILs, the most important features of the members of this family are their low volatility and high chemical and electrochemical stability, making them ideal solvents and electrolytes.[59] ILs also have remarkable affinity to certain gases, especially towards CO_2. Compared to CO_2, CH_4, and N_2 are significantly less soluble in ILs, therefore, they can be promising materials for separation of CO_2/CH_4 and CO_2/N_2 gas pairs.

2.3. Ionic Liquid-Incorporated MOFs

Tuning the porous structure of several types of MOFs to achieve high performance in a target process is very important. With this aim, different methods such as cation exchange,[20] metal substitution,[22] ligand exchange,[23-25] introducing various functional metals and organic linkers into the structure,[26-29] and post-synthesis modification techniques[30] has been widely studied. Although ILs have many advantageous properties by themselves which make their usage preferable in gas separation, their application is limited in real processes because of the liquid nature of ILs. For example, the packaging, portability, product purification, and recycling are the most important problems applications. Moreover, they have high viscosity and low diffusion coefficients which are also problematic. They can be confined into porous materials such as nanoporous silicas and carbons, MOFs, COFs, CNTs, and zeolites to overcome these drawbacks.[60]

The number of studies including MOFs and ILs has increased in the last decade as can be seen from Figure 2.2. Recent studies have focused on enhancing the structural and

functional features of MOFs by introducing ILs into the porous framework of MOFs. The most important advantage of MOFs among other porous materials is that their pore sizes/shapes and gas affinities can be tuned easily by varying organic linkers and metal complexes.[6] Therefore, combining ILs with MOFs is favorable for several applications, such as catalysis and gas adsorption/separation rather than using bulk ILs or other supported IL materials. Based on this objective, a novel technique called "IL incorporation in MOFs" aiming to combine the tunable physicochemical properties of ILs with MOF structures has been developed in the recent years.[60] The resulting materials will be referred as "IL/MOF composites" throughout this thesis study.

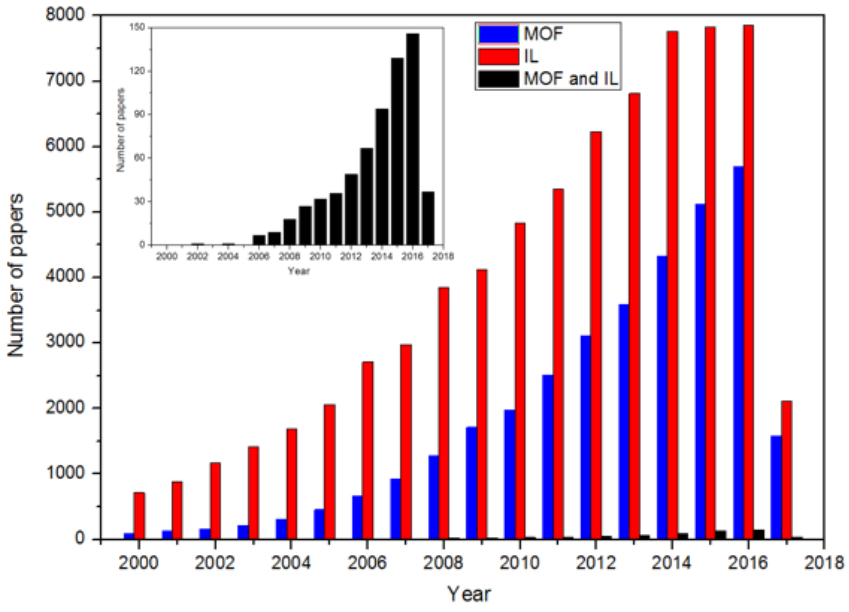

Figure 2.2. The number of publications featuring the terms "metal organic framework", "ionic liquid" and "metal organic framework AND ionic liquid" as a function of years. Source: Web of Science, accessed on 21st April, 2017.

IL/MOF composites have been explored computationally and experimentally in the fields of adsorption-based gas separation, membrane-based gas separation, liquid phase adsorption and separation, catalysis, and ionic conductivity in the last 6 years.[60] Table 2.1

shows the list of MOFs that have been experimentally and computationally investigated for IL incorporation to be used in different application areas. The unique characteristics of IL incorporation in MOFs are obtaining better adsorption and separation performance, higher conversion and reusability in catalytic applications, and remarkable ionic conductivity because of the combination of favorable properties of ILs and MOFs. Very recently, COFs have been also used as support materials for ILs. Therefore, there are a limited number of gas separation and catalysis applications of IL/COF composites in the literature.

Table 2.1. The characteristics of MOFs and COFs used for IL incorporation

MOF name	Chemical formula	Structure	Porosity and BET surface area	Ref
IRMOF-1	$Zn_4O(BDC)_3$ (MOF-5, BDC = 1,4-benzene dicarboxylate)	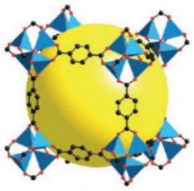	*Pore size:* 7.8 Å and 15 Å (pore limiting diameter) *Pore volume:* 1.22 cm^3/g *Surface area:* 2297 m^2/g	61-62
IRMOF-10	$Zn_4O(BPDC)_3$ (MOF-10, BPDC = 4,4'-biphenyl dicarboxylate)	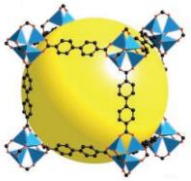	*Pore size:* 16.7 Å (largest cavity diameter) and 20.2 Å (pore limiting diameter) *Pore volume:* 2.62 cm^3/g *Surface area:* 4991 m^2/g	63-65
CuBTC	$Cu_3(BTC)_2$ (HKUST-1 or MOF-199, BTC = 1,3,5-benzene tricarboxylate	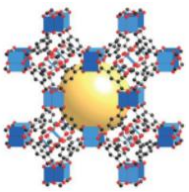	*Pore size:* Main channels (9 Å) and tetrahedral side pockets (5 Å) accessible through triangular windows (3 Å) *Pore volume:* 0.75 cm^3/g *Surface area:* 2175 m^2/g	41, 66-67

ZIF-8	$Zn(MeIM)_2$ (MeIM = imidazolate-2-methyl)	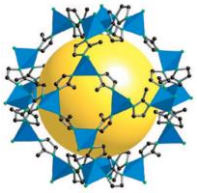	*Pore size:* Large cavities (11.6 Å) connected through small apertures (3.4 Å) *Pore volume:* 0.66 cm^3/g *Surface area:* 1947 m^2/g	68
NH_2-MIL-101(Cr)	$[Cr_3O(X)(H_2O)_2(BDC\text{-}NH_2)_3]\cdot nH_2O$ (BDC = 1,4-benzene dicarboxylate, X= F or OH, n~25)	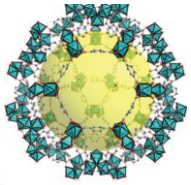	*Pore size:* Two monodispersed pore sizes with 15.4 and 19.9 Å *Pore volume:* 2.26 cm^3/g *Surface area:* 2070 m^2/g	69-71
MIL-101(Cr)	$[Cr_3O(X)(H_2O)_2(BDC)_3]\cdot nH_2O$ (BDC = 1,4-benzene dicarboxylate, X= F or OH, n~25)	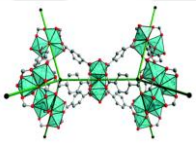	*Pore size:* Inner free cage diameters up to 34 Å and pore aperture windows up to 16 Å *Pore volume:* 1.68 cm^3/g *Surface area:* 4000 m^2/g	72
UiO-66	$[Zr_6O_4(OH)_4(BDC)_6]$ (BDC = 1,4-benzene dicarboxylate)	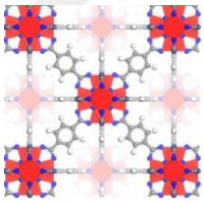	*Pore size:* 12 Å (octahedral cage) and 7.5 Å (tetrahedral cage) *Pore volume:* 0.43 cm^3/g *Surface area:* 969 m^2/g	73
UiO-67	$[Zr_6O_4(OH)_4(BPDC)_6]$ (BPDC = biphenyl dicarboxylate)	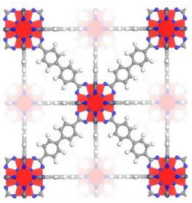	*Pore size:* 16 Å (octahedral cage) and 12 Å (tetrahedral cage) *Pore volume:* 0.85 cm^3/g *Surface area:* 1877 m^2/g	73

Cu-TDPAT	Cu_3(TDPAT)$(H_2O)_3]\cdot 10H_2O\cdot$ 5DMA (TDPAT = 2,4,6-tris(3,5-dicarbonylphenyl amino)-1,3,5-triazine)	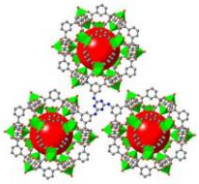	*Pore size:* 17.2 Å (octahedral cage) and 9.1 Å (tetrahedral cage) *Pore volume:* 0.93 cm^3/g *Surface area:* 1938 m^2/g	73
MOF-74(Mg)	Mg_2(DOBDC) (DOBDC = 2,5-dihydroxyl benzene dicarboxylic acid)	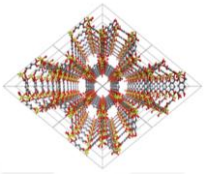	*Pore size:* 1-D hexagonal channels of single type pores (11 Å) *Pore volume:* 0.62 cm^3/g *Surface area:* 1525 m^2/g	74
ZIF-71	$Zn(DCIM)_2$ (DCIM = 4,5-dichloro imidazolate)	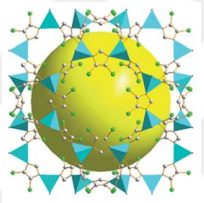	*Pore size:* 5.4 Å (pore limiting diameter) and 17 Å (largest cavity diameter) *Pore volume:* 0.36 cm^3/g *Surface area:* 679 m^2/g	62, 75
Na-rho-ZMOF	$[(Na^+)_{48}][In_{48}$(HIMDC$)_{96}]$ (IMDC = imidazole-4,5-dicarboxylic acid)	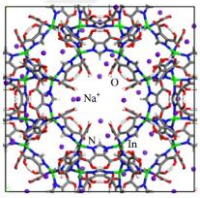	*Pore size:* 5.6 Å (window diameter) and 18.2 Å (largest cavity diameter) *Pore volume:* 0.34 cm^3/g *Surface area:* 816 m^2/g	76-78
MIL-100(Fe)	$(Fe_3F(H_2O)_2O[C_6H_3(CO_2)_3]_2\cdot nH_2O$	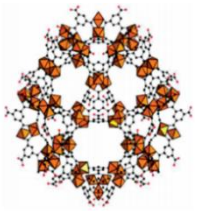	*Pore size:* Mesoporous cages (25 and 29 Å) accessible through microporous windows (5.5 and 8.6 Å) *Pore volume:* 0.79 cm^3/g *Surface area:* 1626 m^2/g	79-80
ZIF-90	$Zn(ICA)_2$ (ICA= imidazolate-2-carboxy aldehyde)	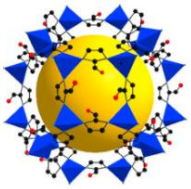	*Pore size:* 3.5 Å (pore limiting diameter) and 11 Å (largest cavity diameter) *Pore volume:* 0.40 cm^3/g *Surface area:* 1214 m^2/g	62, 81

COF-320	$C_{53}H_{36}N_4$	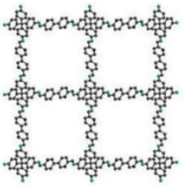	*Pore size:* 1D rectangular channels with an aperture size of 13.5 x 6.2 Å *Pore volume:* 0.81 cm^3/g *Surface area (Langmuir):* 2400 m^2/g	82-83

2.3.1. Synthesis of IL/MOF Composites

IL/MOF composites were first prepared using the ionothermal synthesis method in the literature. This method is based on utilization of ILs as both solvent and template or structure directing agent in the synthesis of solid materials (e.g. zeolites and MOFs).[84] For ionothermal synthesis, first precursors of a MOF are dissolved in an IL and the mixture is sealed inside a Teflon-lined stainless-steel autoclave. Then, the mixture is put into a furnace and treated at a specified temperature for couple of days. Finally, it was cooled to ambient temperature and crystals are collected.[85] Initial studies using this method were not successful in terms of incorporation of bulk ILs into MOFs. When the first two dimensional coordination network structure, [Cu(I)(bbp)][BF_4] was synthesized using [BMIM][BF_4], the [BF_4]$^-$ anions were incorporated into the coordination polymer as charge-compensating species and [BMIM]$^+$ cations remained in the solution.[86] Similarly, large channels of the MOF were filled with only [BF_4]$^-$ anions in the synthesis of [$Cu_3(tpt)_4$](BF_4)$_3$.$(tpt)_{2/3}$.5H_2O from an IL medium, [BMIM][BF_4].[87] Other research groups also reported that ionothermally synthesized MOFs contain mostly cation parts of ILs in the frameworks.[84, 88-89] The frameworks of ionothermally synthesized MOFs are generally negatively charged, therefore cations of ILs remain in the structure as counter ions to provide electrical neutrality. However, cations are not able to show the same properties with the bulk ILs which is an disadvantage of this method.[90] This method has another drawback, the number of MOFs that can be synthesized ionothermally is limited.[90]

In order to eliminate the problems in ionothermal synthesis, a strategy called post-synthesis impregnation in which ILs are impregnated into the porous structure after the synthesis of MOFs has been developed. With this method, IL/MOF composites having different characteristics and performances can be obtained by changing the components. Post-synthesis impregnation of ILs inside the cavities of synthesized MOFs can be achieved using different ways, such as wet impregnation, capillary action, and ship-in-a-bottle methods. Schematic representations of post-synthesis impregnation methods can be seen in Table 2.2.

2.3.1.1. Wet Impregnation Method

The most widely used post-synthesis impregnation method is wet impregnation. In this method, ILs are first dissolved in the excess amount of an inert solvent, such as acetone, methanol, or ethanol to provide better dispersion. MOF is then added to the solution and the mixture is stirred at ambient temperature for a couple hours. After having a homogenous solution, the solvent is removed and IL/MOF composite in the form of a powder is obtained. Several studies used this strategy to prepare IL/MOF composites for adsorption/separation and catalysis applications.[43, 91-105]

2.3.1.2. Capillary Action Method

In this post-synthesis impregnation strategy, IL and MOF are directly mixed without using a solvent. MOF is first dried to remove all impurities from the pores before being mixed with the IL. Then, two materials are mixed using a mortar and a pestle at a certain volumetric occupancy ratios. In order to ensure better diffusion of IL into the pores of the MOF, resulting sample is heated overnight and then resulting powder is stored. There are several IL/MOF studies in the literature utilizing this technique.[106-110]

2.3.1.3. Ship-in-a-bottle Method

Another post-synthesis impregnation method is called "ship-in-a-bottle" process, where ILs are synthesized in the pores of MOFs.[111-114] For the synthesis, small precursors of ILs (ship) are diffused into the pores of MOF (bottle) after dissolving in a solvent. They are allowed to react within the cages of MOF, ending up with the formation of bulk ILs trapped inside the pores. Finally, unreacted precursors of IL are removed from the surface of MOF using a solvent and IL/MOF composite is obtained after drying process. With this method, ILs can be trapped inside the cavities because the synthesized IL is generally larger than the pore apertures of the MOF.[112]

Table 2.2. Schematic representations of different post-synthesis impregnation methods used in the synthesis of IL/MOF composites

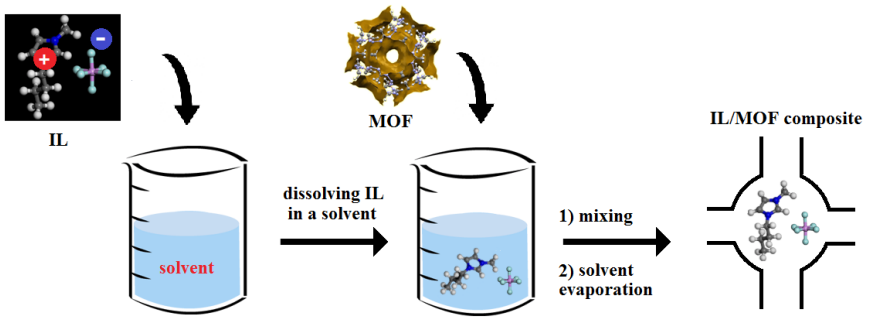	Wet-impregnation method

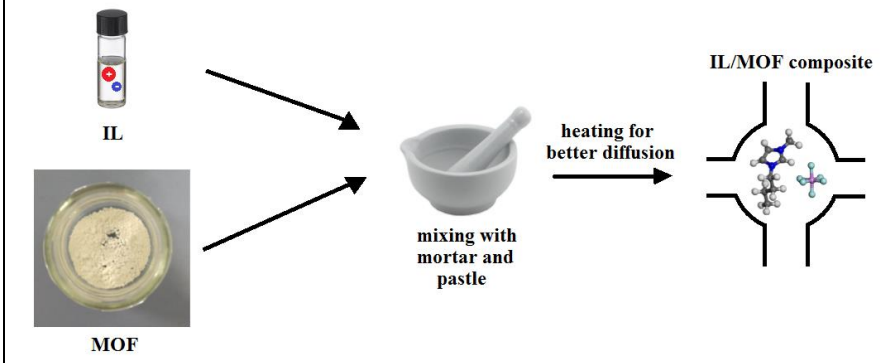	Capillary action method
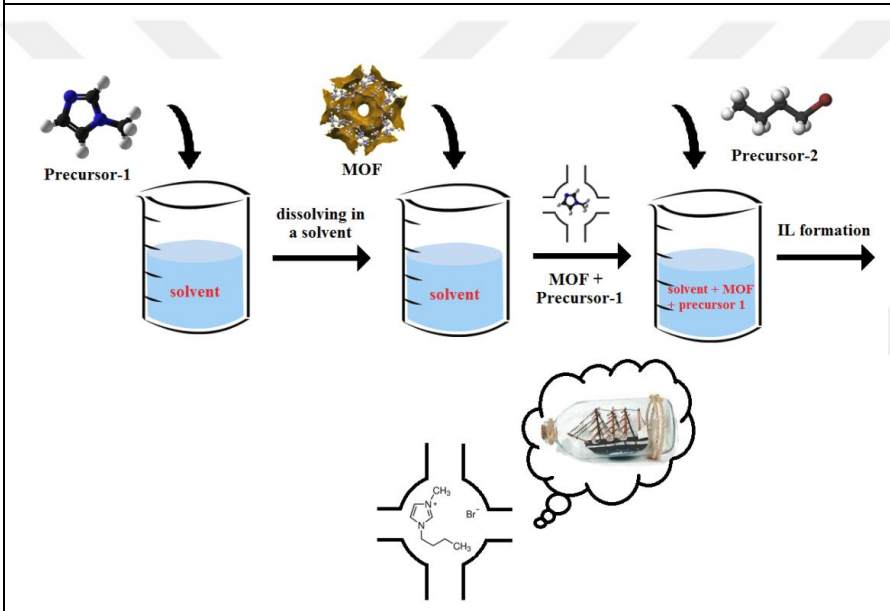	Ship-in-a-bottle method

2.3.2. Investigation of IL-MOF Interactions in the Composites:

It is important to understand the effects of IL incorporation into the MOF pores on the properties and performances of MOFs. For this purpose the key point is the elucidation of interactions between ILs and MOFs and their consequences on the performance of the resulting material. If these interactions are clearly examined and their effects on the performance can be elucidated, the rational design of IL/MOF composites can be possible by finding promising IL-MOF pairs for a desired application. IL-MOF

interactions were studied both computationally and experimentally. Different amounts of [BMIM][PF_6], [BMIM][Br], [BMIM][Tf_2N], [BMIM][DCA], and [BuPy][Tf_2N] were loaded into IRMOF-1 and IRMOF-10 (isoreticular, having the same topology) using molecular dynamics (MD) simulations to investigate the structural stability of the MOFs in the presence of ILs.[115] It was found that impregnation of all ILs made both IRMOFs structurally unstable and deformation occurred in their crystal structures. Molecular simulations were supported by the density functional theory (DFT) calculations which showed that the interactions between IL anions and Zn atoms of IRMOFs cause the collapse of the frameworks. It was concluded that IRMOFs are not suitable host materials for ILs. Another computational study[116] incorporated different ILs consisting of $[BMIM]^+$ cation and four different anions ($[Tf_2N]^-$, $[PF_6]^-$, $[BF_4]^-$, and $[SCN]^-$) into IRMOF-1 to investigate the microscopic properties of ILs in IRMOF-1. They concluded that anion has a stronger interaction than the cation with IRMOF-1. However, the stability of IRMOF-1 after IL incorporation was not further investigated. In a different study, the interactions between [EMIM][$EtSO_4$] and CuBTC were investigated using FTIR and Raman spectroscopies complemented by DFT calculations.[108] It was observed that interionic interactions become stronger because $[EtSO_4]^-$ anion of IL interacts with the Cu sites of the MOF and direct interactions present between the IL's imidazolium ring with either MOF or the anion of IL. Two IL ion-pair configurations in the pores of MOF were observed: for the first configuration, interionic interactions between the anion and cation of IL were enhanced based on the strengthened hydrogen bonds while the second ion-pair configuration caused a weakening in the interactions. DFT calculations showed that charge-transfer or redistribution of electron density was the reason of the interactions between the IL and MOF.

The studies reviewed above proved that it is important to achieve a fundamental level understanding on how the incorporation of IL physically and chemically affects the MOF. Only after achieving this understanding, rational design of these novel materials can be possible. With this aim, we[43] recently investigated an IL/MOF composite prepared by incorporating [BMIM][PF_6] into ZIF-8. FTIR data indicated that IL interacts with the

MOF through its anion by sharing electrons with the imidazole ring in ZIF-8. These observations were supported by DFT calculations illustrating that $[PF_6]^-$ anion prefers to locate itself parallel to an imidazolium ring of the ZIF-8 framework. According to the TGA experiments, IL/MOF composite started to decompose at a lower temperature compared to that of pristine ZIF-8 and bulk IL showing that there is a different decomposition mechanism after IL incorporation. Moreover, remaining mass was less than expected at the end of the analysis. These results proved the interactions between [BMIM][PF_6] and ZIF-8.

2.4. IL/MOF Composites in Adsorption-Based Gas Separation

Among the studies considering the IL/MOF composites, majority of them focus on gas adsorption and separation applications. Several gas storage and gas separation studies have been conducted using MOFs[4, 8-9, 20, 48, 117-119] to achieve the desired storage limits and high selectivities. Solubility of different gases (especially CO_2) in ILs have widely been investigated in the literature.[120] A unit operation named as "adsorptive absorption" was proposed for investigating the gas capture performances of ILs after the addition of MOFs into ILs.[121] Here, it is important to note that in these studies ILs are not incorporated into MOFs but molecular simulations were used to predict the solubility and adsorption of gases (CO and CO_2) in ILs and MOFs, respectively. Experiments were conducted to measure the gas solubility in bulk ILs and IL-MOF mixtures which were prepared by dispersing MOFs into the liquid phase and explore the effect of MOF suspension on the gas capture of ILs. Results showed that the addition of MOF into IL can remarkably increase the solubility of CO and CO_2.[149,150]

The new approach to obtain better performing MOFs for gas storage and gas separation is to incorporate ILs as guest molecules into MOFs' pores and hence to tune the gas affinity of MOFs. With the introduction of IL into MOF cavities, the porosity of MOF can be tuned, new adsorption sites can be created and/or molecular sieve property of MOFs can be enhanced.[97] The separation performances of IL/MOF composites are

generally quantified using selectivity, which is the ratio of adsorbed amounts of gas components. Considering the very large numbers of available MOFs and ILs, it is possible to find ideal IL/MOF composites that can achieve high selectivity for a desired gas separation.

2.4.1. Experimental Studies

The first experimental gas adsorption study of an IL/MOF composite was conducted in combination with the Monte Carlo simulations to improve the CO_2 storage capacity of a MOF with IL incorporation.[97] Two different ILs ([BMIM][PF_6] and [BMIM][Tf_2N]) were experimentally impregnated into CuBTC at different concentrations (1, 5, and 10 wt%). Experimental adsorption measurements on [BMIM][PF_6] and [BMIM][Tf_2N]/CuBTC samples showed that IL incorporation does not help to exceed the CO_2 uptake of pure CuBTC which was explained by the defects on the structure with the high loading of IL, yet there was no direct evidence from the characterization studies.

Our research group[93] used the same MOF, CuBTC but a different IL, [BMIM][BF_4]. 5, 20, and 30 wt% of [BMIM][BF_4] was impregnated into MOF cavities. None of the [BMIM][BF_4]/CuBTC samples could outperform the CO_2, CH_4, N_2, and H_2 adsorption capacities of pure CuBTC because of the reduced pore volume. Ideal adsorption selectivities, which is the ratio of adsorbed amount of single-component gases, were calculated for CO_2/CH_4, CO_2/N_2, CO_2/H_2, CH_4/N_2, CH_4/H_2, and N_2/H_2 separations and the highest enhancement was achieved for CH_4/H_2 selectivity at low pressures with an IL loading of 30 wt% as shown in Figure 2.3. For instance, at 0.2 bar the corresponding selectivity increased from 26 to 56 upon IL incorporation at 30 wt%. Other gas selectivities (CO_2/H_2, CH_4/N_2, and N_2/H_2) were also improved between 0.1-1 bar after IL incorporation.

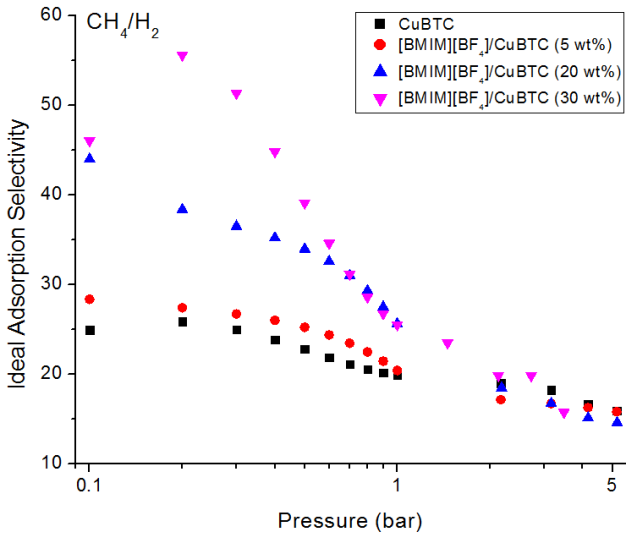

Figure 2.3. Ideal adsorption selectivities of [BMIM][BF_4]/CuBTC samples for CH_4/H_2 separation at room temperature up to 5 bar.[93]

A similar study was conducted by Ban et al.[97] that IL was used to tailor the molecular sieving property of the MOF by tuning the nanocages. An improvement in the CO_2 uptake with IL incorporation was reported for the first time in the literature whereas the uptake amounts of N_2 and CH_4 in [BMIM][Tf_2N]/ZIF-8 composite decreased because of the decreased pore volume. Unsurprisingly, CO_2/N_2 and CO_2/CH_4 gas separation performances were significantly improved, which were reported to be approximately 5 times more than those of pristine ZIF-8. These results were attributed to the good solubility of CO_2 in [BMIM][Tf_2N] and high molecular sieving property of IL/MOF composite.

A task specific ionic liquid (TSIL), [C_3NH_2BIM][Tf_2N] was impregnated in NH_2-MIL-101(Cr).[96] CO_2 and N_2 uptakes in TSIL/NH_2-MIL-101(Cr) composite decreased as a result of the reduced pore volume supporting the previous findings. Because of the existence of imidazolium ring, $[Tf_2N]^-$ anion and amine groups, [C_3NH_2BIM][Tf_2N] has an excellent CO_2 affinity, therefore the decrease in N_2 uptake is higher than that of CO_2 at lower pressures. The CO_2/N_2 selectivity of TSIL/MOF composite was reported to be

almost 2 times more than that of pristine MOF. This composite was used in MMM as a filler particle.

Very recently, our group performed a work by impregnating [BMIM][BF_4] into ZIF-8 MOF at different loadings.[101] Single-component gas adsorption isotherms (CH_4, CO_2, and N_2) were experimentally and computationally measured for 4, 20, and 28 wt% IL loaded composite materials. The composite with 20 wt% IL loading showed 9% higher CO_2 uptake than that of pure ZIF-8 at 0.1 bar. CO_2/CH_4, CO_2/N_2, and CH_4/N_2 selectivities were also increased from 2.2, 6.5, and 3 to 4, 13.3, and 3.4, respectively with 28 wt% IL loading. Q_{st} values elucidated that the change in Q_{st} of CO_2 with IL incorporation was more apparent compared to other gases, resulting in enhanced CO_2 selectivities. However, as the pressure increased, the dominant factor became the available pore volume.

Recently, a bifunctional IL/MOF composite was prepared for selective CO_2 adsorption and separation over N_2 and CH_4.[122] CO_2 uptake for IL/UiO-67 (22.4 cm^3/g) composite was obtained as the same with that of pristine UiO-67 (22.9 cm^3/g) while CH_4 and N_2 uptakes were much lower than that of pristine UiO-67. The selectivities for equimolar CO_2/CH_4 and CO_2/N_2 mixtures were calculated by fitting the single-component adsorption isotherms of gases and using the Ideal Adsorbed Solution Theory (IAST). Results showed that selectivities for IL/UiO-67 were 7.6 and 381.4, respectively. It must be noted that exceptionally high CO_2/N_2 selectivity may be originated from the uncertainties of the IAST. The same material was also used as a catalyst for the chemical transformation of CO_2 to cyclic carbonates.

2.4.2. Computational Studies

Thousands of MOFs have been synthesized over the years, however choosing the appropriate MOF for the desired application is still very challenging because it is not possible to measure the performances of all available MOFs using purely experimental manners.[123] Similarly, a large number of ILs with different properties has been synthesized using different cations and anions. Computational studies have an important

role to identify the most promising IL-MOF pairs among thousands of possible combinations for the desired processes and to direct the experimental efforts, time, and resources to those promising composites. Majority of the initial studies on IL/MOF composites were computational in nature as briefly discussed below.

Chen et al.[124] conducted the first computational work on an IL/MOF composite in the literature to explore the structure and dynamics of IL in the MOF. CO_2 capture and CO_2/N_2 gas separation performance of the resulting material were investigated using molecular dynamics (MD) and GCMC simulations. At low pressures, CO_2 adsorption was enhanced compared to pure IRMOF-1 because of the presence of IL in the pores. However, the free volume in IRMOF-1 decreased with the IL addition and this affected the gas capture performance of [BMIM][PF_6]/IRMOF-1 negatively at high pressures. CO_2 was especially preferred by the $[PF_6]^-$ sites, and thus, it was adsorbed more than N_2 in [BMIM][PF_6]/IRMOF-1. Higher CO_2/N_2 selectivities were observed for IL/IRMOF-1 compared to pristine IRMOF-1 at all IL loadings and as the loading increased, separation performance became better.

It is known that anion governs the gas solubility of IL.[125] To find out the effect of anion type of IL on the gas adsorption and separation performances of the CuBTC, molecular simulations were performed with five different ILs ($[EMIM]^+$ cation with $[SCN]^-$, $[Tf_2N]^-$, $[BF_4]^-$, $[NO_3]^-$, and $[PF_6]^-$ anions).[126] CO_2 uptake enhanced up to 3 bar no matter which IL was loaded into CuBTC because of the affinity between CO_2 and ILs, whereas adsorption of CH_4 and N_2 was not affected by the presence of IL. All IL/MOF composites were reported to have higher heats of adsorption for CO_2 compared to pristine CuBTC. The highest and lowest CO_2 adsorptions were observed for ILs with $[SCN]^-$ and $[Tf_2N]^-$, which are the smallest and the bulkiest anions studied, respectively. As the anion gets bulkier, less CO_2 was adsorbed on the composite which proved the effect of the anion type on the adsorption of CO_2 as shown in Figure 2.4. [BMIM][SCN]/CuBTC showed better CO_2/CH_4 and CO_2/N_2 mixture selectivity at all pressures compared to pure CuBTC.

Another computational study aimed to investigate the effect of anion type was about the desulfurization of natural gas.[127] Cu-TDPAT was the MOF and four different

ILs consisting of $[BMIM]^+$ cation and $[Cl]^-$, $[Tf_2N]^-$, $[PF_6]^-$ and $[BF_4]^-$ anions were selected. Superior isosteric heats of adsorption of H_2S and CH_4 were observed in all IL/MOF composites compared to pristine MOF, indicating that gases tend to be adsorbed more on the composite material. Q_{st} of H_2S in IL/MOF composites were much higher than that of CH_4 resulting from the highly polar nature of ILs and H_2S, therefore all composite materials exhibited higher H_2S/CH_4 selectivities than pure Cu-TDPAT. Because of having the smallest anion size, [BMIM][Cl] had more distinct filling sequence in Cu-TDPAT with increasing the loading. Compared to other IL/MOF composites, [BMIM][Cl]/Cu-TDPAT has the highest Q_{st} value for H_2S for all IL loadings while O_{st} values for CH_4 were similar for all composites. Consequently, [BMIM][Cl]/Cu-TDPAT exhibited the best H_2S adsorption and H_2S/CH_4 separation performance.

The selection of the correct MOF is important in terms of designing novel IL/MOF composites with outstanding gas adsorption and separation performances. A simulation work was carried out to investigate the diffusion behavior of IL, [BMIM][SCN] in the pores of five MOFs and eight COFs..[128] ILs showed better dispersion when they have smaller coordination number in the support material. [BMIM][SCN] has smaller coordination number in MOFs compared to COFs indicating that IL molecules can diffuse better in MOFs than COFs. Therefore, MOFs were considered as better supporters for ILs. Both IL/MOF and IL/COF composites showed higher adsorption selectivities for CO_2/CH_4 and CO_2/N_2 mixtures compared to pristine materials. Although [BMIM][SCN] was more dispersive in MOF-74(Mg) than ZIF-8 and IRMOF-1, the enhancement in the selectivities was much weaker compared to them. While $[SCN]^-$ provides new adsorption sites for CO_2, the competitive adsorption between CO_2 molecules and $[SCN]^-$ anions around the coordinately unsaturated metal site (CUS) of the MOF negatively affected the CO_2 adsorption.

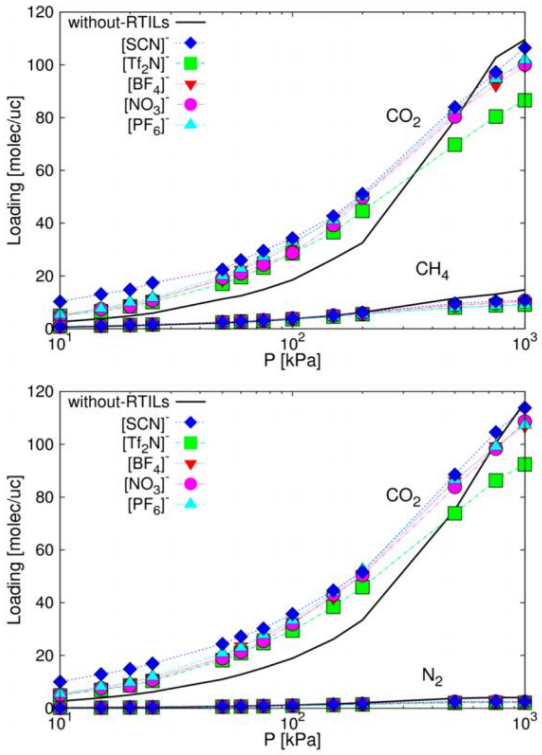

Figure 2.4. Adsorption isotherms computed for CO_2/CH_4 (top) and CO_2/N_2 (bottom) equimolar mixtures in the bare CuBTC and in the structure with eight molecules of ILs per unit cell.[126]

As discussed here, investigation of gas adsorption and separation performances of IL/MOF composites have drawn attention in the last few years. However, there is a limited number of studies in the literature and they use certain types of ILs and MOFs for preparing IL/MOF composites. Both experimental and computational studies that are summarized above show that imidazolium-based ILs were preferred in all prepared IL/MOF composites especially because of their commercially availability and high CO_2 solubility.[129] However, for designing novel adsorbents with better separation performances it is important to expand the knowledge about new IL and MOF families. Considering the large variety of available MOFs and ILs, results are very promising in terms of design and development of new IL/MOF composites with exceptional selectivity

for target gas separation applications. Moreover, combining experiments with computational methodology is very important to elucidate the effect of interactions on gas adsorption/separation performances of IL/MOF composites. With this motivation, gas storage and separation abilities of IL/MOF composites prepared by using both imidazolium-based and phosphonium-based ILs have been investigated computationally and experimentally focusing on CO_2/CH_4, CO_2/N_2, and CH_4/N_2 separations. The results obtained in this study are given in Chapter 4 and 5.

Chapter 3: Methods

In this chapter, computational and experimental methods used in this thesis study are covered. In the first part, experimental methods are described in detail and in the second part computational methods are explained comprehensively.

3.1. Experimental Methods

This section covers experimental techniques used for the characterization and gas adsorption performance analyses of the IL/MOF composites.

3.1.1. Materials and Sample Preparation

Materials used in this study ([BMIM][PF_6], phosphonium-based ILs, ZIF-8, CuBTC, and acetone) were purchased from Sigma-Aldrich with the highest purity commercially available. ILs and MOFs were freshly opened and stored in an Ar-filled glovebox (Labconco). Acetone was used to dissolve the IL for impregnation. The gases used for gas adsorption measurements were CH_4 (99.95 vol %), N_2 (99.998 vol %), and CO_2 (99.9 vol %) purchased from Linde gas company.

All composites were prepared in open atmosphere by using the wet impregnation method. Prior to sample preparation, the MOF was dried at 105 °C overnight in a vacuum oven to remove moisture and/or any other volatile impurities. As an example: for the preparation of [BMIM][PF_6]/ZIF-8 composite, first 0.30 g of [BMIM][PF_6] was dissolved in 30 mL of acetone and stirred at room temperature for approximately 1 h. The glass container was covered with Parafilm™ to avoid acetone evaporation during stirring. Then, 0.70 g of ZIF-8 was loaded into the solution, and the mixture was stirred at 30 °C

for 6 h in open atmosphere, allowing acetone to evaporate slowly. After acetone was completely evaporated, the resulting sample was dried in an oven at 105 °C overnight. The sample was labeled as [BMIM][PF_6]/ZIF-8, kept sealed in a vial, and stored in a desiccator to avoid humidity and other impurities.

3.1.2. Characterization Methods

3.1.2.1. Fourier Transform Infrared Spectroscopy

Fourier transform infrared (FTIR) spectroscopy is a widely used spectroscopic technique in organic and inorganic chemistry to determine the chemical functional groups present in a sample. In this technique, some of the infrared light is absorbed by the sample while some of it is transmitted through the sample, therefore the vibrational energy of molecule changes.[130] The resulting IR spectrum represents the molecular fingerprint of a sample with absorption peaks which correspond to the frequencies of vibrations between the bonds of the atoms making up the materials. The combination of atoms for different materials is unique, therefore it is not possible for two different compounds to have the same infrared spectrum.[131]

For FTIR measurements, a Bruker Vertex 80v IR spectrometer equipped with a sample holder with two potassium bromide (KBr) windows was used in transmission mode. Measurement of IR spectra was performed between spectral ranges from 4000 to 500 cm^{-1} with a resolution of 4 cm^{-1} for pure ZIF-8 and [BMIM][PF_6]/ZIF-8 composite and 2 cm^{-1} for CuBTC and phosphonium-based IL/ZIF-8 composites. For background and sample measurements, 128 and 512 scans were obtained, respectively, with a scanner velocity of 10 kHz. Background measurements were performed under vacuum using an empty sample holder. For pristine MOFs and IL/MOF composites, approximately 10 mg of sample was placed between two KBr windows and loaded into the sample holder. The holder was then placed into the spectrometer and sample measurements were performed under vacuum. For IL measurement, first approximately 10 mg of IL was mixed with

KBr powder and then placed between KBr windows and the measurement was performed as described above. Baseline correction was performed for each IR spectrum. For pristine MOFs and IL/MOF composites, IR bands were deconvoluted by employing Voigt function with Fityk[132] software.

3.1.2.2. Powder X-Ray Diffraction

Powder X-ray diffraction (PXRD) spectroscopy is an efficient analytical technique largely used for identification and characterization of a powder crystalline material. This method gives information on crystal structure, phase, texture, and other structural parameters such as crystallinity, crystal defects, and grain size.[133] In this method, generated X-rays are first sent to the sample and diffracted beams at specific angles from each set of lattice planes in a sample are detected by the detector of the instrument. The distribution of the atoms within the lattice determines the peak intensities, therefore X-ray diffraction pattern is the fingerprint of periodic atomic arrangements in a material.[133]

X-ray diffraction patterns of pure ZIF-8 and [BMIM][PF_6]/ZIF-8 composite were obtained using Bruker D2 Phaser instrument with X-ray generator performance of 30 kV of voltage and 10 mA of current. Cu-Kα_1 radiation source was used with a wavelength of 1.5418 Å and Lynxeye detector was used with a slit size of 1 mm. The analysis was carried out between 2θ values of 5-90° with a step size of 0.0204°. For CuBTC and phosphonium-based IL/MOF composites, Bruker D8 Advance instrument was used with Cu Kα_1 radiation source employing a wavelength of 1.5418 Å. The power rating of X-ray generator was adjusted to 40 kV and 40 mA and Vantec-1 detector was used with a slit size of 1 mm. The measurement was performed between 2θ values 5-90° with a step size of 0.0204°.

For the sample preparation, first a double-sided tape was attached on a glass slide and then approximately 10 mg of powder sample was spreaded on top of the tape. The sample covered the tape completely to prevent any amorphous signals coming from the tape. The glass slide was placed on a gum inside a sample container and the powder was

flattened with another piece of glass. Both pristine MOF and IL/MOF composites were prepared in a similar way and the same parameters were used for the measurement.

3.1.2.3. Scanning Electron Microscopy

Scanning electron microscopy (SEM) is used for scanning the samples with a focused beam of high-energy electrons to obtain high resolution images. A variety of signals (including secondary electrons that produce SEM images) originated from the interactions between electrons and atoms in the samples reveal information about the topography, crystalline structure, and chemical composition of the materials.[134]

SEM analysis was performed using Zeiss Evo LS 15 for imaging the micrographs of pristine MOFs and IL/MOF samples investigated in this study. Vacuum with an accelerating voltage of 3 kV was applied during the analysis and the working distance was adjusted to 6 mm and 6.5 mm for ZIF-8 and [BMIM][PF_6]/ZIF-8, respectively. For phosphonium-based IL/MOF composites, the same voltage was applied while the working distance was adjusted as 8 mm. Three different magnifications (20Kx, 10Kx, and 5Kx) were used for screening crystalline structure of the samples. For the sample preparation, carbon tape was pasted on the cell and then approximately 5 mg of sample was placed on it. Excess samples on the carbon tape surface were removed with a pump. After samples were placed into the instrument, high vacuum was applied to eliminate any impurity on the sample surface.

3.1.2.4. Brunauer-Emmett-Teller Surface Area and Pore Size Analysis

Brunauer-Emmett-Teller (BET) analysis is used for the determination of surface area of powders and porous solids by multilayer adsorption of nitrogen at -196 °C as a function of relative pressure (P/P_0).[135] The N_2 physisorption isotherm in the P/P_0 range of 0.05-0.3 is used for calculating the surface area using the BET equation[136] provided below:

$$\frac{1}{N \times (P_0/P - 1)} = \frac{C - 1}{N_m \times C}\left(\frac{P}{P_0}\right) + \frac{1}{N_m \times C} \quad (3.1)$$

where N is the weight of N_2 adsorbed at a given relative pressure (P/P_0), N_m is monolayer capacity which is the volume of gas adsorbed at standard temperature and pressure (STP, 273 °C and 1 atm) and C is the BET constant. Ideally, a minimum of three data points in the P/P_0 range 0.05-0.3 are entered in *"N"* and *"1/[N(P₀/P-1)]"* is plotted against *"P/P₀"*. The plot is generally linear and the slope *((C-1)/(NₘC))* and the intercept *(1/NₘC)* are used to calculate N_m and C. The BET surface area can then be calculated from the equation[135] below:

$$S_{BET} = \frac{N_m \times N_A \times s}{V_M} \quad (3.2)$$

where S_{BET} is the total BET surface area, N_A is Avogadro's number, s is the cross sectional area of the adsorbate and V_M is the molar volume at STP.

BET analysis was performed by using a Micromeritics ASAP 2020-Physisorption Analyzer.[137] Approximately 250 mg of sample was used for the measurements. Prior to measurements, samples were activated under vacuum in two steps (vacuum pressure for the activation of the samples was 100 μmHg). Temperature was raised up to 90 °C with a ramp rate of 10 °C/min and hold for 40 min, and then the temperature was raised up to 150 °C with a ramp rate of 10°C/min and hold for 10 h under vacuum. After the activation, sample was cooled down to -196 °C using liquid N_2 and free space was measured with helium gas. For removing residual helium gas, vacuum was applied to the sample for 10 h. At the end of all these steps, N_2 gas was fed to the system for measuring volumetric adsorption between 10^{-6} and 1 bar. A part of the N_2 adsorption isotherm in the P/P_0 range 0.04-0.3 was fitted to the BET equation to estimate the surface areas of the samples.

Pore volumes of pristine MOF and IL/MOF composites were also derived from N_2 adsorption isotherms at -196 °C using Non-Local Density Functional Theory (NL-DFT) method assuming cylindrical pore model, which is available in the software of Micromeritics ASAP 2020-Physisorption Analyzer.

3.1.2.5. Thermal Gravimetric Analysis

Thermal gravimetric analysis (TGA) measures the changes in the weight of a material as a function of the temperature or time under any gas flow. It is possible from the measured weight loss curve to get information about the changes in sample composition, thermal stability, volatile content, moisture in the sample, and decomposition kinetics. During the analysis, the material can be heated to a temperature up to 1000 °C.[138]

TGA experiments were performed for all the MOFs, ILs, and IL/MOF composites using a TA Instruments Q500 thermogravimetric analyzer[139] with a platinum pan. After taring, approximately 15 mg of sample was weighed. For CuBTC, ZIF-8, phosphonium-based ILs, phosphonium-based IL/MOF composites, and [BMIM][PF_6]/ZIF-8 composite, first a constant temperature ramp rate of 5 °C/min was adjusted up to 120 °C, then the temperature was kept constant for 8 h and finally, constant temperature ramp rate of 2 °C/min was employed up to 700 °C under N_2 flow of 40 and 60 ml/min for balance and purge gases, respectively. For [BMIM][PF_6], first a constant temperature ramp rate of 2 °C/min was adjusted up to 80 °C, then the temperature was kept constant for 5 h and finally, constant temperature ramp rate of 2 °C/min was set up to 700 °C under the same N_2 flow values. After experiment was done, platinum pan was cleaned carefully to remove any residual sample.

Thermal decomposition temperatures were compared by finding the onset (T_{onset}) and derivative onset (T'_{onset}) temperatures from gravimetric and derivative gravimetric curves. In general, T_{onset} values overestimate thermal decomposition temperature;[140-141] therefore, T'_{onset} values were used in this study.

3.1.2.6. X-ray Fluorescence

X-ray fluorescence (XRF) spectrometry is an elemental analysis technique which is widely used for the determination of the chemical compositions of different kind of materials in several forms such as liquid, solid, powder, and thin-film.[142] The analysis of the elements in materials by XRF is made possible by the behavior of atoms when they interact with X-ray photons. When individual atoms are excited by an external energy source with high energy and short wavelength, they emit X-ray photons of a characteristic energy or wavelength. It is possible to specify and quantify the existing elements by counting the number of photons and by this way, elemental analysis can be performed.[143]

XRF analysis was performed using a Bruker S8 Tiger XRF spectrometer under helium atmosphere. X-rays are generated by using a 4 kW Rh anode X-ray tube. Elemental compositions were determined as weight percentages by using an 18 mm mask. First, XRF sample container (Chemplex Industries Inc.) was filled with powder sample (approximately 0.25 g) and a 4 μm Prolene film support (Chemplex Industries Inc.) is placed on top of the container. Then, the film was immobilized with a ring. The common ppm level impurities in the measurements were Ca, P, Fe, Zn, Cu, Zr, Ti, and Al. Data interpretation was made by using the SpectraPlus Eval2 V2.2.454 software.

3.1.3. High Pressure Volumetric Adsorption Analysis

Gas storage and separation performances of both pure MOFs and IL/MOF composites were investigated by using a Micromeritics (Particulate Systems) High Pressure Volumetric Analyzer HPVA II-200[144] based on the static volumetric method. In volumetric adsorption technique, a known amount of gas was first dosed into the container which includes the sample to be analyzed. The sample was waited to reach the equilibrium with the adsorbate gas and then the final equilibrium pressure was recorded. The quantity of adsorbed gas was calculated using the difference between dosing and equilibrium pressures. This process was repeated at given pressure intervals until the

maximum pressure is reached. To measure desorption, the pressure was decreased to the initial pressure point and all the adsorbed gas is released. Finally, resulting adsorbed volume and equilibrium pressure was plotted and an isotherm was obtained.

HPVA analyzer includes an analysis port for adsorption measurements and a separate degas port which can be heated up to 500 °C for drying the sample before testing. The adsorption system also contains a vacuum pump and gauge, a gas manifold kept at 40 °C, two pressure transducers (high pressure and low pressure), a temperature control vessel which can be connected to a constant temperature bath and a stainless steel sample holder. The schematic of the HPVA system[145] is given in Figure 3.1.

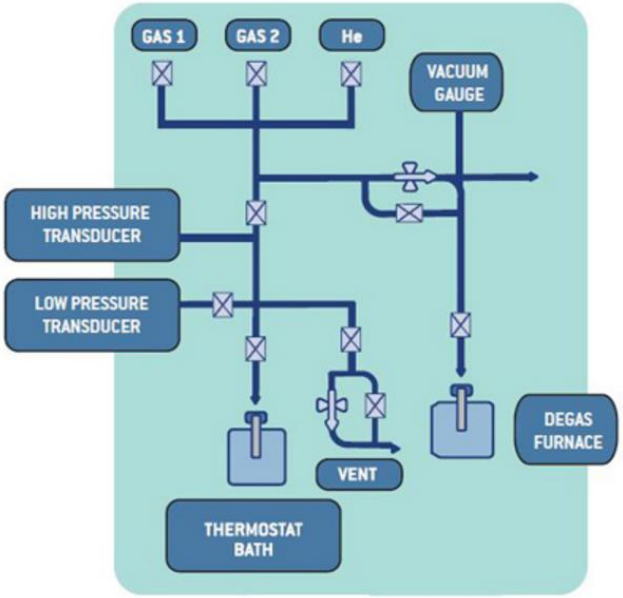

Figure 3.1. Schematic representation of HPVA system[145]

Volumetric gas adsorption analyses were carried out at different pressures ranging from 0.1 to 35 bar for CH_4, CO_2, and N_2 gases. Approximately 0.45 g of sample was weighed (wet sample weight) and loaded into a sample holder in open atmosphere. First, sample holder was connected to the degas port in a furnace for activation of the samples. Swagelok gaskets were used in the connections to prevent the leakage of gases. Pure

MOFs (ZIF-8 and CuBTC) were activated at 150 °C while IL/MOF composites ([BMIM][PF_6]/ZIF-8 and phosphonium-based IL/MOF composites) were activated at 125 °C under vacuum for overnight until the pressure reached to 10^{-6} bar. The stability of the samples under these degassing conditions was confirmed by IR and TGA measurements. After degassing, the sample holder was cooled and placed into a water bath at ambient temperature to make the experiment at constant temperature (approximately at 25 °C), then it was connected to the analysis port. Before starting the adsorption measurements, all lines were purged with helium three times to remove any residual gases from previous experiments. After purging manually, the analysis is performed by HPVA II automatically. First, system is evacuated for 10 minutes. Then, free space is measured using helium gas at 0.8 bar and after that system is evacuated again for 30 minutes. When the adsorption/desorption analysis at given pressure points is completed, system is cleaned with helium to remove the adsorbate gas in the system. Adsorbed amounts of gases were obtained and calculated by using dry sample weights measured after measurements.

After measurements were completed, the adsorption isotherms were obtained using the Excel macro provided with HPVA II. Dual site Langmuir and Freundlich models were fitted to single-component gas adsorption isotherms to determine adsorbed gas amounts at exact pressure points. The dual site Langmuir and Freundlich relations used for fitting are given below, respectively:

$$N_{ads} = \frac{A \times P}{B + P} + \frac{C \times P}{D + P} \tag{3.3}$$

$$N_{ads} = \frac{E \times P^G}{F + P^G} \tag{3.4}$$

where N_{ads} is the adsorbed gas amount in cm^3/g STP, P is pressure in bar and A, B, C, D, E, F, and G are fitting parameters.

Ideal gas selectivities of the samples were calculated by dividing the volume amount of the more adsorbed component to the less adsorbed one at the same pressures. Langmuir- and Freundlich-fitted single component adsorption isotherms were used for determination of the selectivities. Gas separation performances of pure ZIF-8, pure CuBTC, IL/ZIF-8, and IL/CuBTC composites for CO_2/CH_4, CO_2/N_2, and CH_4/N_2 gas pairs were investigated.

3.2. Computational Methods

3.2.1. Density Functional Theory (DFT) Calculations

As a part of the collaboration study,[43] DFT calculations were performed by a colleague, Volkan Balci. DFT calculations of [BMIM][PF_6]/ZIF-8 composite were conducted using Gaussian 09 software.[146] Different conformers of [BMIM][PF_6] were first optimized at the Becke's three-parameter hybrid exchange functional[147] and the Lee−Yang−Parr correlation functional[148] (B3LYP) method together with the 6-31+G(d) basis set. The conformer search for [BMIM][PF_6] was performed according to the methodology previously reported.[149] The lowest energy conformer was further optimized, and the vibration frequencies were calculated both at the B3LYP/6-311+G(2d,p) level to enhance the accuracy of calculations. Furthermore, binding energies, ΔE_B, between anions and cations were calculated and corrected for scaled zero-point vibrational energies (ZPVE) for each conformer, as reported previously.[149] Similarly, the lowest energy conformer of [BMIM][PF_6] was incorporated into a ZIF-8 cage (obtained from the Cambridge Structure Database,[150-151] consisting of 288 atoms) and optimized at the B3LYP/6-31G(d) level. The position of all ZIF-8 atoms were initially frozen to preserve the crystalline cage structure of ZIF-8, while the [BMIM][PF_6] atoms were released inside the cage, and a conformer search was conducted by altering the position of [BMIM][PF_6] inside the fixed cage. After the lowest energy conformer was obtained for [BMIM][PF_6]/ZIF-8, the ZIF-8 atoms that are in close proximity of the [BMIM][PF_6]

atoms were released free. A total of 120 atoms were released (i.e., 88 atoms of ZIF-8 and 32 atoms of [BMIM][PF_6]), and the rest of the 200 atoms of the ZIF-8 cage were kept frozen. A conformer search was further performed for the partially released [BMIM][PF_6]/ZIF-8 system by altering the position of [BMIM][PF_6] near the released ZIF-8 atoms and optimizing the resulting structure at the B3LYP/6-31G(d) level. The vibration frequencies of all [BMIM][PF_6]/ZIF-8 conformers were calculated at the B3LYP/6-31G(d) level and scaled by a factor of 0.9614[152] to compensate for harmonic effects. Furthermore, population analysis was conducted with a full Natural Bond Orbital (NBO) analysis using NBO version 3.1[153], as reported before.[149] In order to investigate the effect of dispersion interactions on the geometry and binding energy of ZIF-8 and [BMIM][PF_6]/ZIF-8, the D3 version of Grimme's dispersion with Becke−Johnson (BJ) damping[154] was also included into the standard DFT calculations performed in this study (i.e., B3LYP/6-31G(d) level). The term B3LYP-D3(BJ) will be used in the rest of the manuscript as a reference to dispersion-included DFT calculations performed at the B3LYP/6-31G(d) level.

3.2.2. Grand Canonical Monte Carlo (GCMC) Simulations

Atomically detailed simulations were performed using the GCMC method to obtain adsorption isotherms of CO_2, CH_4, and N_2 for pristine ZIF-8 and for [BMIM][PF_6]/ZIF-8 by Materials Studio.[155] GCMC simulations were conducted by a colleague, Çiğdem Altıntaş, as a part of the collaboration study.[43] The crystal structure of ZIF-8 was obtained from the Cambridge Structure Database as in the case of DFT calculations.[151] The lowest energy equilibrium conformer of [BMIM][PF_6], which was optimized by DFT calculations as described above, was used in the simulations. These structures were imported into Materials Studio[156] and used without further optimization. The interactions between ZIF- 8, [BMIM][PF_6], and gas molecules (CO_2, CH_4, and N_2) were modeled using Lennard−Jones (LJ) 12-6 and Coulomb interactions. Several different force fields have been used in molecular simulations of MOFs in the literature.[127, 157] Universal Force

Field (UFF)[158] was used for ZIF-8 and IL to obtain CO_2 adsorption, while a modified version of UFF[159] was used for ZIF-8 and IL to obtain CH_4 and N_2 adsorption in a better agreement with the experimental results. The force field parameters used for simulations of ZIF-8 and IL/ZIF-8 are given in Appendix A.

Several computational methods for accurately assigning partial charges to MOFs have been developed in the recent years. These methods basically have a compromise between time efficiency and the rigor of the method. Since charges are not experimentally observable, there is no way to choose a method as the most accurate one. The atomic charges of ZIF-8 were calculated using the Qeq charge equilibration method of the Materials Studio and charges of [BMIM][PF_6] were obtained from the study of Chen et al.,[124] respectively. Since the GCMC results based on these charge assignment methods agree with the experimental measurements of gas adsorption as shown below, these methods are in all the simulations in this study. CO_2 was modeled as a three-site, rigid, linear molecule using UFF with partial charges assigned to each atom. It is important to note that other force fields such as EPM2 were also used to model CO_2 adsorption in ZIF-8 in the literature.[159] UFF was simply selected because a good agreement between experiments and simulations was obtained for gas adsorption isotherms. CH_4 was modeled as a single LJ site with no charge molecule following Goodbody et al.,[160] and N_2 was modeled as a two-site LJ molecule with no charge following Galassi et al.[161] LJ parameters and partial charges used for gas molecules are given in Appendix A.

After obtaining a good agreement between simulations and experimental results for ZIF-8 as discussed below, 24 wt% of IL as determined by BET and XRF measurements, corresponding to three IL molecules in 1 unit cell of ZIF-8, were incorporated into MOF using Metropolis algorithm in fixed loading task of sorption module in Materials Studio. The anion and cation were modeled as a rigid body and represented as a motion group before the loading simulation. Equilibration and production steps were used as 5×10^6. For van der Waals (electrostatic) interactions, the atom-based (Ewald) summation method with a cutoff radius of 15.5 Å (12 Å) was used. The lowest energy frame obtained at the end of the simulation was further used in gas adsorption simulations. The

adsorption isotherms of CO_2, CH_4, and N_2 were calculated between 0.1 and 10 bar using the adsorption isotherm task of sorption module at 298 K. More detailed information about the Monte Carlo methods used in Materials Studio can be found elsewhere.[155] Absolute gas adsorption amounts obtained from the GCMC simulations were converted to excess gas adsorption to compare with the experimental results using the following equation, $N_{excess} = N_{abs} - V_p \rho_{gas}$, where N_{excess} is the excess amount of gas molecules, N_{abs} is the absolute amount of gas molecules, V_p is the pore volume of the MOF to describe the volume of the gas phase, and ρ_{gas} is the density of the bulk gas.

The isosteric heats of adsorption for CO_2, CH_4, and N_2 gases were obtained from single-component adsorption isotherm simulations conducted in Materials Studio software using the adsorption isotherm task of the Sorption module. Materials Studio software utilizes the Clapeyron equation to calculate the isosteric heats of adsorption for gas molecules, which is calculated as the difference of partial molar enthalpy of the sorbate component between the gas reservoir and the framework.

3.2.3. Ideal Adsorbed Solution Theory (IAST) Calculations

Ideal selectivity gives an idea about the gas separation performance of a material. However, gases exist as mixtures in reality; therefore, it is important to report mixture selectivities of materials. Measuring single-component gas adsorption isotherms of materials is possible by using some commercial instruments; however, a similar type of measurements becomes very complex, expensive, and time consuming for gas mixtures.[162] Therefore, prediction of binary gas adsorption isotherms using reliable theoretical approaches is highly valuable. Ideal adsorbed solution theory (IAST)[163] which has been commonly used for obtaining multicomponent adsorption isotherms of porous materials using single component adsorption isotherm data to predict mixture selectivities was used in this study. Almost all studies in the literature which compared molecular simulations of mixture adsorptions in MOFs with IAST predictions found that the results are consistent with each other.[20] Several studies in the literature[164-167] showed that IAST

works well to predict adsorption behavior of gas mixtures in ZIFs. Binary gas mixture selectivities (CO_2/CH_4, CO_2/N_2, and CH_4/N_2, in a 50/50 mixture) of ZIF-8 and [BMIM][PF_6]/ZIF-8 samples were obtained by IAST calculations and compared with experimental selectivities. Mixture selectivities were calculated using dual site Langmuir fit parameters which described in Section 3.1 (Equation 3.3).

Chapter 4: Improving Gas Separation Performance of ZIF-8 by [BMIM][PF_6] Incorporation and Elucidation of Interactions Between [BMIM][PF_6] and ZIF-8[†]

Because of its advantageous properties such as being commercially available, hydrophobic and CO_2 selective, ZIF-8 (commercially available as Basolite Z1200) has been investigated computationally and experimentally for gas adsorption and separation. IL/MOF composite has been prepared with an IL, [BMIM][PF_6], which has a remarkable CO_2 affinity and hydrophobic nature. Later, both pristine ZIF-8 and [BMIM][PF_6]/ZIF-8 composite have been characterized prior to adsorption performance analysis. In the first part of Chapter 5, characterization results of pristine ZIF-8 and composite material are given. In the second part, results of gas adsorption and separation measurements combined with molecular simulations and DFT calculations are provided.

4.1. Preparation of [BMIM][PF_6]/ZIF-8 Composite

All materials mentioned in this chapter (ZIF-8, [BMIM][PF_6], and high purity acetone) have been purchased from Sigma-Aldrich. The chemical structure of [BMIM][PF_6] can be seen in Figure 4.1. ZIF-8 and [BMIM][PF_6] were freshly opened and stored in Ar glovebox (Labconco). The preparation of [BMIM][PF_6]/ZIF-8 composite was performed in open atmosphere using wet impregnation method (Chapter

[†] The results given in this chapter were published in ACS Applied Materials and Interfaces with following reference: Kinik, F. P.; Altintas, C.; Balci, V.; Koyuturk, B.; Uzun, A.; Keskin, S., [BMIM][PF_6] Incorporation Doubles CO_2 Selectivity of ZIF-8: Elucidation of Interactions and Their Consequences on Performance. ACS Applied Materials and Interfaces, **2016**, *8* (45), 30992–31005. This chapter is the reformatted version of the mentioned research paper.

3.1.1). After the samples were prepared and dried in oven overnight, they were sealed with Parafilm^{TM} and stored in a desiccator to minimize water and impurity content.

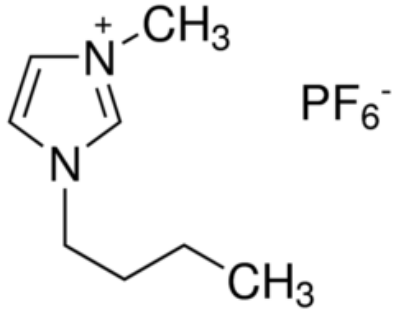

Figure 4.1. Chemical structure of [BMIM][PF_6][168]

4.2. Characterization of ZIF-8 and [BMIM][PF_6]/ZIF-8 Composite

4.2.1. Characterization of ZIF-8

ZIF-8 is a widely studied MOF which is commercially available and supplied from Sigma-Aldrich. In this study, some characterization experiments were conducted to compare the physicochemical properties of ZIF-8 with available literature data. First, the crystal structure of ZIF-8 was investigated using PXRD. To understand the crystal morphology in detail, SEM was used. Then, the thermal stability of ZIF-8 was checked by TGA. Finally, N_2 adsorption at -196 °C and 0-1 bar was performed to determine the BET surface area and pore volume of ZIF-8.

4.2.1.1. Powder X-Ray Diffraction (PXRD) Results of ZIF-8

PXRD analysis was performed to identify the crystal structure of ZIF-8 used in this study. XRD pattern of pristine ZIF-8 was obtained using the measurement parameters given in Chapter 3. The resulting XRD pattern of ZIF-8 was compared with the literature as shown in Figure 4.2. The intensity values were normalized according to the highest

peak observed in the measurements to compare the results accurately. The peaks obtained from the XRD measurement in this thesis study are obtained by the same way as with the literature data.

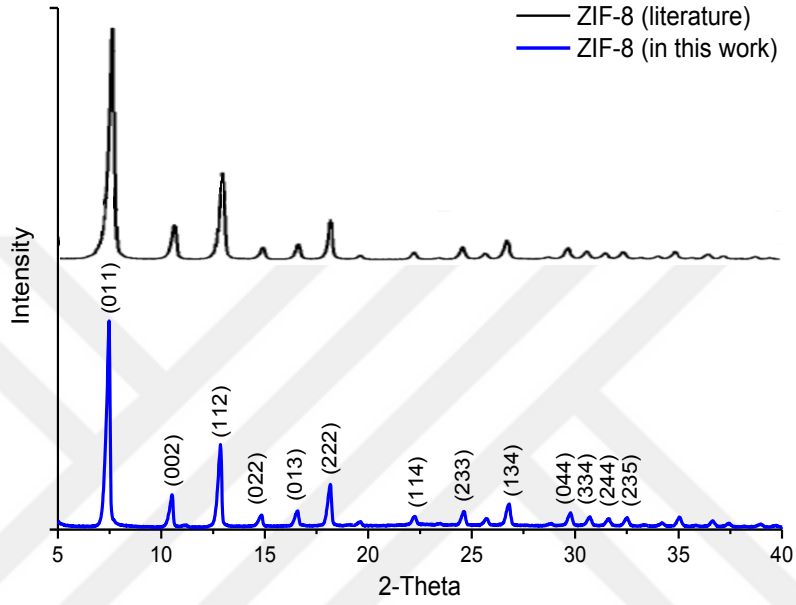

Figure 4.2. X-ray diffraction pattern of ZIF-8 used in this study (blue) and its comparison with XRD pattern adapted from literature (black)[35]

4.2.1.2. Scanning Electron Microscopy (SEM) Images of ZIF-8

SEM was used for obtaining images at very high magnifications to investigate surface characteristics of the materials. SEM pictures of ZIF-8 were produced at different magnifications to get information about the morphology and particle size of the sample. Micrographs of ZIF-8 are shown in Figure 4.3 that the crystal shapes and sizes of ZIF-8 used in this study are in agreement with those obtained from the literature, which is given in Figure 4.4.

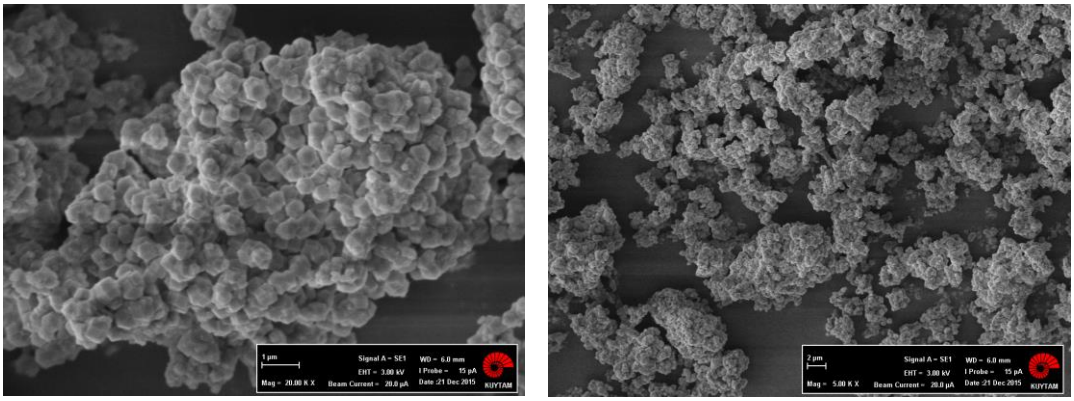

Figure 4.3. Morphology of ZIF-8 crystals at different magnifications: (a) 20,000x; (b) 5,0000x.

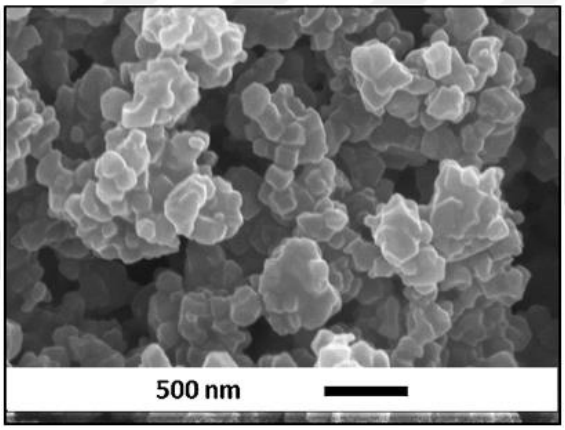

Figure 4.4. SEM image of ZIF-8 crystals obtained from Ref.[169]

4.2.1.3. Thermal Gravimetric Analysis (TGA) Results of ZIF-8

TGA was performed for the determination of weight loss of ZIF-8 with increasing temperature. This analysis gives the temperature value where the decomposition of the material starts. ZIF-8 was first heated up to 120 °C with a constant temperature ramp rate of 5 °C/min, then the temperature was kept constant for 8 h and finally, ZIF-8 was heated again with a rate of 2 °C/min up to 700 °C under N_2 flow. The resulting weight percent change and derivative weight percent change with temperature are given in Figure 4.5.

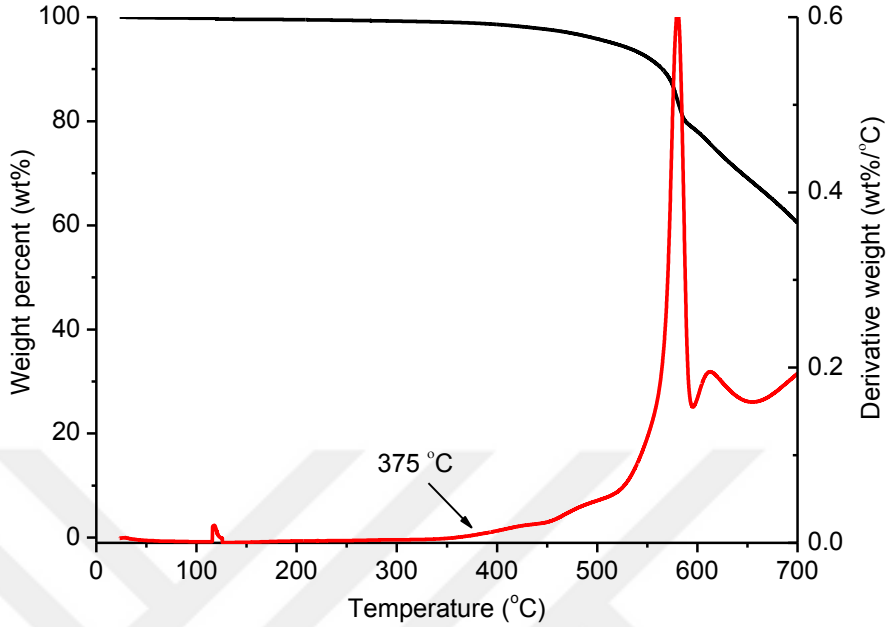

Figure 4.5. Thermal gravimetric analysis results for ZIF-8. The black line and left *y*-axis shows weight percent change with temperature and the red line and right *y*-axis shows derivative weight percent change with temperature.

TGA results in Figure 4.5 show that there is almost no weight loss in ZIF-8 resulting from the water content because of its hydrophobic nature. The derivative onset temperature (T'_{onset}) was used to obtain the decomposition temperature of ZIF-8 framework. ZIF-8 starts to decompose at 375 °C with an approximately 60 wt% of the initial mass remaining in the pan after a temperature ramp to 800 °C. Results were also compared with the literature data (Figure 4.6) and it was found that the thermal decomposition temperature obtained in this study is comparable with the temperature obtained from the literature.

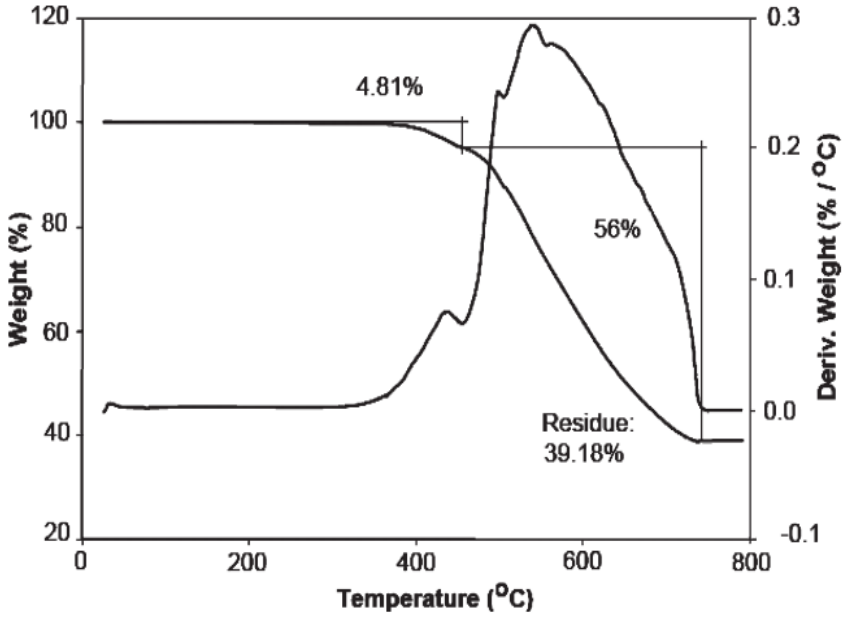

Figure 4.6. Thermal gravimetric analysis results for ZIF-8 adapted from work by Phan et al.[170] The first line and left *y*-axis shows weight percent change with temperature and the second line and right *y*-axis shows derivative weight percent change with temperature.

4.2.1.4. Fourier Transform Infrared (FTIR) Spectroscopy Results of ZIF-8

FTIR spectroscopy provides useful information about the structure and interactions between the molecules, and these interactions can be monitored by the shifts in band positions.[171] Therefore, experimental IR spectra of all samples were thoroughly analyzed and shifts (higher than the spectral resolution) in the corresponding band positions were investigated. IR spectra of ZIF-8 was measured between spectral ranges from 4000 to 500 cm^{-1} with a resolution of 4 cm^{-1} and the comparison with the literature data was provided in Figure 4.7. As seen in Figure 4.7, the IR peak positions of ZIF-8 obtained in this study are in agreement with the spectra reported in literature.[172] The peaks in the IR spectra between 3100-3200 cm^{-1} are assigned to C-H stretching of the imidazolium ring.[173] Because of the in-plane and out of plane bending of the imidazolium ring, some

peaks observed between 950-1200 cm^{-1} and 550-800 cm^{-1}, respectively.[173] Detailed information related with the IR peaks of ZIF-8 are given in Appendix B.

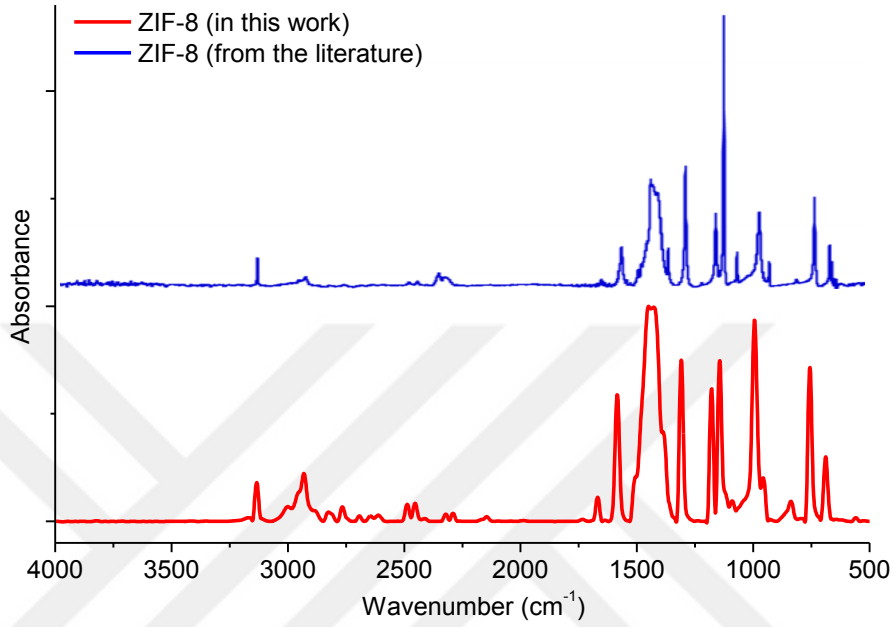

Figure 4.7. FTIR spectra of ZIF-8 obtained in the spectral range of 500-4000 cm^{-1}. Red line represents the experimental data obtained in this study and blue line shows the literature data.[172]

4.2.1.5. Brunauer-Emmett-Teller (BET) Surface Area and Pore Volume Measurements of ZIF-8

For the determination of BET surface area and pore volume of ZIF-8, N_2 adsorption and desorption isotherms were obtained at -196 °C between 0-1 bar. A part of the nitrogen adsorption isotherm between the relative pressures (P/P_0) of 0.04-0.3 was fitted to the BET equation to estimate the surface areas of the samples. The resulting adsorption and desorption isotherms are provided in Figure 4.8.

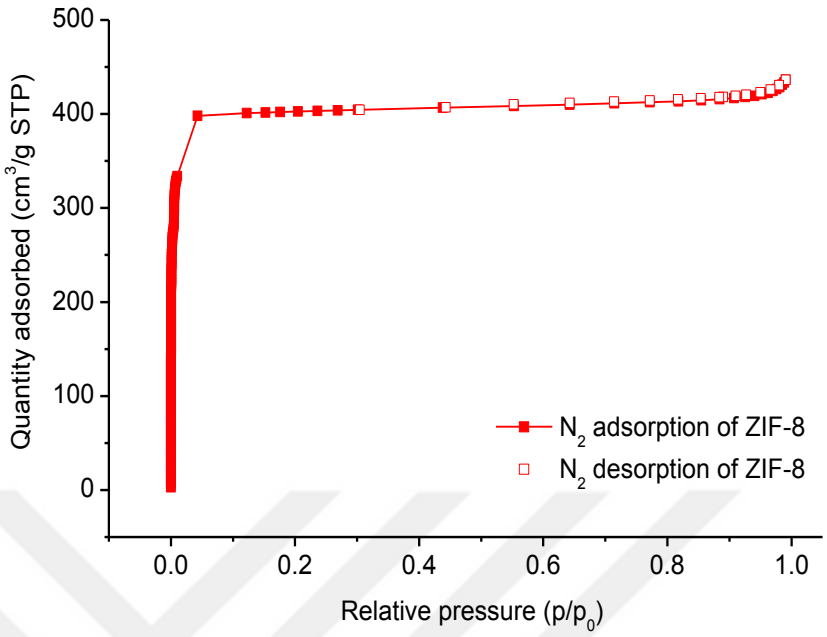

Figure 4.8. N_2 adsorption-desorption isotherm at -196 °C between 0-1 bar for ZIF-8.

From N_2 adsorption isotherm, the BET surface area and pore volume of ZIF-8 were calculated as 1208 m^2/g and 0.6332 cm^3/g, respectively. BET surface area value of ZIF-8 is slightly higher than those obtained by Huang et al. (1030 m^2/g)[174] and Cravillon et al. (962 m^2/g)[175] who used two different synthetic protocols. However, the pore volume measured in this study is almost the same with the ZIF-8 obtained by Park et al. (0.64 cm^3/g)[68] while the surface area is lower (1630 m^2/g). These differences are mainly arise from different synthesis conditions including time, temperature, ratio of the precursors, and type of solvent.[176]

4.2.2. Characterization of [BMIM][PF6]/ZIF-8 Composite

The characterization measurements performed for ZIF-8 as described above were also performed for [BMIM][PF_6]/ZIF-8 composite with an additional method, X-ray fluorescence (XRF) spectroscopy, which was used to calculate the IL loading amount in the composite material.

4.2.2.1. Powder X-Ray Diffraction (PXRD) Results of [BMIM][PF_6]/ZIF-8

XRD pattern of [BMIM][PF_6]/ZIF-8 was obtained using the measurement parameters given in Chapter 3 to investigate the effect of IL impregnation on the crystal structure of ZIF-8. The integrity of the crystal structure of ZIF-8 after IL incorporation is provided in Figure 4.9. The intensity values were normalized according to the highest peak observed in the measurements to compare the results accurately.

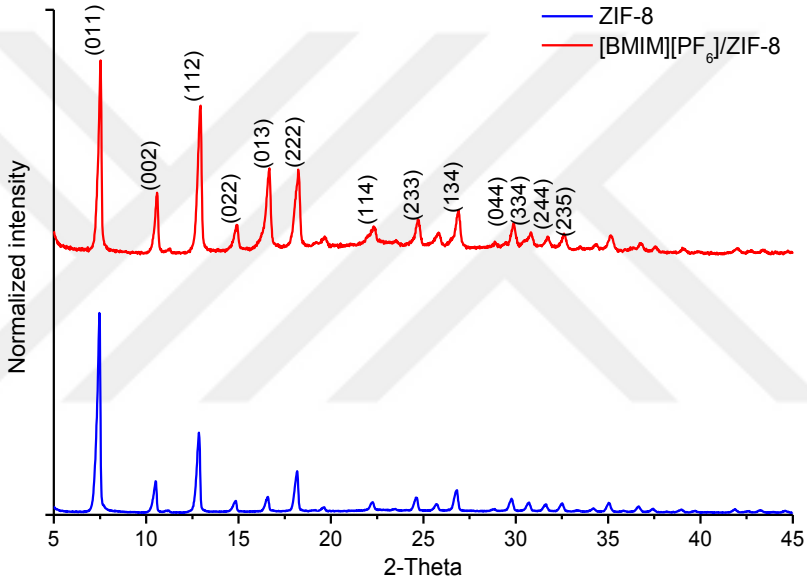

Figure 4.9. X-ray diffraction pattern of ZIF-8 (blue) and [BMIM][PF_6]/ZIF-8 (red).

X-ray diffraction results presented in Figure 4.9 illustrate that the characteristic peaks of ZIF-8 remain intact after IL incorporation. These results confirm the lack of any structural changes within the framework of ZIF-8 upon the incorporation of [BMIM][PF_6]. Except from the intensity of the feature at $2\theta = 7.34°$, all intensities changed with the introduction of IL. This result possibly indicates a change in the electron density of ZIF-8 upon IL incorporation. However, it is important to note that the change in the intensity of the peaks could be because of many reasons including but not limited

to partial decomposition, sample preparation, preferred orientation, and instrument alignment.

4.2.2.2. Scanning Electron Microscopy (SEM) Images of [BMIM][PF_6]/ZIF-8

SEM was used for investigating the morphology of ZIF-8 after IL incorporation. SEM images of IL/ZIF-8 samples are provided in Figure 4.10. As seen from the images, the stability of framework after IL incorporation was confirmed. The size and shape integrity of the particles in [BMIM][PF_6]/ZIF-8 were almost the same with those of pristine ZIF-8, thus it is inferred that the crystal structure is mostly preserved during the incorporation of IL into ZIF-8.

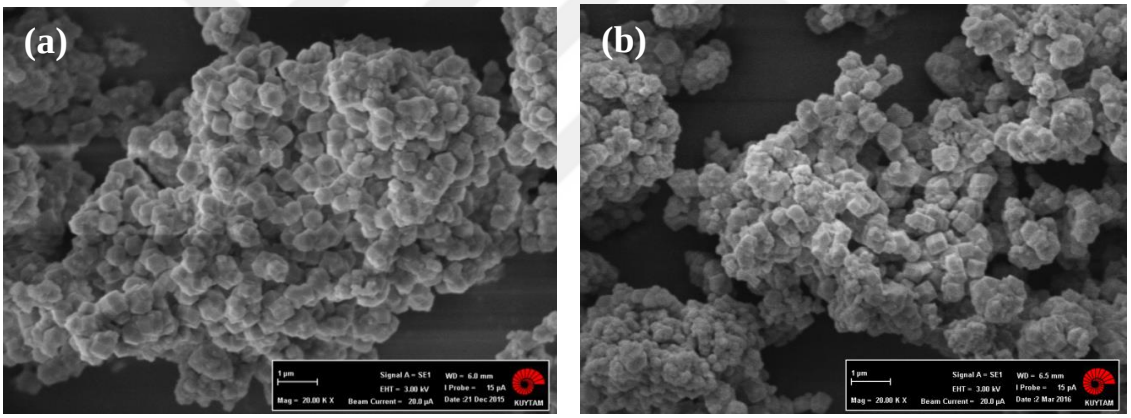

Figure 4.10. Morphology of (a) ZIF-8 and (b) [BMIM][PF_6]/ZIF-8 samples obtained from the SEM analysis.

4.2.2.3. Brunauer-Emmett-Teller (BET) Surface Area Results of [BMIM][PF_6]/ZIF-8

Surface area and micropore volume of IL/ZIF-8 composite was calculated using N_2 adsorption isotherms obtained at -196 °C. The adsorption and desorption isotherms are

given in Figure 4.11 and the resulting BET surface area and micropore volume are given in Table 4.1, respectively.

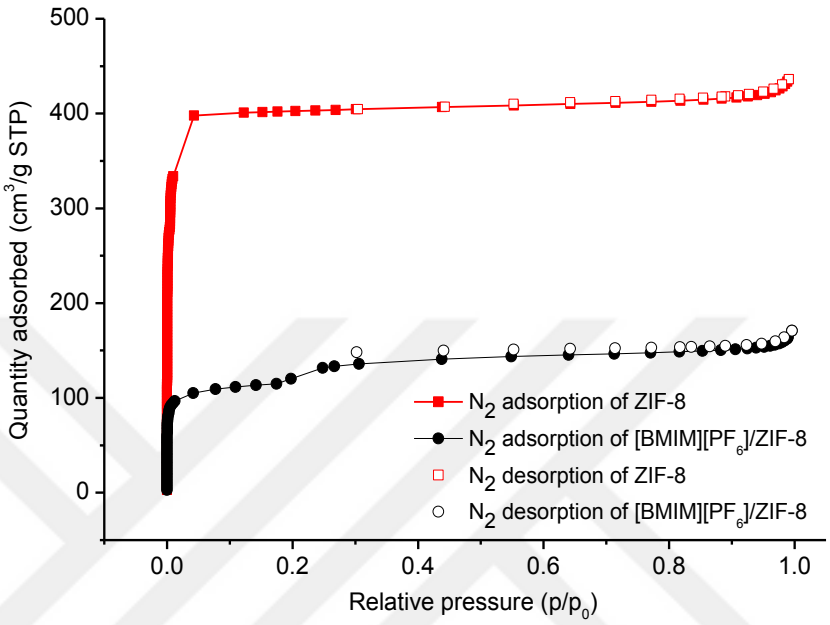

Figure 4.11. N_2 adsorption-desorption isotherm at -196 °C between 0-1 bar for ZIF-8 and [BMIM][PF_6]/ZIF-8.

Table 4.1. Surface area and pore volume values of ZIF-8 and [BMIM][PF_6]/ZIF-8

	ZIF-8	**[BMIM][PF_6]/ZIF-8**
BET surface area (m^2/g)	1208	415
Pore volume (cm^3/g)	0.63	0.22

It can be seen from Figure 4.11 that the N_2 adsorption amount decreases with the IL incorporation into ZIF-8 framework because of the occupancy of the pores. Upon incorporation of IL, the BET surface area decreases from 1208 to 415 m^2/g with a corresponding decrease in the pore volume from 0.6332 to 0.2197 cm^3/g. This decrease in the pore volume was originated from the IL incorporation. Using the pore volume

values obtained for ZIF-8 and [BMIM][PF_6]/ZIF-8, the IL loading amount was calculated. For the calculation, Equation 3.4 was used:

$$W_{[BMIM][PF_6]} = \frac{\left(V_{ZIF-8} - \left(\frac{V_{[BMIM][PF_6]/ZIF-8}}{1 - W_{[BMIM][PF_6]}}\right)\right) \times \rho_{[BMIM][PF_6]}}{1 + \left(V_{ZIF-8} - \left(\frac{V_{ZIF-8}}{1 - W_{[BMIM][PF_6]}}\right)\right) \times \rho_{[BMIM][PF_6]}} \quad (3.5)$$

where $W_{[BMIM][PF6]}$ is the IL loading (wt%), V_{ZIF-8} is the pore volume of 1 g of ZIF-8, $V_{[BMIM][PF6]/ZIF-8}$ is the pore volume of 1 g of [BMIM][PF_6]/ZIF-8 composite and $\rho_{[BMIM][PF6]}$ is the density of [BMIM][PF_6]. By dividing the $V_{[BMIM][PF6]/ZIF-8}$ into (1 - $W_{[BMIM][PF6]}$), the pore volume of the IL/MOF composite including 1 g of MOF was found (Normally, the resulting composite is 1 g). The difference between V_{ZIF-8} and $V_{[BMIM][PF6]/ZIF-8}$ (for the composite including 1 g of ZIF-8) gives the volume that was occupied by IL molecules. By multiplying this difference with $\rho_{[BMIM][PF6]}$, the amount of IL in IL/MOF composite (including 1 g of ZIF-8) was calculated. By dividing the IL amount into the sum of IL and MOF (1 g) amount, IL loading was found. However, IL/MOF composite material is 1 g, therefore IL loading was calculated as below:

(1 + x) g composite	x g IL
1 g composite	?

According to these calculations, the corresponding IL loading was calculated as approximately 24 wt%.

4.2.2.4. X-ray Fluorescence (XRF) Results of [BMIM][PF_6]/ZIF-8

The elemental analysis was performed using XRF technique to determine amounts of Zn and P. Using these amounts, the IL loading was calculated and the amount that was

found in BET measurements was confirmed. Data given in Table 4.2 show that P and Zn amounts in IL/ZIF-8 sample were 2.68 wt% and 23.53 wt%, respectively. For IL loading calculation, first the concentration of P (wt%) was divided by the molar mass of P and the mole number of P was found. Every [BMIM][PF_6] molecule has 1 mole of P as can be seen from the structure given in Figure 4.1, therefore the mole number of P equals to the mole number of [BMIM][PF_6]. The mole number of [BMIM][PF_6] was multiplied by the molecular weight of [BMIM][PF_6] and the IL amount was found in the unit of "g". The same calculations were made for finding ZIF-8 amount in the composite by using the concentration of Zn element. Finally, IL loading can be calculated by dividing the amount of [BMIM][PF_6] by sum of the amounts of [BMIM][PF_6] and ZIF-8. Based on these values, an IL loading of approximately 23 wt% was found. These results indicate that although an IL loading of 30 wt% was targeted for sample preparation, some portion of the IL was not incorporated into ZIF-8 and lost on the walls of the sample container during sample preparation. Therefore, the IL loading for the rest of this study was set to 24 wt%.

Table 4.2. Zn and P amount in the IL/ZIF-8 sample according to XRF measurements

Formula	Concentration (wt%)
CHN	73.70
Zn	23.53
P	2.68
Impurities	0.08

4.2.2.5. Thermal Gravimetric Analysis (TGA) Results of [BMIM][PF_6]/ZIF-8

TGA was conducted to understand at which temperature the weight loss starts because of decomposition of the sample. The weight percent and derivative weight

percent changes for both pristine ZIF-8 and IL/ZIF-8 samples are presented in Figure 4.12(a) and Figure 4.12(b), respectively.

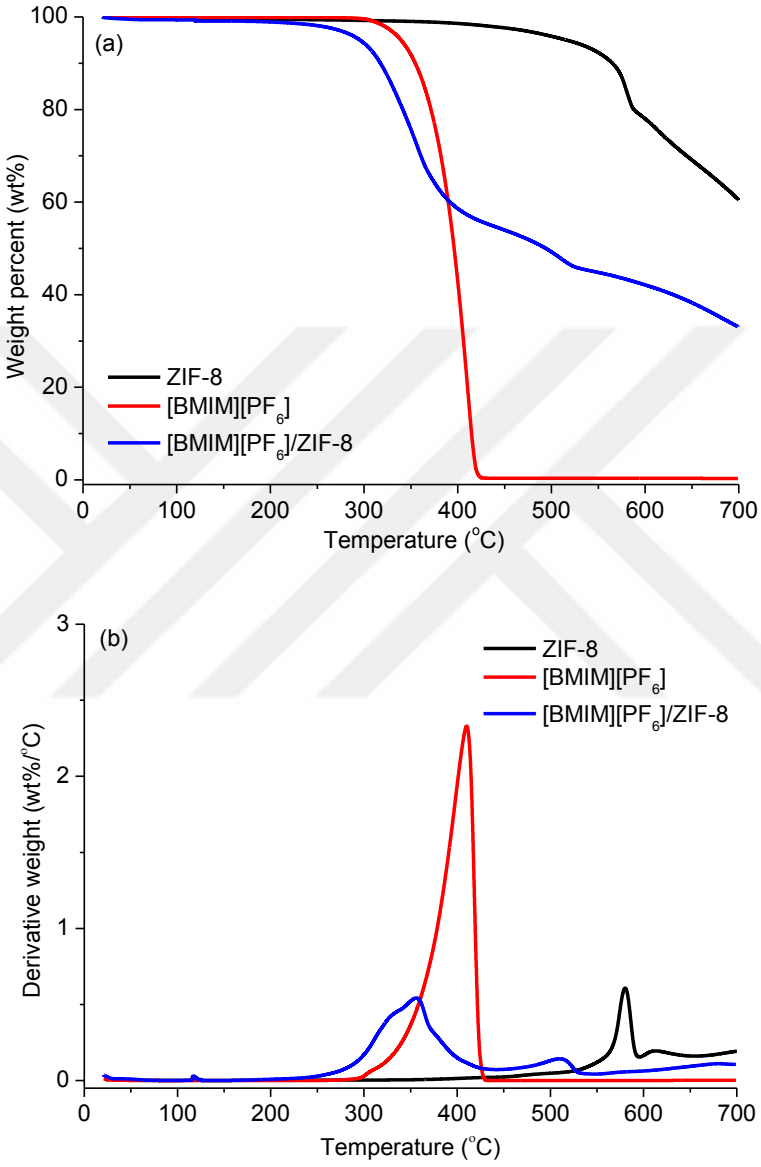

Figure 4.12. TGA results of ZIF-8, [BMIM][PF6], and [BMIM][PF6]/ZIF-8: (a) change of weight percent with increasing temperature and (b) change of derivative weight percent with increasing temperature.

TGA of the samples shown in Figure 4.12 demonstrates that there is no weight loss in samples resulting from the water content. Because, both [BMIM][PF_6] and ZIF-8 have hydrophobic nature and all samples were kept in sealed desiccators after preparation. Data indicate that [BMIM][PF_6]/ZIF-8 sample has more weight loss than the pristine ZIF-8 sample when both of them were heated up to 700 °C under N_2 flow. This behavior results from the addition of the amount decomposed from [BMIM][PF_6] to that from ZIF-8 in the analysis of IL/MOF composite. T_{onset} and T'_{onset} temperatures obtained from TGA measurement are given in Table 4.3. Results for bulk IL indicate that the decomposition starts at a temperature of 298 °C (determined by T'_{onset}) and before the temperature reaches 450 °C, the IL completely disappears. For ZIF-8, TGA measurements performed at the same heating rate as the one for bulk IL shows that ZIF-8 starts to decompose at 375 °C with an approximately 60 wt% of the initial mass remaining in the pan after a temperature ramp to 700 °C. The [BMIM][PF_6]/ZIF-8 sample, on the other hand, indicates a remaining mass of approximately 33 wt% of the initial mass. For an IL loading of approximately 24 wt% as determined by BET and XRF measurements, one can expect to see approximately 45 wt% of the total mass remaining in the pan after the ramp to 700 °C for this specific sample (that is approximately 60 wt% of the ZIF-8 amount in the [BMIM][PF_6]/ZIF-8 sample, as bulk IL appears to completely disappear at 700 °C). However, TGA profile of the [BMIM][PF_6]/ZIF-8 sample indicates a remaining mass of approximately 33 wt%, much less than the expected amount. Moreover, the decomposition temperature determined by this measurement was 236 °C, which is significantly lower than that of both bulk IL and pristine ZIF-8. These results indicate that the initial temperature for thermal decomposition reaction shifts to a lower temperature, most probably accompanied by a change in the decomposition mechanism as well. Such a change in decomposition mechanism indicates that there are direct interactions between IL and MOF. Because of these interactions the [BMIM][PF_6]/ZIF-8 sample behaves as a different system than its individual components. Thus, the individual thermal decomposition reactions alter significantly, involving the decomposition of more of ZIF-8 fragments, leading to a significant decrease in the final

weight and T'_{onset}. Such decrease was also observed in the thermal stability of metal-oxide-supported imidazolium ILs.[177]

Table 4.3. Onset temperatures and weight losses for ZIF-8, [BMIM][PF_6], and [BMIM][PF_6]/ZIF-8 composite calculated from TGA measurements

Sample	T_{onset} (°C)	T'_{onset} (°C)	Weight loss (%)
ZIF-8	382	375	40.3
[BMIM][PF_6]	305	298	100.0
[BMIM][PF_6]/ZIF-8	240	236	67.6

4.2.2.6. Fourier Transform Infrared (FTIR) Spectroscopy Results of [BMIM][PF_6]/ZIF-8

FTIR spectroscopy was used to determine the existence of IL in IL/MOF composite and elucidate the interactions between IL and MOF. Data for the bulk [BMIM][PF_6], ZIF-8, and [BMIM][PF_6]/ZIF-8 are presented in two different frequency regions, 3300-2800 cm^{-1} and 1700-500 cm^{-1}. In both regions, there are some shifts in the IR spectrum of bulk [BMIM][PF_6] towards either higher or lower wavenumbers, as blue and red shifts, respectively. These shifts (specifically those higher than the spectral resolution) provide evidence on the interactions between IL and MOF. For this purpose, first the IR features in bulk IL were determined as described in Appendix B.

The IR spectra of the bulk [BMIM][PF_6], ZIF-8, and [BMIM][PF_6]/ZIF-8 in the ranges of 3300-2800 cm^{-1} and 1700-500 cm^{-1} are given in Figure 4.13 and Table 4.4. The deconvoluted peaks of IR spectra of [BMIM][PF_6], ZIF-8, and [BMIM][PF_6]/ZIF-8 are also given in Appendix B. The strongest region of the IR spectrum of [BMIM][PF_6] is the CH stretching region between 2800 and 3300 cm^{-1}.[178] The vibration bands of the imidazolium ring of the [BMIM][PF_6] at 3124, 2984, and 2965 cm^{-1} show blue shifts (by 5, 14, and 6 cm^{-1}, respectively) in IL/ZIF-8. Similarly, in 1700-500 cm^{-1} region, other

bands belonging to the imidazolium ring of the [BMIM][PF_6], at 1603, 1366, 1300, 1252, 1138, 864, 748, and 525 cm^{-1}, present blue shifts (by 15, 6, 6, 8, 9, 5, 11, and 5 cm^{-1}, respectively) upon the incorporation of [BMIM][PF_6] into ZIF-8 structure. Together with these blue shifts, the bulk IL's bands at 1387, 883, 837, 792, 779, 698, 557, and 536 cm^{-1} show red shifts by 5, 5, 14, 6, 5, 5, 5, and 6 cm^{-1}, respectively. According to the band assignments based on the DFT calculations (see assignments in Appendix B), all of these bands, except for the one at 698, 779, and 1387 cm^{-1}, belong to the $[PF_6]^-$ anion. Based on these shifts in the IR spectra, the interpretation of the interactions between [BMIM][PF_6] and ZIF-8 is as follows: The red shifts at the stretching frequencies of $[PF_6]^-$ anion, at 883, 837, 792, 557, and 536 cm^{-1}, indicate that the P–F bonding weakens upon the incorporation of IL into MOF. This weakening in P–F bond is attributed to an electron sharing between the anion and ZIF-8 indicating direct interactions between the imidazole rings present in ZIF-8 framework and $[PF_6]^-$. Consistent with this interpretation, the strength of the C2–H and C4,5–H stretching of the imidazolium ring increases as indicated by blue shifts at 3124, 1138, and 748 cm^{-1} and at other bands belonging to the imidazolium ring. Apparently, as the anion interacts with the MOF, it shares less electron with the cation. Thus, the inner bonds of the cation get stronger, possibly accompanied by hydrogen bonding with the framework as indicated by these blue shifts at its IR fingerprints.[179] Three remaining bands at 1387, 779, and 698 cm^{-1} are assigned to the deformation vibrations of the imidazolium ring. The red shifts observed on these bands upon the incorporation of IL into the MOF can be attributed to the confinement of IL in the cages of ZIF-8. The shifts observed on the IR bands of bulk IL are accompanied by shifts in IR bands of ZIF-8 as well, as illustrated in Appendix B. Although the assignment of these peaks was not fully accomplished,[173] it is inferred that incorporation of IL into the MOF modifies the surface structure of ZIF-8. These structural modifications are also evidenced by the observed intensity variations in the XRD features of ZIF-8 upon IL incorporation.

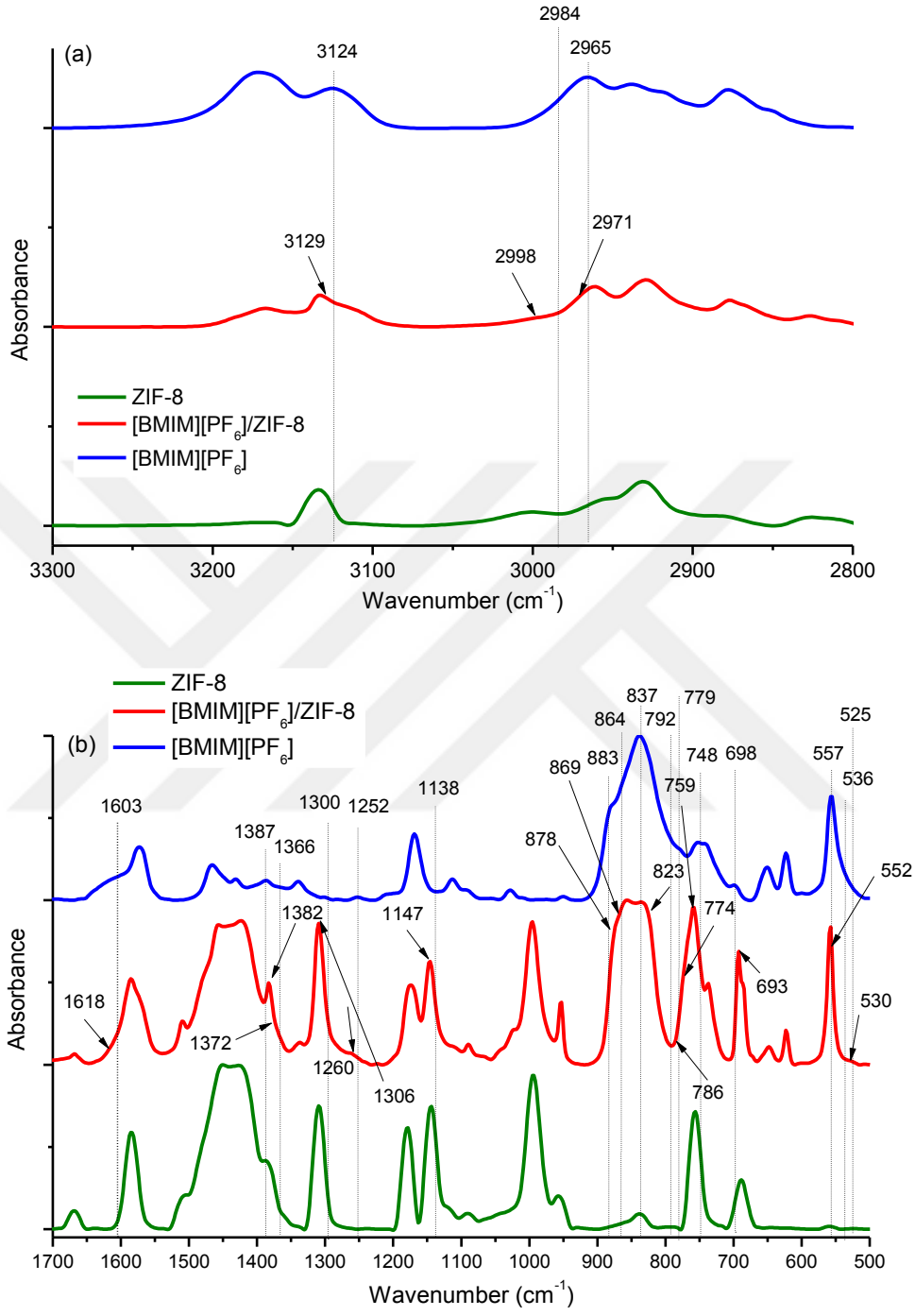

Figure 4.13. FTIR spectra of ZIF-8, [BMIM][PF_6]/ZIF-8 sample and [BMIM][PF_6] between (a) 3300-2800 cm^{-1}, and (b) 1700-500 cm^{-1}. Only the bands with shifts higher than the spectral resolution (4 cm^{-1}) are shown in both regions.

Table 4.4. IR peaks of bulk IL showing shifts upon incorporation into ZIF-8

Assignment	Bulk IL (exp.)	IL/ZIF-8 composite (exp.)
C2-H stretching	3124	3129
CH_3 HCH asymmetric stretching and CH_2 HCH asymmetric stretching	2984	2998
CH_3 HCH asymmetric stretching and $CH_2CC(N)$ HCH asymmetric stretching on butyl	2965	2971
$CH_3(N)$ HCH bending, ring in plane asymmetric stretching	1603	1618
$CH_2(N)$ HCH wagging, $CH_2C(N)$ HCH twist	1387	1382
$CH_2CH_2(N)$ HCH twist, $CH_2CC(N)$ HCH wagging, ring in plane symmetric stretching	1366	1372
$CH_2CH_2CH_2(N)$ HCH twist, CH_3 HCH bending on butyl	1300	1306
$CH_2CH_2CH_2(N)$ HCH twist, CH_3 HCH bending on butyl, C2-H bending	1252	1260
C4,5-H and C2-H sym bending, $CH_3(N)$ HCH asym bending	1138	1147
PF_6 asymmetric stretching, $CH_2(N)$ HCH bending, $CH_3CH_2CH_2$ C-C asymmetric bending	883	878
$CH_2(N)$ HCH bending, $CH_3CH_2CH_2$ C-C asym bending	864	869
PF_6 asymmetric stretching, C2-H, and C4,5-H out of plane bending, $CH_2(N)$ HCH rocking	837	823
PF_6 asymmetric stretching, C2-H out of plane bending, CH bending on butyl	792	786
$CH_2CH_2C(N)$ HCH rocking and CH_3 HCH rocking on butyl	779	774
C4,5-H symmetric out of plane bending, C2-H out of plane bending	748	759
N-CH_3 and N-CH_2 N-C stretching, ring bending, $CH_2CH_2C(N)$ HCH rocking	698	693
PF_6 asymmetric stretching	557	552
PF_6 asymmetric stretching	536	530
CCCC bending on butyl, ring out of plane bending	525	530

In conclusion, both pristine ZIF-8 and [BMIM][PF_6]/ZIF-8 samples have been characterized in deep detail using different characterization techniques. XRD analysis and SEM micrographs showed that the crystal structure of ZIF-8 remained intact after IL incorporation. As expected, the pore volume and surface area of the IL/ZIF-8 samples were found lower than those of pristine ZIF-8 because of the occupancy of available pore space of MOF by IL molecules. Decrease in the pore volume and XRF analysis results were used for the calculation of IL loading and it was found that 24 wt% of IL was confined inside the pores of ZIF-8. TGA and FTIR results also proved that IL was successfully impregnated into ZIF-8. Moreover, these analyses showed that there is an interaction between MOF and IL molecules.

4.3. DFT Calculations of ZIF-8 and [BMIM][PF_6]/ZIF-8

The interactions between [BMIM][PF_6] and ZIF-8 were needed to be confirmed at the atomic level. Tripathi et al.[180] illustrated similar shifts in the vibrational bands of *ν*(C2–H) with the confinement of 1-*n*-ethyl-3-methylimidazolium tetrafluoroborate [EMIM][BF_4] into the nanopores of MCM-41 by combining experiments with DFT calculations. They showed that these shifts result from the interaction between the oxygen of the silica surface and the C–H of the imidazolium ring. Similarly, our recent work illustrated direct interactions between [BMIM][BF_4] with various metal oxides.[171] Very recently, Dhumal et al.[108] investigated the interactions between Cu-based MOF and [EMIM][$EtSO_4$] by DFT calculations and vibrational spectroscopy. It was reported that the anion of the IL interacts with the metal Cu ions of the MOF, therefore the interionic interaction is remarkably improved. Similar to these reports elucidating interactions between ILs and surfaces in confined spaces at the atomic level, DFT calculations were performed to fully support the above-mentioned interpretation on IL-MOF interactions. For this purpose a detailed conformer search was performed to obtain the lowest energy equilibrium geometry for [BMIM][PF_6]/ZIF-8. The ZPVE-corrected binding energies for all conformers are presented in Appendix A. Figure 4.14 presents the geometry of the

conformer with the lowest energy obtained by B3LYP, and the corresponding XYZ coordinates are provided in Appendix A. This geometry in Figure 4.14 illustrates that the [BMIM][PF_6] lies inside the ZIF-8 cage, and the imidazolium ring of [BMIM][PF_6] aligns parallel to the plane of the pore opening of a ZIF-8 cage. $[PF_6]^-$ anion, on the other hand, locates itself parallel to an imidazolium ring of the ZIF-8 framework. Based on this geometry it is inferred that [BMIM][PF_6] is anchored to the ZIF-8 pore opening through C4,5–H, CH_2(N), and CH_3(N) of the $[BMIM]^+$ cation and $[PF_6]^-$ anion, while the butyl chain of $[BMIM]^+$ cation is twisted towards the inside of ZIF-8 cage. In order to elucidate the nature of molecular interactions, a natural bond orbital (NBO) analysis was also conducted on this lowest energy conformer geometry. The analysis corroborated that the protons at the C4,5–H, CH_2(N), and CH_3(N) positions of the $[BMIM]^+$ cation interact mainly with the N atoms of the ZIF-8 pulling electron density from cationic Zn centers as confirmed by the blue shifts in experimental IR features of the cation, as described above. These interactions result in more positive natural charges for the Zn atoms and they are accompanied by the interaction of the anion with the imidazolium ring of the ZIF-8 framework. On average, the P–F bond distances increase with that facing the ZIF-8 framework elongating by approximately 0.014 Å. This increase in P–F bond distances is consistent with the red shifts experimentally observed on ν(P–F) bands. Other details on the bond distances and NBO analysis can be found in SI in as a separate file. As reported by Antony et al.[181] contribution of London dispersions to the overall energy is crucial and cannot be omitted for large systems similar to the one investigated in the present study. Therefore, DFT calculations were also performed using B3LYP-D3(BJ) to elucidate the magnitude of dispersion interactions in [BMIM][PF_6]/ZIF-8. Results showed that the inclusion of dispersion interactions into the DFT calculations led to significant contribution to the overall energy as well as binding energy between [BMIM][PF_6] and ZIF-8. For instance, dispersion interactions resulted in a significant decrease in ZPVE-uncorrected binding energy for Conf-1 from -85 to -227 kJ/mol with a corresponding dispersion energy contribution of approximately 69%. A similar

conformer search including dispersion interactions resulted in a very similar geometry with the one already presented by performing B3LYP calculations in terms of IL position and orientation inside the MOF cage. Thus, it is inferred that inclusion of the dispersion interactions in DFT calculations do not change the main conclusions of this study, although data show that these interactions have a pronounced effect on determining the binding energy of IL molecule in the MOF cage.

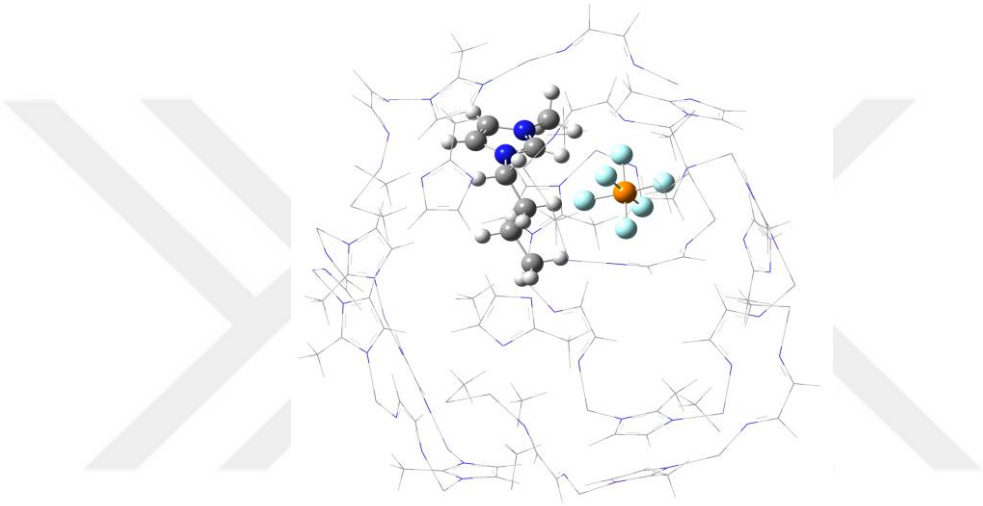

Figure 4.14. The lowest energy equilibrium conformer of [BMIM][PF_6]/ZIF-8 optimized at B3LYP/6-31G(d). For clear representation, ZIF-8 and [BMIM][PF_6] are demonstrated in wireframe and ball-and-bond type representation, respectively.

4.4. Gas Adsorption Measurements

Gas adsorption measurements were performed experimentally and computationally for CO_2, CH_4, and N_2 gases at room temperature between 0.1 and 35 bar. First, all gas uptakes of ZIF-8 were obtained experimentally and compared with the ones in the literature to understand whether the gas capture performance of pristine material is the same with the previous measurements. Then, adsorption measurements were conducted for IL/MOF composite with the same gases. GCMC simulations were also performed for

the comparison with the experimental results. Gas separation performances of the materials were determined by calculating the ideal gas selectivity, which is the ratio of single-component gas uptake data. Results showed that [BMIM][PF_6] incorporation enhances CO_2 selectivity towards CH_4 and N_2 gases especially in the low pressure region.

4.4.1. Gas Adsorption Analysis of ZIF-8

Gas adsorption measurements for ZIF-8 were performed experimentally and computationally according to the procedure explained in Chapter 3. Before experimental gas adsorption measurements, ZIF-8 was activated at 150 °C overnight under high vacuum (10^{-6} bar) to remove all impurities from the pores. For the validation of experimental results, GCMC simulations were also performed. CO_2, CH_4, and N_2 gas uptakes obtained from the experiments and GCMC simulations between 0.1-10 bar are shown in Figure 4.15. As can be seen from Figure 4.15, there is a good agreement between experiments and simulations for all gases.

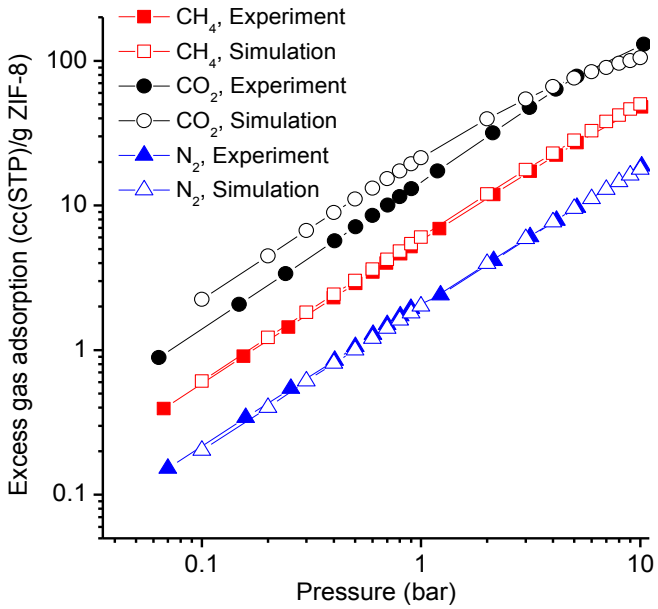

Figure 4.15. Single-component adsorption isotherms of CO_2, CH_4, and N_2 in ZIF-8.

Experimental adsorption isotherms obtained in this study were also compared with the literature data as shown in Figure 4.16. Results of the adsorption measurements are very close to those obtained from the literature especially in the low pressure region (between 0-1 bar). N_2 uptake measurements in this study were slightly lower than Battisti et al.[182] because they performed a computational study to obtain adsorption isotherms while the results in this study come from experimental measurements. CO_2 and CH_4 adsorption measurement results taken from the literature are experimental data and therefore they are in a good agreement with the adsorption isotherms in this study.

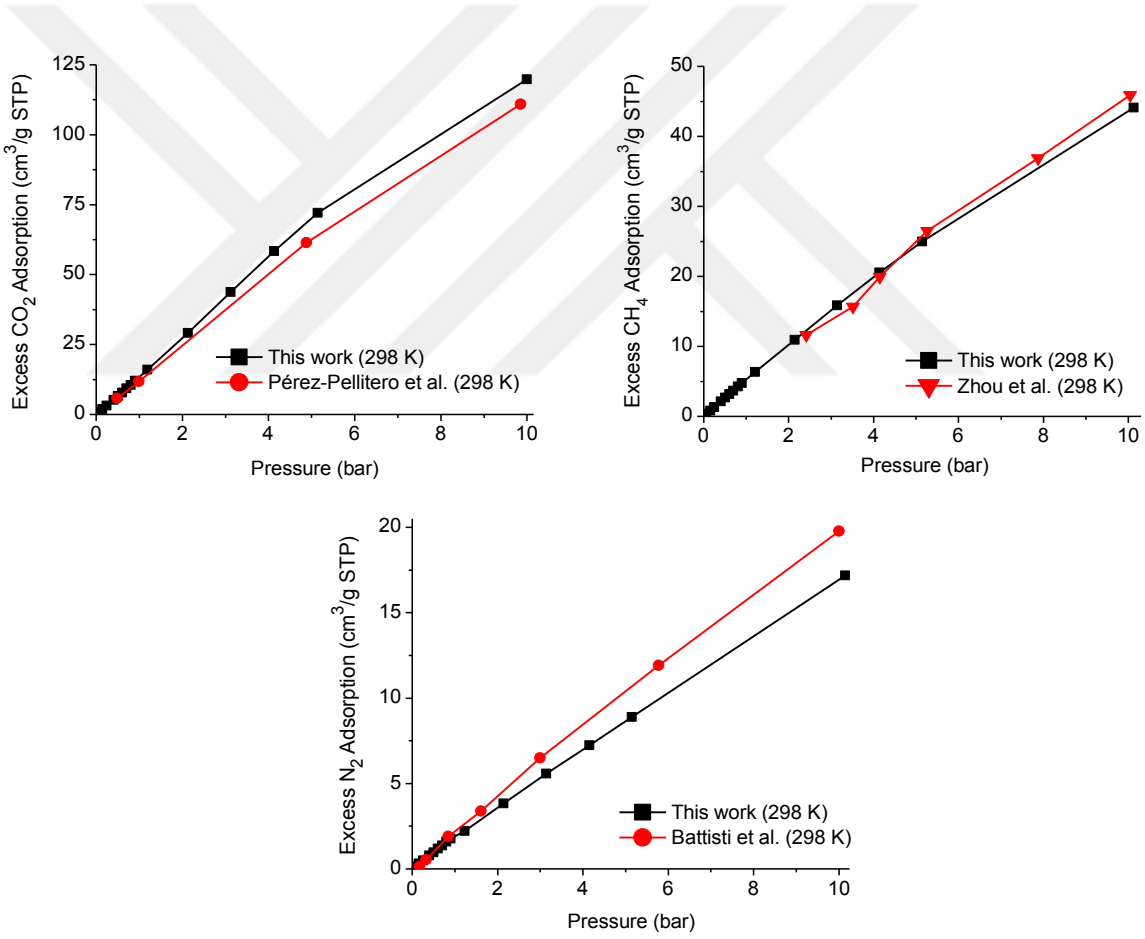

Figure 4.16. Experimental adsorption isotherms of ZIF-8 obtained in this study and their comparison with the literature data for (a) CO_2[159]; (b) CH_4[183]; and (c) N_2[182] gases.

4.4.2. Gas Adsorption Analysis of [BMIM][PF_6]/ZIF-8 Composite

Consequences of the interactions between [BMIM][PF_6] and ZIF-8 on the gas storage and separation performance of ZIF-8 were investigated by combining experiments with the GCMC simulations. Results of the experimental volumetric gas adsorption measurements and GCMC simulations for [BMIM][PF_6]/ZIF-8 up to 10 bar are shown in Figure 4.17. Comparison of the adsorption isotherms for the same gas on the same figure both for ZIF-8 and [BMIM][PF_6]/ZIF-8 was also given in Figure 4.18. Unsurprisingly, [BMIM][PF_6]/ZIF-8 samples have less gas uptakes compared to pristine ZIF-8 because the number of adsorption sites and available pore volume were reduced by the partial occupation of the pores by [BMIM][PF_6] as confirmed by BET and XRF measurements. Similar behavior was previously reported on a system prepared by the incorporation of [BMIM][BF_4] in CuBTC.[93] It was shown that as the [BMIM][BF_4] loading in CuBTC was increased from 5 wt% to 30 wt%, the adsorption amount of CH_4, CO_2, H_2, and N_2 gases decreased significantly.[93] A similar decrease observed in the gas adsorption performance of [BMIM][PF_6]/ZIF-8 can also be explained by the FTIR data showing strong interactions between ZIF-8 and [BMIM][PF_6]. As a result of these interactions, [BMIM][PF_6]/ZIF-8 acts as a different material compared to pristine ZIF-8 in terms of gas adsorption property.

In the simulations of [BMIM][PF_6]/ZIF-8, the energy parameter (ε) of C atoms in ZIF-8 was modified with a factor of 0.6 (ε_c = 0.18 kJ/mol) to obtain a better agreement with the experimental results for CH_4 and N_2 adsorption. Simulation results with unmodified energy parameter of C atom are also shown in Appendix B for comparison. This, in fact, suggests that incorporation of [BMIM][PF_6] changes the adsorption behavior on ZIF-8, thus, the simulation results provide better agreement with the experimental results only if the energetic parameters for C of ZIF-8 are modified. Here, it is important to note that several molecular simulation studies were performed to compute gas adsorption in similar IL/MOF composites, as mentioned above.[124, 126-128] However, to the best of our knowledge, this is the first study which compares predictions

of molecular simulations with the experimental measurements for three different gas adsorptions in IL/MOF composites. Results suggest that it is not very accurate to simply use generic force fields for molecular simulation of IL/MOF composites. IL incorporation may significantly change the adsorption affinity of the MOFs because of the interactions between them. Thus, new force fields are required to represent the modified adsorption preference of these IL/MOF systems.

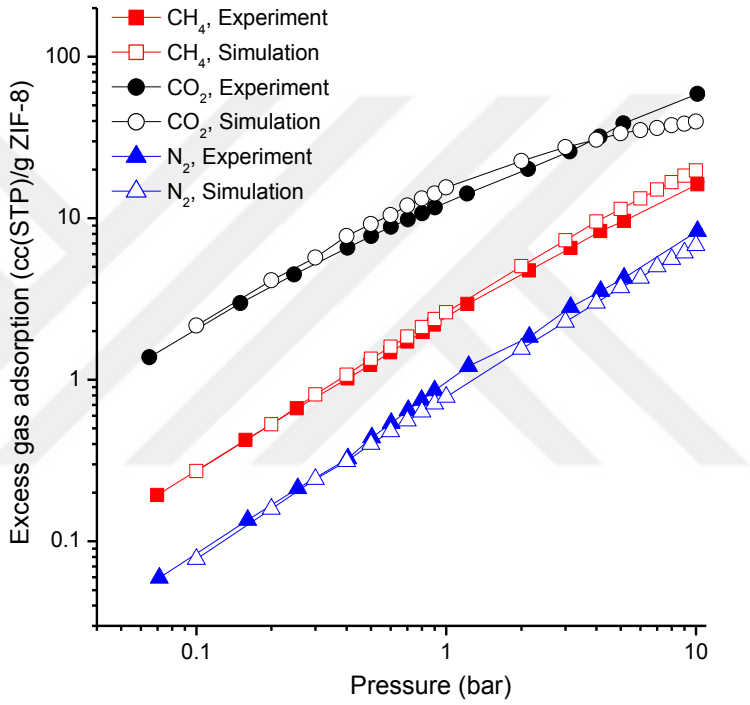

Figure 4.17. Single-component excess adsorption isotherms of CO_2, CH_4, and N_2 in [BMIM][PF_6]/ZIF-8.

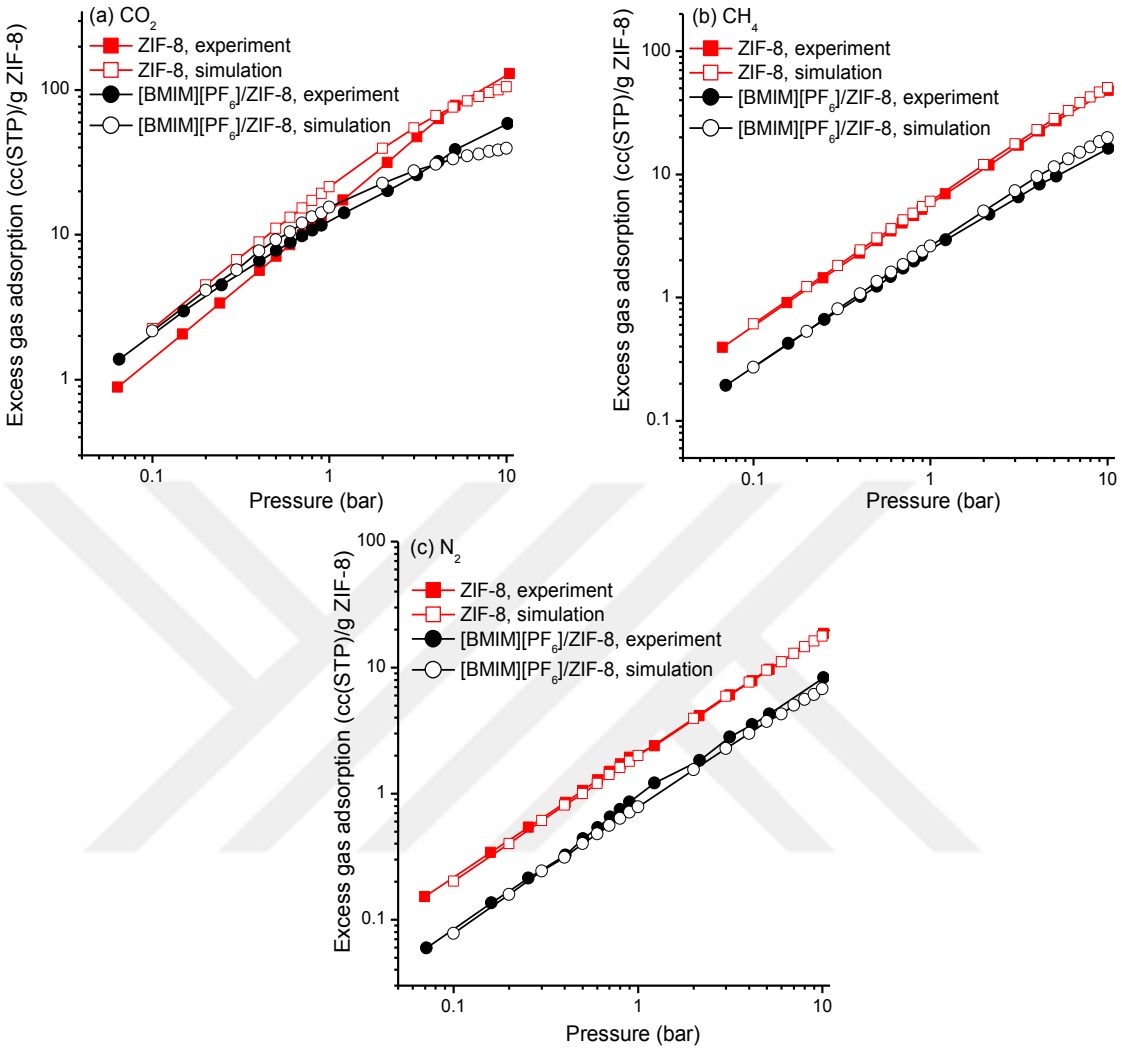

Figure 4.18. Comparison of the adsorption isotherms for (a) CO_2, (b) CH_4 and (c) N_2 for both ZIF-8 and [BMIM][PF_6]/ZIF-8 composite.

Results presented in Figure 4.17 and Figure 4.18 show that IL incorporation into a MOF generates a decrease in the uptake amounts of all gases used in this study (except for CO_2 up to 0.4 bar) but it also creates new adsorption sites because of the presence of IL and its interactions with the MOF. The affinity of each adsorption site is differently altered for each gas, thus reduction of gas uptakes differ particularly at low pressures.

Figure 4.19 shows the adsorption capacity change in comparison with pristine ZIF-8. Unlike the case in other gases, the CO_2 uptake per gram of ZIF-8 remarkably increased up to 0.4 bar upon the IL incorporation. According to this result, it seems that adsorption performance of ZIF-8 was enhanced up to 0.4 bar. Therefore, it is concluded that the incorporation of IL created new stronger adsorption sites for CO_2 at low pressures. However, CO_2 adsorption underperformed after that point in IL/ZIF-8 composite compared to pristine ZIF-8. The most apparent changes were observed in CH_4 and N_2 uptakes, which are nearly half of their values on ZIF-8.

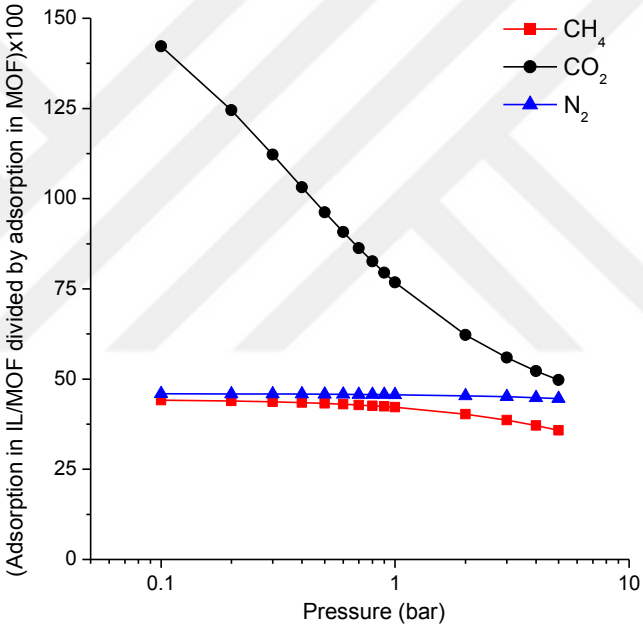

Figure 4.19. Change in gas adsorption amount upon incorporation of [BMIM][PF_6] in ZIF-8 as a function of pressure. Uptakes are calculated based on per gram of MOF and dual site Langmuir models were fitted to single-component gas adsorption isotherms.

The difference between adsorption performances of IL/MOF for different gases suggests that this material can be promising for separation of gases. Especially at low pressures, a remarkable increase in CO_2 selectivities can be expected because of the

improvement in the CO_2 adsorption capacity of ZIF-8 with the IL incorporation. In order to calculate the ideal gas selectivity of IL/MOF composite, dual site Langmuir models were fitted to single-component gas adsorption isotherms. The fit parameters are given in Appendix B. Figure 4.20 shows calculated ideal selectivities of ZIF-8 and [BMIM][PF_6]/ZIF-8 samples for CO_2/CH_4, CO_2/N_2, and CH_4/N_2 separations at room temperature up to 5 bar. As expected, CO_2 adsorbed more strongly than CH_4 and N_2 did in both pure MOF and IL/MOF composites. This behavior is attributed to its higher solubility in [BMIM][PF_6][137] and higher electrostatic interactions with the polar functional groups of ZIF-8.[139] Both CO_2/CH_4 and CO_2/N_2 selectivities of ZIF-8 were improved at low pressures after IL incorporation. IL/MOF composite was approximately two times more selective towards CO_2 over CH_4 than pure ZIF-8 up to 1 bar as shown in Figure 4.20(a). However, the most noticeable increase was observed for CO_2/N_2 selectivity of IL/MOF composite, which is almost three times of pure ZIF-8 up to 0.3 bar and two times of pure ZIF-8 up to 1 bar as shown in Figure 4.20(b). Even after 1 bar, gas separation performance of IL/ZIF-8 remains superior up to 5 bar. Both CO_2/CH_4 and CO_2/N_2 selectivities were considerably improved in this work compared to our previous study,[93] where CuBTC and [BMIM][BF_4] were used. Although the CO_2/CH_4 selectivity was better in pristine CuBTC than IL/CuBTC composite up to 5 bar, [BMIM][PF_6]/ZIF-8 showed higher CO_2/CH_4 separation performance compared to pure ZIF-8 at all pressures. The reason can be attributed to the interactions between MOF and IL: When the MOF with an unsaturated metal site (CuBTC) and the IL were strongly interacted, the competition between the CO_2 molecules and anion of the IL around the open metal site may cause a negative effect in gas adsorption performance.[128] Ban et al.[35] also reported higher CO_2/CH_4 and CO_2/N_2 selectivity values in [BMIM][Tf_2N]-loaded ZIF-8 membranes. This also supports the fact that when ZIF-8 was used as the MOF, the uptake amount of CO_2 was enhanced especially at low pressures. ZIF-8 does not have any open metal site, thus, CO_2 can easily dissolve in IL without facing any competition and interact better with the MOF surface modified by the presence of IL. Incorporation of IL into MOF shows less effect on CH_4 and N_2 adsorption, thus CH_4/N_2 selectivity could not make

any remarkable progress compared to the pristine ZIF-8. Figure 4.20(c) shows that CH_4/N_2 selectivity of IL/MOF composite could not reach the selectivity values of pristine ZIF-8 at any pressure step and it varied between 2 and 3 up to 5 bar for IL/MOF composite. At first, CH_4/N_2 selectivity of IL/ZIF-8 was closer to the one of ZIF-8 at low pressures, however, this value gradually reduced with an increase in pressure up to 5 bar. These results indicate that adsorption amounts of N_2 and CH_4 of IL/ZIF-8 composite decreased as a result of the reduction in pore volume with the confinement of IL into the structure, discussed above.

Ideal selectivity gives an idea about the gas separation performance of a material. However, gases exist as mixtures in reality, therefore, it is better to report mixture selectivities of materials. Measuring single-component gas adsorption isotherms of materials is possible by using some commercial instruments, however, similar type of measurements become very complex, expensive, and time consuming for gas mixtures.[162] Therefore, prediction of binary gas adsorption isotherms using reliable theoretical approaches is highly valuable. Ideal Adsorbed Solution Theory (IAST)[164] which has been commonly used for obtaining multi-component adsorption isotherms of porous materials using single-component adsorption isotherm data to predict mixture selectivities was used. Several studies in the literature[164-167] showed that IAST works well to predict adsorption behavior of gas mixtures in ZIFs. Binary gas mixture selectivities (CO_2/CH_4, CO_2/N_2, and CH_4/N_2, in a 50/50 mixture) of ZIF-8 and [BMIM][PF_6]/ZIF-8 samples calculated by IAST are shown in Figure 4.20. As the pressure approaches zero, selectivities obtained from IAST became almost the same as the ideal selectivities. This is expected because at low pressures gases do not interact with each other very much and behave as single-component gases. Figure 4.20(a) and (b) show that mixture selectivities were higher than the ideal selectivities. CO_2 is more strongly adsorbed than CH_4 and N_2 according to the single-component isotherms. Therefore, CO_2 molecules in the CO_2/CH_4 and CO_2/N_2 mixture occupy most of the adsorption sites that are also available for CH_4 and N_2 molecules. However, in the single-component adsorption, all sites are available

for all gas molecules. This competitive adsorption leads to higher mixture selectivities compared to ideal selectivities.

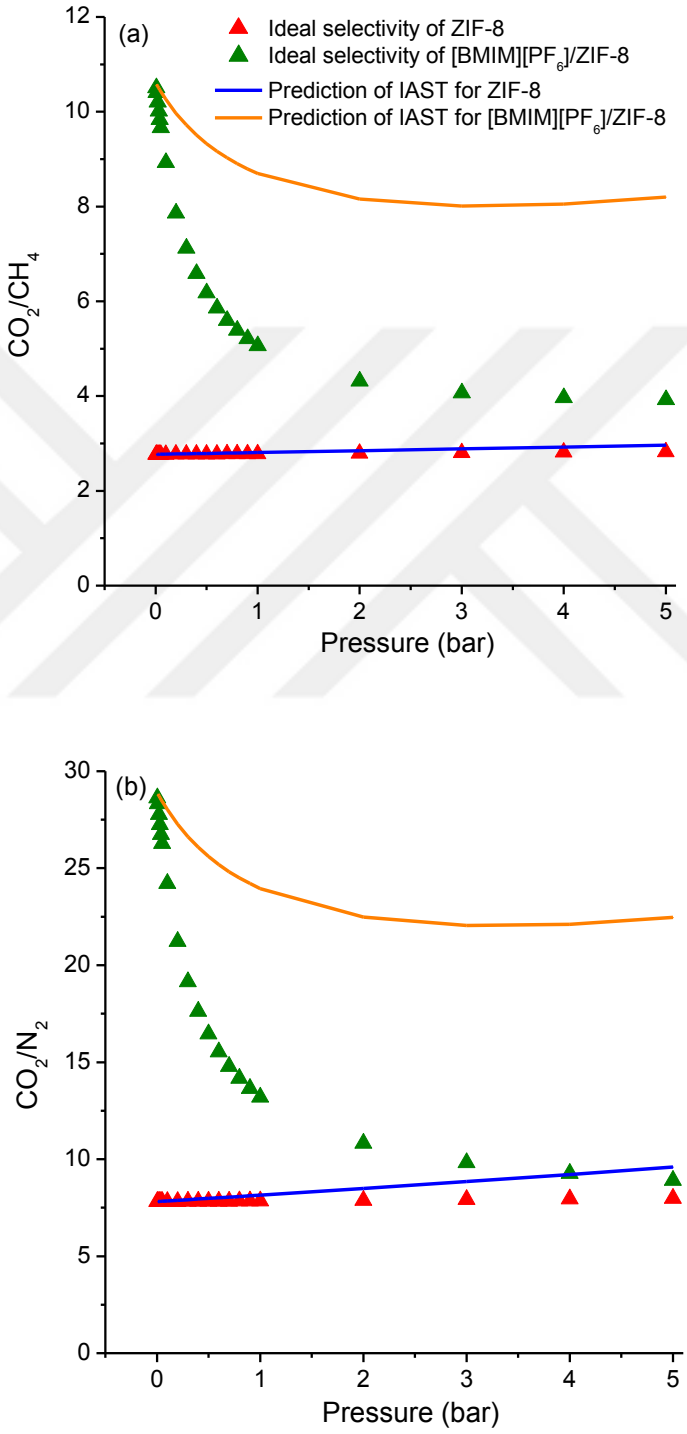

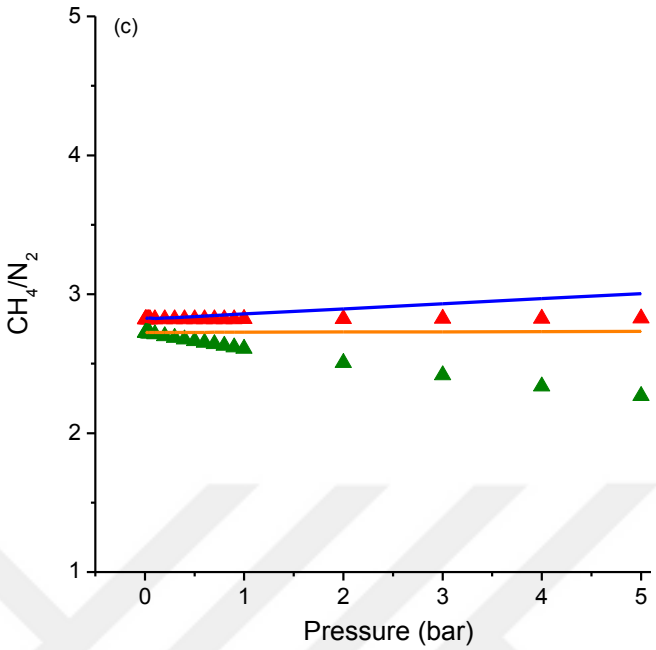

Figure 4.20. Ideal adsorption selectivities from Langmuir fits and IAST predictions (50/50 mixture) of ZIF-8 and [BMIM][PF_6]/ZIF-8 samples for (a) CO_2/CH_4, (b) CO_2/N_2, and (c) CH_4/N_2 at room temperature up to 5 bar.

In order to explain the change in selectivity with the incorporation of IL into the structure of ZIF-8, the difference of isosteric heats of adsorption of gas molecules was examined as an indicator of the interaction strength of gas molecules with the adsorbent. For instance, as Yang et al.[145] illustrated that the selectivity depends on the difference of isosteric heats at zero pressure, while with increasing pressure it starts to depend on structural factors such as available porosity. Figure 4.21 shows the ideal selectivities as a function of difference in isosteric heats of adsorption of gases for both ZIF-8 and [BMIM][PF_6]/ZIF-8.

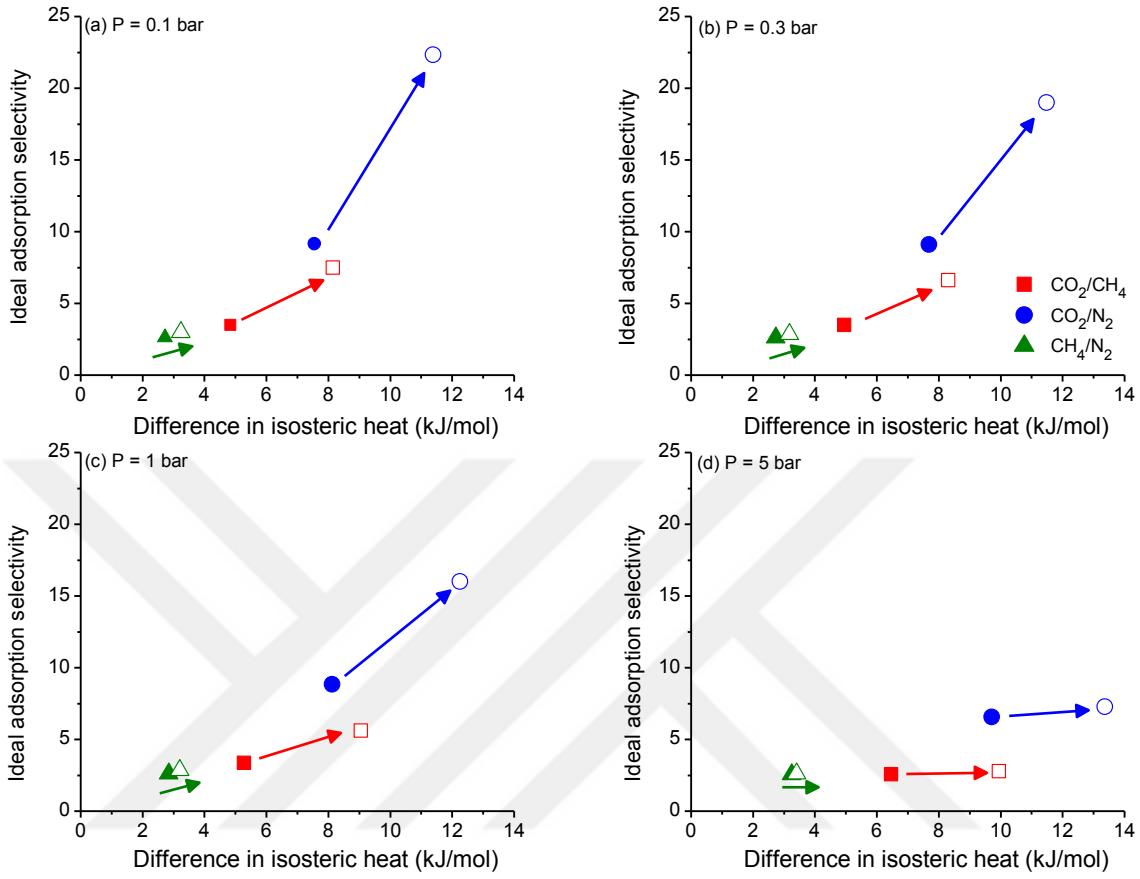

Figure 4.21. Comparison of ideal adsorption selectivities with the difference in isosteric heats of two gases at the adsorption pressure of (a) 0.1 bar, (b) 0.3 bar, (c) 1 bar, and (d) 5 bar at room temperature for CO_2/CH_4, CO_2/N_2, and CH_4/N_2 separations. Closed symbols represent ZIF-8 while open symbols representing [BMIM][PF_6]/ZIF-8. Arrows indicate the corresponding change upon the incorporation of IL into the MOF.

This figure illustrates that the difference in isosteric heats of adsorption between two gases is always higher for [BMIM][PF_6]/ZIF-8 system than the that for the pure ZIF-8. This behavior is directly attributed to the interactions between IL and MOF as discussed above. The highest heat of adsorption difference is observed between CO_2 and N_2 (7.56 kJ/mol for ZIF-8 and 11.38 kJ/mol for [BMIM][PF_6]/ZIF-8 as shown in Figure

4.21(a)), as a result the highest selectivity is observed for CO_2/N_2 in both ZIF-8 and [BMIM][PF_6]/ZIF-8. The increase in the difference of isosteric heat of adsorption is accompanied with an increase in ideal adsorption selectivity at lower pressures (0.1 and 0.3 bar), whereas with a further increase in pressure, this effect becomes less pronounced. For instance at 5 bar (Figure 4.21(d)), although there is always a positive difference between the heat of adsorption of gas species in ZIF-8 and [BMIM][PF_6]/ZIF-8, there is almost no change in selectivity. This behavior is more obvious for CO_2/CH_4 and CO_2/N_2 gas pairs. These results suggest that the interactions between IL and MOF are the dominant factor in determining the gas selectivity specifically at low pressures. Although it is noted that as the pressure goes up (above 1 bar), the dominant factor becomes the available space within the MOF cage. Thus it is concluded that elucidation of the interactions between ILs and MOFs is the key in rational design of such hybrid materials, with almost infinite number of possibilities, offering great potential for high performance gas separation applications.

Chapter 5: The Effect of Phosphonium-Based Ionic Liquid Incorporation on the Gas Adsorption and Separation Performances of ZIF-8 and CuBTC

To extend the knowledge about IL/MOF composites and their potential in gas adsorption/separation applications, phosphonium-based ILs were also incorporated into MOFs for the first time in the literature. Five different phosphonium-based ILs ([P_{4444}][TOS], [P_{4441}][$MeSO_4$], [$P_{(14)666}$][TMPP], [$P_{(14)666}$][Br], and [$P_{(14)666}$][DCA]) were incorporated into ZIF-8 and [$P_{(14)666}$][DCA] was incorporated into CuBTC. ZIF-8 and CuBTC were selected as MOFs because they have been combined with imidazolium-based ILs up to date and investigated in deep detail. Therefore, the effect of a different family of IL impregnation on the gas uptake and selectivity of ZIF-8 and CuBTC was investigated in this chapter. ZIF-8 was characterized in deep detail in Chapter 4, therefore no more discussion on this material will be included in this chapter. Characterization results of pristine CuBTC, phosphonium-based IL/ZIF-8, and phosphonium-based IL/CuBTC composites are given in the first part of Chapter 5. In the second part, results of gas adsorption measurements and gas selectivities are given along with their discussions.

5.1. Preparation of Phosphonium-Based IL/MOF Composites

All materials mentioned in this chapter (ZIF-8, CuBTC, [P_{4444}][TOS], [P_{4441}][$MeSO_4$], [$P_{(14)666}$][TMPP], [$P_{(14)666}$][Br], and [$P_{(14)666}$][DCA] and high purity acetone) have been purchased from Sigma-Aldrich. The chemical structures of phosphonium-based ILs can be seen in Figure 5.1. The preparations of composite materials were performed in open atmosphere using wet impregnation method (Chapter

3.1.1). After the samples were prepared and dried in oven overnight, they were sealed with Parafilm™ and stored in a desiccator to minimize water and impurity content. Resulting composite materials are named as $[P_{4444}][TOS]$/ZIF-8, $[P_{4441}][MeSO_4]$/ZIF-8, $[P_{(14)666}][TMPP]$/ZIF-8, $[P_{(14)666}][Br]$/ZIF-8, $[P_{(14)666}][DCA]$/ZIF-8, and $[P_{(14)666}][DCA]$/CuBTC as explained in Chapter 1.

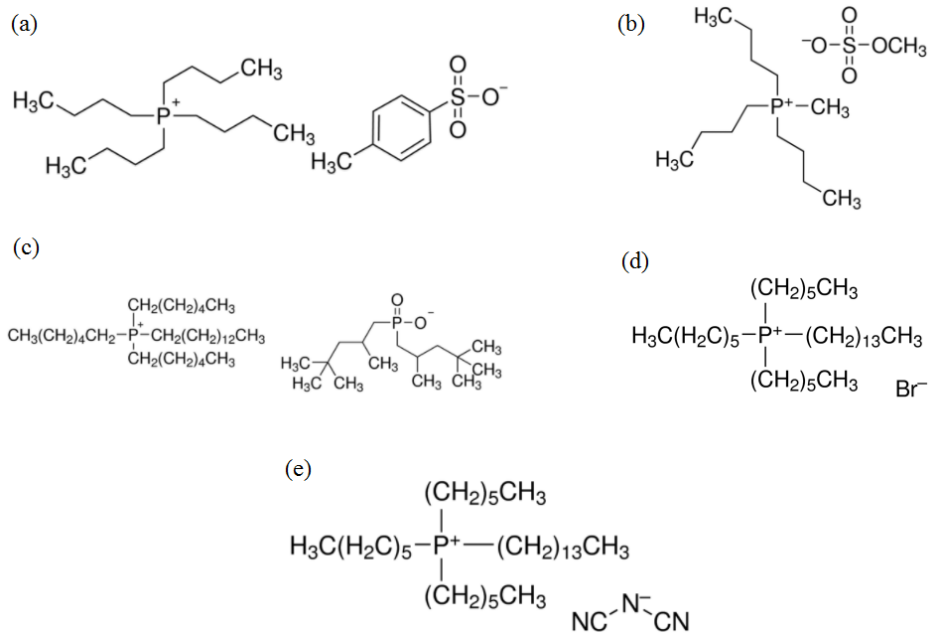

Figure 5.1. Chemical structures of phosphonium-based ILs used in this thesis study: (a) $[P_{4444}][TOS]$;[184] (b) $[P_{4441}][MeSO_4]$;[185] (c) $[P_{(14)666}][TMPP]$;[186] (d) $[P_{(14)666}][Br]$;[187] (e) $[P_{(14)666}][DCA]$[188]

5.1. Characterization of MOFs and Phosphonium-Based IL/MOF Composites

Physicochemical properties of both pristine CuBTC, phosphonium-based IL/ZIF-8, and phosphonium-based IL/CuBTC composites were analyzed by means of various characterization tools. As in the case of ZIF-8, the integrity of the crystal structures of CuBTC and phosphonium-based IL/MOF composites were checked using powder X-ray

diffraction. X-ray fluorescence analysis was conducted to determine the IL loading in composite material. Fourier transform infrared spectroscopy was performed to check the existence of IL in phosphonium-based IL/MOF composite as explained in Chapter 4. Thermal gravimetric analysis was made to determine the thermal stability limit of CuBTC and phosphonium-based IL/MOF composites. Scanning electron microscopy was used to understand the crystal morphology of MOFs after IL incorporation.

5.1.1. Characterization of Pristine CuBTC

Like ZIF-8, CuBTC was analyzed using several characterization methods, such as powder X-ray diffraction, scanning electron microscopy, thermal gravimetric analysis, BET surface area and pore volume analysis.

5.1.1.1. Powder X-Ray Diffraction (XRD) Results of CuBTC

XRD pattern of CuBTC was obtained using the parameters given in Chapter 3. The peaks were compared with the literature data as shown in Figure 5.2. As seen from the Figure 5.2, the XRD pattern obtained from the measurements conducted in this study is consistent with the pattern adapted from literature data.

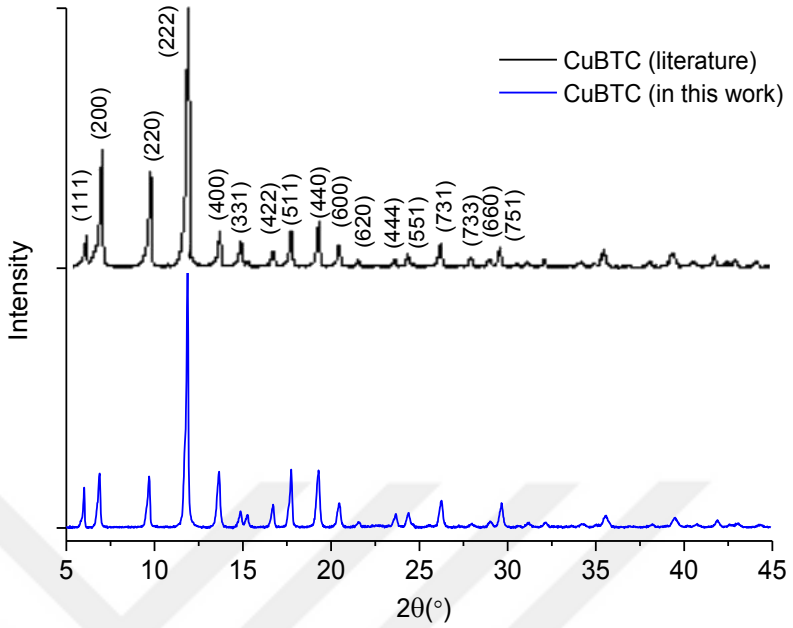

Figure 5.2. X-ray difftraction pattern of CuBTC used in this study (blue) and its comparison with XRD pattern adapted from literature (black)[189-190]

5.1.1.2. Scanning Electron Microscopy (SEM) Images of CuBTC

Surface characteristics of pristine CuBTC was investigated using scanning electron microscopy (SEM). With this method, crystal images of CuBTC at different magnifications were obtained. The parameters defined in Chapter 3 were used for the SEM analysis. Micrographs of CuBTC obtained in this thesis study are shown in Figure 5.3 and the SEM images obtained from the literature is given in Figure 5.4. These figures show that there is a coherency between the morphologies of CuBTC used in this study and taken from the literature.

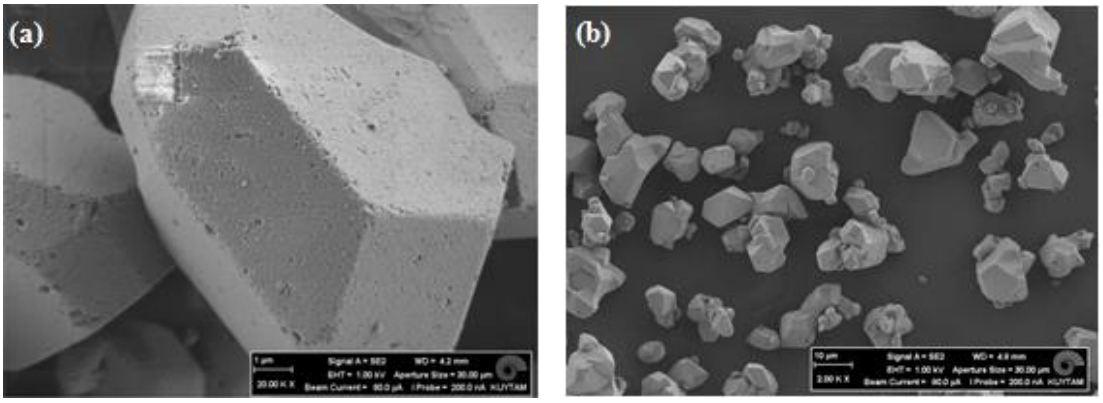

Figure 5.3. Morphology of CuBTC crystals at different magnifications: (a) 20,000x; (b) 2,000x.

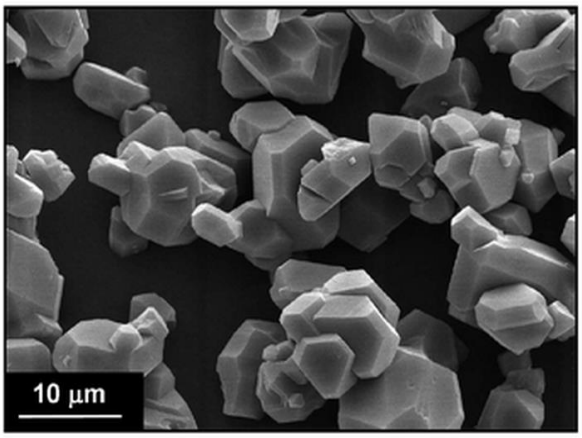

Figure 5.4. SEM image of CuBTC obtained from the literature.[191]

5.1.1.3. Thermal Gravimetric Analysis (TGA) Results of CuBTC

Thermal gravimetric analysis (TGA) was performed to specify the thermal decomposition temperature of CuBTC by measuring the weight loss with the increasing temperature. The analysis was performed using the same procedure used in the measurement of ZIF-8. The resulting weight percent change and derivative weight percent change with temperature diagrams are given in Figure 5.5.

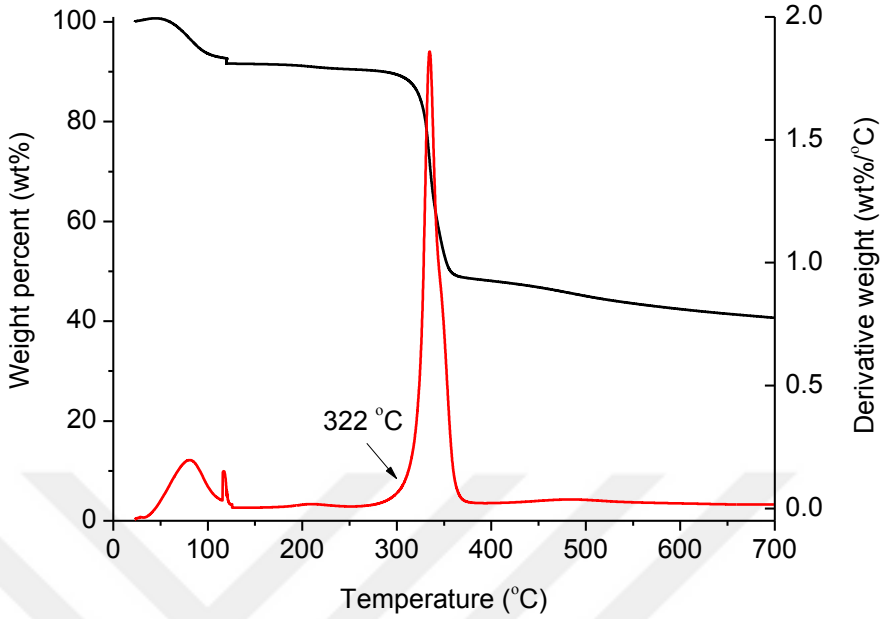

Figure 5.5. Thermal gravimetric analysis results for CuBTC. The black line and left *y*-axis shows weight percent change with temperature and the red line and right *y*-axis shows derivative weight percent change with temperature.

Figure 5.5 shows that CuBTC first loses 10 wt% of its initial weight until 150 °C because of the removal of water adsorbed on the sample. The weight percent is stable until around 320 °C followed by a weight loss of 40 wt% because of the decomposition of the framework. Then, another weight loss of 10 wt% was observed until 700 °C. The thermal decomposition temperature of CuBTC was obtained from the derivative onset temperature (T'_{onset}) as 322 °C. These results are consistent with TGA data of CuBTC obtained from literature given in Figure 5.6. Gimeno-Fabra et al.[192] reported 36 wt% of the initial weight was lost because of water desorption. The water content of the sample in this study is lower compared to the literature data because of the careful storage of CuBTC in a glovebox to minimize water adsorption. Another reason may be that CuBTC in this study was exposed to heating at 120 °C for 8 h during the analysis. Other weight

percent losses and thermal decomposition temperature of CuBTC are in agreement with the results obtained in this study.

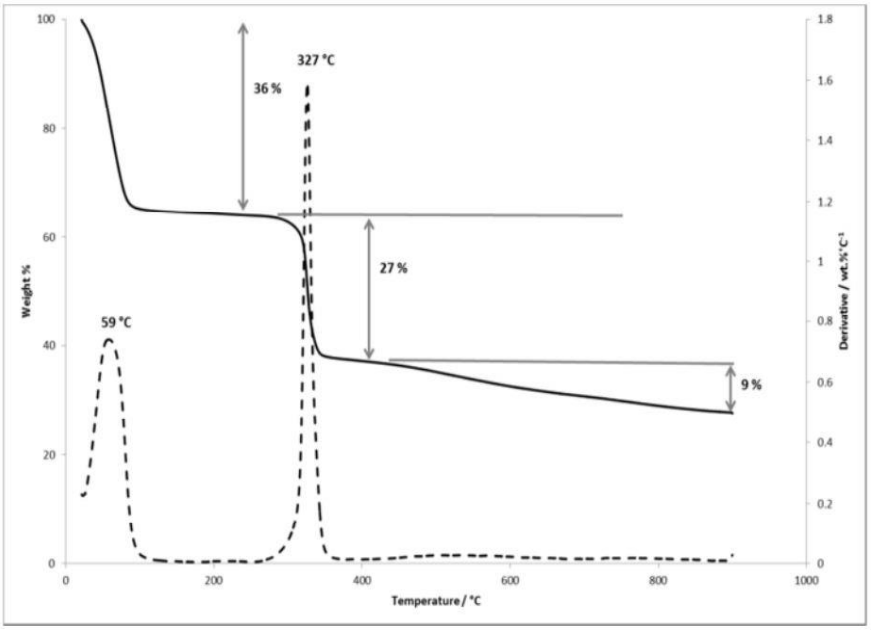

Figure 5.6. Thermal gravimetric analysis results for CuBTC adapted from work by Gimeno-Fabra et al.[192] Straight line and left *y*-axis shows weight percent change with temperature and dashed line and right *y*-axis shows derivative weight percent change with temperature.

5.1.1.4. Fourier Transform Infrared (FTIR) Spectroscopy Results of CuBTC

The vibrational features of CuBTC were investigated using FTIR spectroscopy. IR spectra of CuBTC was measured between spectral ranges from 4000 to 500 cm^{-1} with a resolution of 4 cm^{-1} using the parameters given in Chapter 3. The comparison with the literature data is also provided in Figure 5.7 that the IR peak positions of CuBTC obtained in this study are in agreement with the spectra reported in literature.[193] There are broad bands observed in the IR spectrum of CuBTC between 2800-3800 cm^{-1}, resulting from the H_2O adsorption in CuBTC. The peak at 1720 cm^{-1} is resulting from the C=O stretching

vibrations.[194] The peaks between 1700-1500 cm^{-1} and 1500-1300 cm^{-1} are attributed to C-O asymmetrical and symmetrical stretching, respectively.[194] The band at 1160 cm^{-1} is assigned to the C-C stretching vibration of alkyl chain.[194] There are also sharp peaks around 760 and 730 cm^{-1}, which are assigned to out of plane C-H bending of the framework.

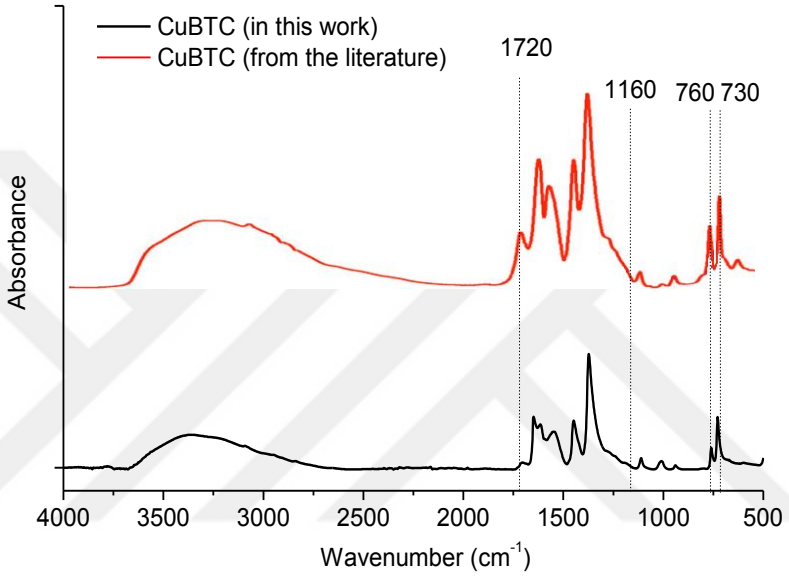

Figure 5.7. FTIR spectra of CuBTC obtained in the spectral range of 500-4000 cm^{-1}. Red line represents the experimental data obtained in this study and blue line shows the literature data.[193]

5.1.1.5. Brunauer-Emmett-Teller (BET) Surface Area Results of CuBTC

BET surface area measurements were used for the determination of the surface area and pore volume of pristine CuBTC. N_2 adsorption measurements were performed at -196 °C between 0-1 bar and surface area calculations were made using resulting isotherm data. The resulting adsorption and desorption isotherms are provided in Figure 5.8.

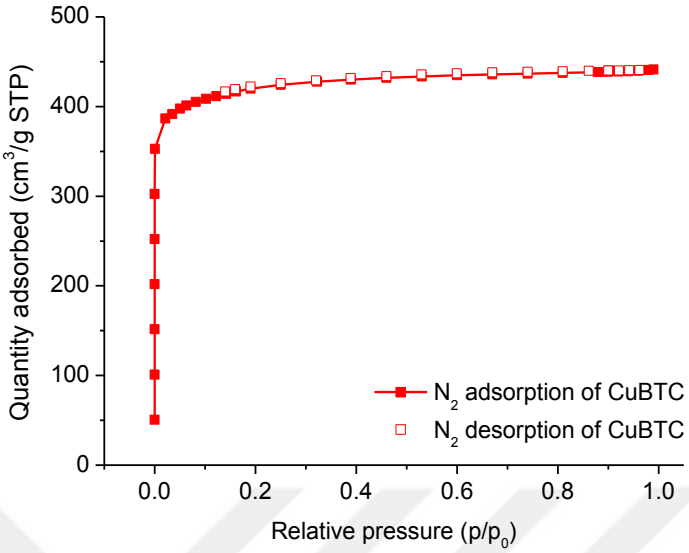

Figure 5.8. N_2 adsorption-desorption isotherm at -196 °C between 0-1 bar for CuBTC.

The BET surface area was calculated as 1324 m^2/g for CuBTC using the N_2 physisorption isotherm at -196 °C between relative pressures of 0.08-0.25 bar. In the literature, average surface areas of CuBTC were reported around 1300-1800 m^2/g.[195] The differences in the surfaces areas are probably because of different activation parameters made before the adsorption measurement, which was performed at 150 °C overnight in this study. Yoon et al.[196] activated CuBTC at 150 °C for 12 hours and reported a surface area of 1560 m^2/g. Variations in the synthesis procedures may be another reason for the slightly lower surface area obtained in this study. Majano and Perez-Ramirez[197] reported that synthesis time is an important parameter that they obtained surface areas between 1346 to 1749 m^2/g according to time given for crystallization. These results show that the surface area value of CuBTC obtained in this study is in a good agreement with the literature data.

5.1.2. Characterization of Pristine ZIF-8

Characterization experiments performed for pure ZIF-8 and their results with discussions were given in Chapter 4.2.1 in deep detail.

5.1.3. Characterization of Phosphonium-Based IL/MOF Composites

Phosphonium-based IL/MOF composites were characterized by the same techniques which was used for CuBTC. X-ray fluorescence (XRF) spectroscopy was additionally used to calculate the IL loading amount in phosphonium-based IL/MOF composites.

5.1.3.1. Powder X-Ray Diffraction Results of Phosphonium-Based IL/MOF Composites

Integrity of the crystal structures of phosphonium-based IL/MOF composites were investigated by powder X-ray diffraction method using the measurement parameters given in Chapter 3. The peak positions of CuBTC and ZIF-8 after phosphonium-based IL impregnation is provided in Figure 5.9 and Figure 5.10. The intensity values were normalized according to the highest peak observed in the measurements to compare the results accurately.

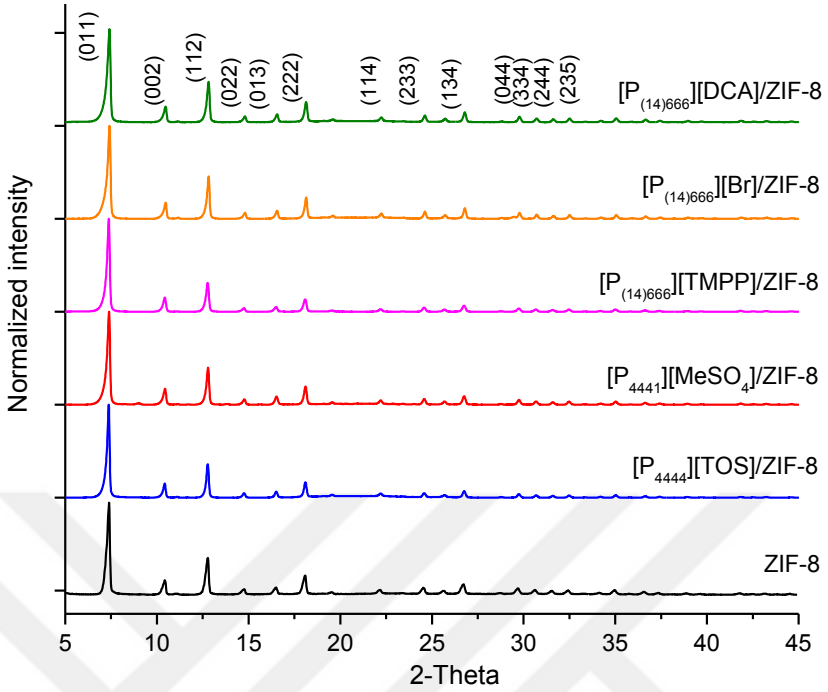

Figure 5.9. X-ray diffraction pattern of pristine ZIF-8 (black) and phosphonium-based IL/ZIF-8 composites.

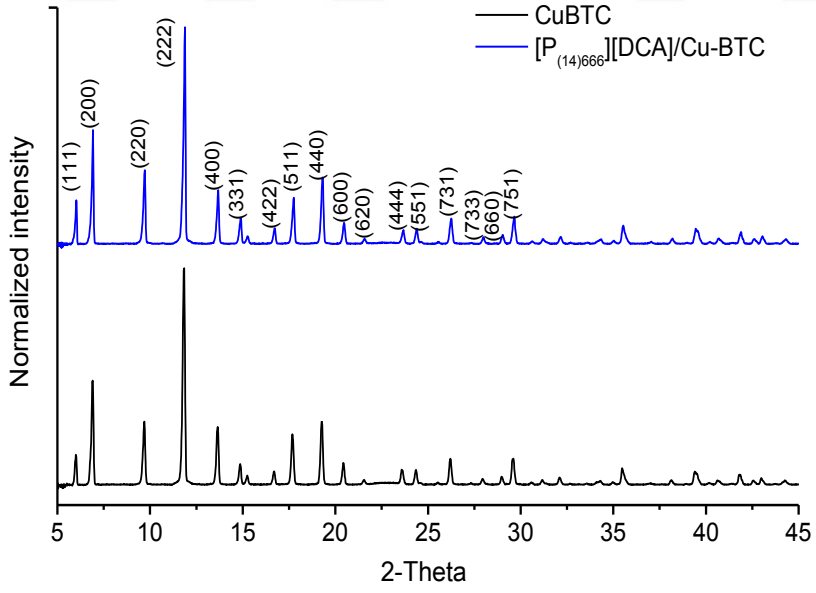

Figure 5.10. X-ray diffraction pattern of pristine CuBTC (black) and phosphonium-based IL/CuBTC composite.

As can be seen from Figure 5.9 and Figure 5.10, the characteristic peaks of ZIF-8 and CuBTC remain intact after incorporation of different types of phosphonium-based ILs. It was proved that there is no change in crystal structures of these two MOFs upon IL incorporation. This observation is consistent with the previous findings which is discussed in Chapter 4.

5.1.3.2. Scanning Electron Microscopy (SEM) Images of Phosphonium-Based IL/MOF Composites

As in Chapter 4, the morphology of phosphonium-based IL/MOF composites were investigated using scanning electron microscopy (SEM). SEM micrographs of IL/ZIF-8 and IL/CuBTC composites are given in Figure 5.11 and Figure 5.12, respectively. Images show that the frameworks of MOFs are stable after IL impregnation. Moreover, the shapes and sizes of phosphonium-based IL/MOF crystals are consistent with those of pristine ZIF-8 and CuBTC. Therefore, it is confirmed that crystal structure of MOFs were mostly preserved after phosphonium-based IL impregnation into the structure.

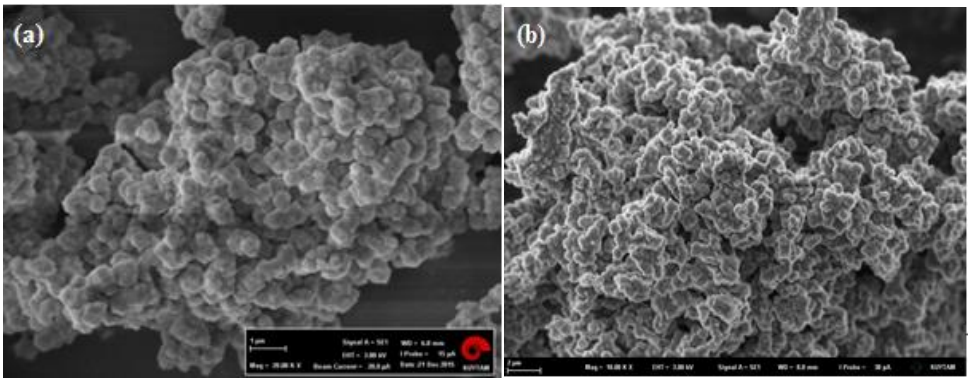

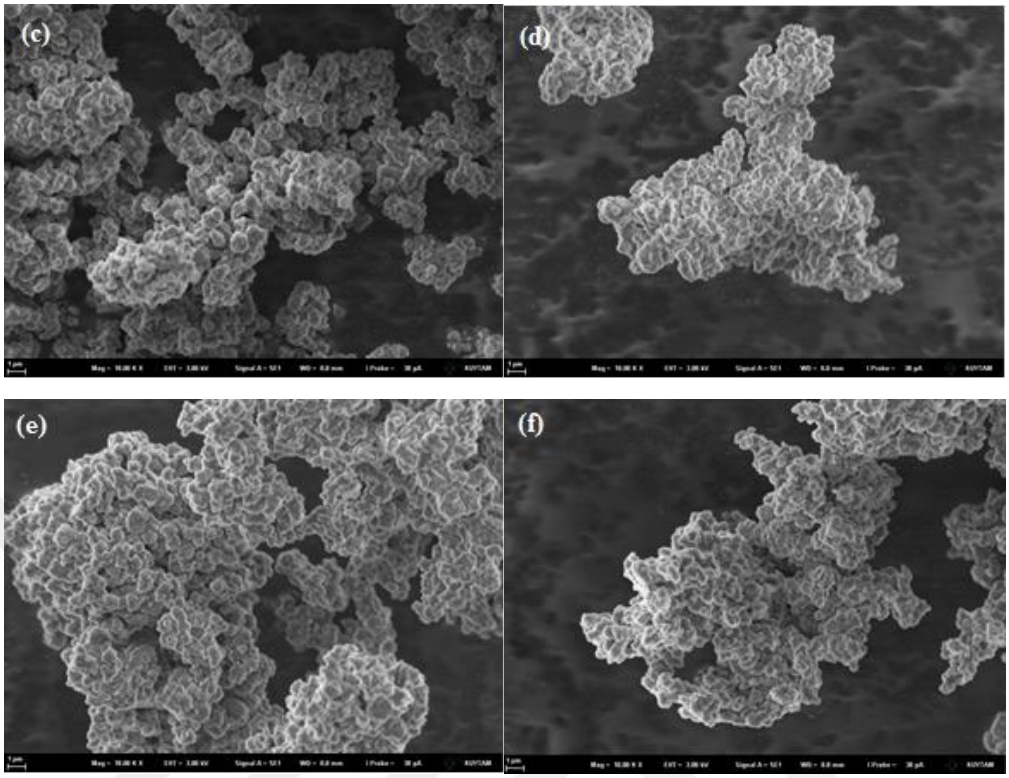

Figure 5.11. Morphology of pristine ZIF-8 and different phosphonium-based IL/ZIF-8 composites: (a) ZIF-8; (b) $[P_{4444}][TOS]$/ZIF-8; (c) $[P_{4441}][MeSO_4]$/ZIF-8; (d) $[P_{(14)666}][TMPP]$/ZIF-8; (e) $[P_{(14)666}][Br]$/ZIF-8; (f) $[P_{(14)666}][DCA]$/ZIF-8.

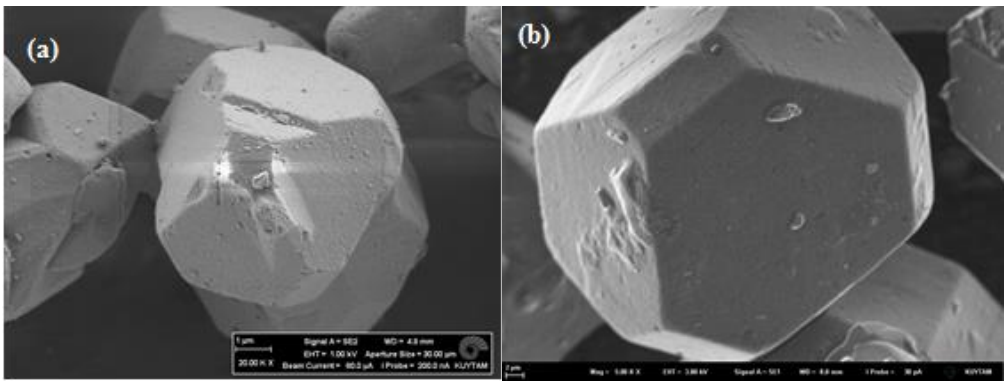

Figure 5.12. Morphology of pristine CuBTC and different phosphonium-based IL/CuBTC composites: (a) CuBTC; (b) $[P_{(14)666}][DCA]$/CuBTC.

5.1.3.3. X-Ray Fluorescence (XRF) Results of Phosphonium-Based IL/MOF Composites

X-ray fluorescence (XRF) analysis was conducted to calculate IL loading into the IL/MOF composites. The amounts of P, S, Zn, and Cu in phosphonium-based IL/ZIF-8 and phosphonium-based IL/CuBTC composites were obtained from the analysis and they were used to determine the loading of ILs inside phosphonium-based IL/MOF composites. The calculations were made as explained in Chapter 4.2.2.4. According to elemental concentration values, the IL loadings were calculated as shown in Table 5.1.

Table 5.1. IL loading in composite materials according to XRF measurements.

	[$P_{(14)666}$] [DCA]/ CuBTC	**[P_{4444}] [TOS]/ ZIF-8**	**[P_{4441}] [$MeSO_4$]/ ZIF-8**	**[$P_{(14)666}$] [TMPP]/ ZIF-8**	**[$P_{(14)666}$] [Br]/ ZIF-8**	**[$P_{(14)666}$] [DCA]/ ZIF-8**
IL loading (wt%)	6	28	28	25	29	22

5.1.3.4. Thermal Gravimetric Analysis (TGA) Results of Phosphonium-Based IL/MOF Composites

Thermal gravimetric analyses were performed to determine the thermal decomposition temperature of IL/MOF composites by measuring the weight loss with the increasing temperature. The weight percent and derivative weight percent changes for phosphonium-based ILs, pure MOFs, phosphonium-based IL/ZIF-8 and phosphonium-based IL/CuBTC composites are presented in Figure 5.13 and Figure 5.14, respectively. Data show that during a heating ramp to 700 °C under N_2 flow, phosphonium-based IL/ZIF-8 and phosphonium-based IL/CuBTC composites lost more weight than pristine ZIF-8 and CuBTC. This result was expected because the amount of decomposed IL was added to that of pristine MOF in phosphonium-based IL/MOF composites as explained in Chapter 4. T_{onset} and T'_{onset} temperatures obtained for ILs, MOFs, and phosphonium-

based IL/MOF composites from TGA measurement are given in Table 5.2. Results indicate that none of the composite materials could exceed the thermal stability of pristine MOFs. phosphonium-based IL impregnation lowered the starting thermal decomposition temperature of pristine MOFs as shown in Table 5.2. Such decrease was also observed in the thermal stability of metal-oxide-supported imidazolium ILs.[177] The thermal decomposition mechanisms of phosphonium-based IL/MOF composites are different from both pristine MOFs and ILs. After IL incorporation, all phosphonium-based IL/MOF composites have different amount of weight losses because of the variations in the thermal decomposition mechanisms.

TGA of the samples in Figure 5.13 and Figure 5.14 indicate that there is no significant weight loss in the samples because of the removal of adsorbed water. For ZIF-8, TGA measurement shows that it starts to decompose at 375 °C with an approximately 60 wt% of the initial mass remaining in the pan after a temperature ramp to 700 °C. For bulk $[P_{4444}][TOS]$, the decomposition starts at a temperature of 329 °C (determined from T'_{onset}) and IL completely disappears around 425 °C. The $[P_{4444}][TOS]$/ZIF-8 composite indicates a remaining mass of approximately 34 wt% of the initial mass. For an IL loading of approximately 28 wt% as determined by XRF measurements, approximately 43 wt% of the total mass of $[P_{4444}][TOS]$/ZIF-8 composite (which is nearly 60 wt% of the ZIF-8 amount in the $[P_{4444}][TOS]$/ZIF-8 sample, because of the decomposition of bulk IL completely at 700 °C) was expected to remain in the pan after the ramp to 700 °C. According to these results, the remaining mass in the pan was much less than the expected amount.

Similar calculations were made for the other phosphonium-based IL/MOF composites. For example, the thermal decompositions of bulk $[P_{(14)666}][TMPP]$ and $[P_{(14)666}][Br]$ start at 284 and 309 °C, and they completely disappear at the temperatures of 350 and 400 °C, respectively. The $[P_{(14)666}][TMPP]$/ZIF-8 and $[P_{(14)666}][Br]$/ZIF-8 composites show remaining mass of approximately 27 and 34 wt% of the initial masses, respectively. For the IL loadings of 25 wt% for $[P_{(14)666}][TMPP]$/ZIF-8 and 29 wt% for $[P_{(14)666}][Br]$/ZIF-8 composites as determined by XRF measurements, the remaining

masses in the pan were expected as 44 and 40 wt%, respectively. TGA measurements show that CuBTC starts to decompose at 312 °C with an approximately 57.5 wt% of the initial mass remaining in the pan after a temperature ramp to 700 °C. In the case of $[P_{(14)666}][DCA]$/CuBTC, bulk $[P_{(14)666}][DCA]$ starts to decompose at 328 °C and 4.5 wt% of bulk IL remains on the pan after 450 °C. The $[P_{(14)666}][DCA]$/CuBTC indicates remaining mass of 24 wt% of the initial mass after the analysis. According to XRF calculations, 54 wt% of the initial mass of $[P_{(14)666}][DCA]$/CuBTC is expected to remain on the pan at the end of the analysis.

TGA analysis results indicate that phosphonium-based IL/MOF composites behave different than their individual constituents (i.e. IL and MOF). Therefore, it can be concluded that there are direct interactions between phosphonium-based ILs and MOFs similar to the observations discussed in Chapter 4.

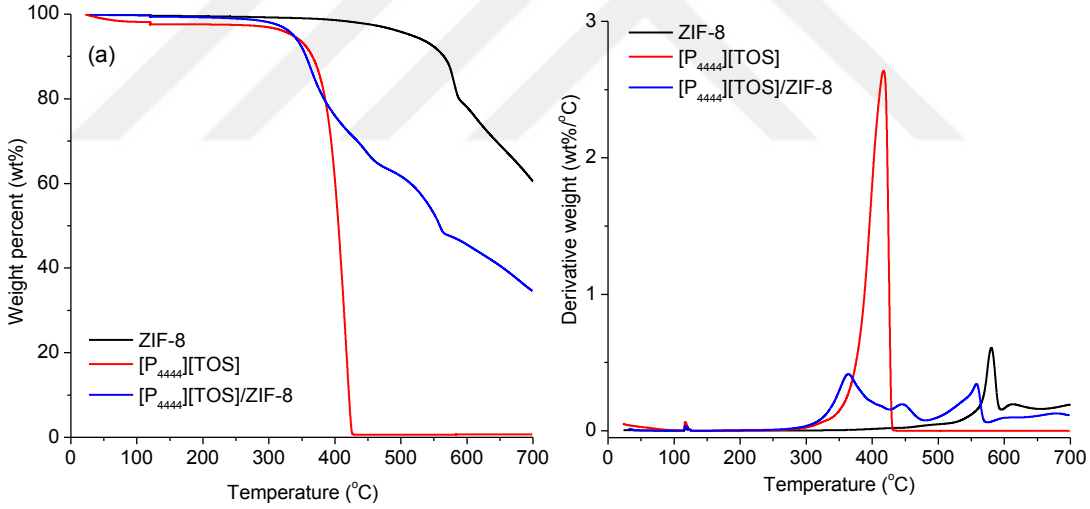

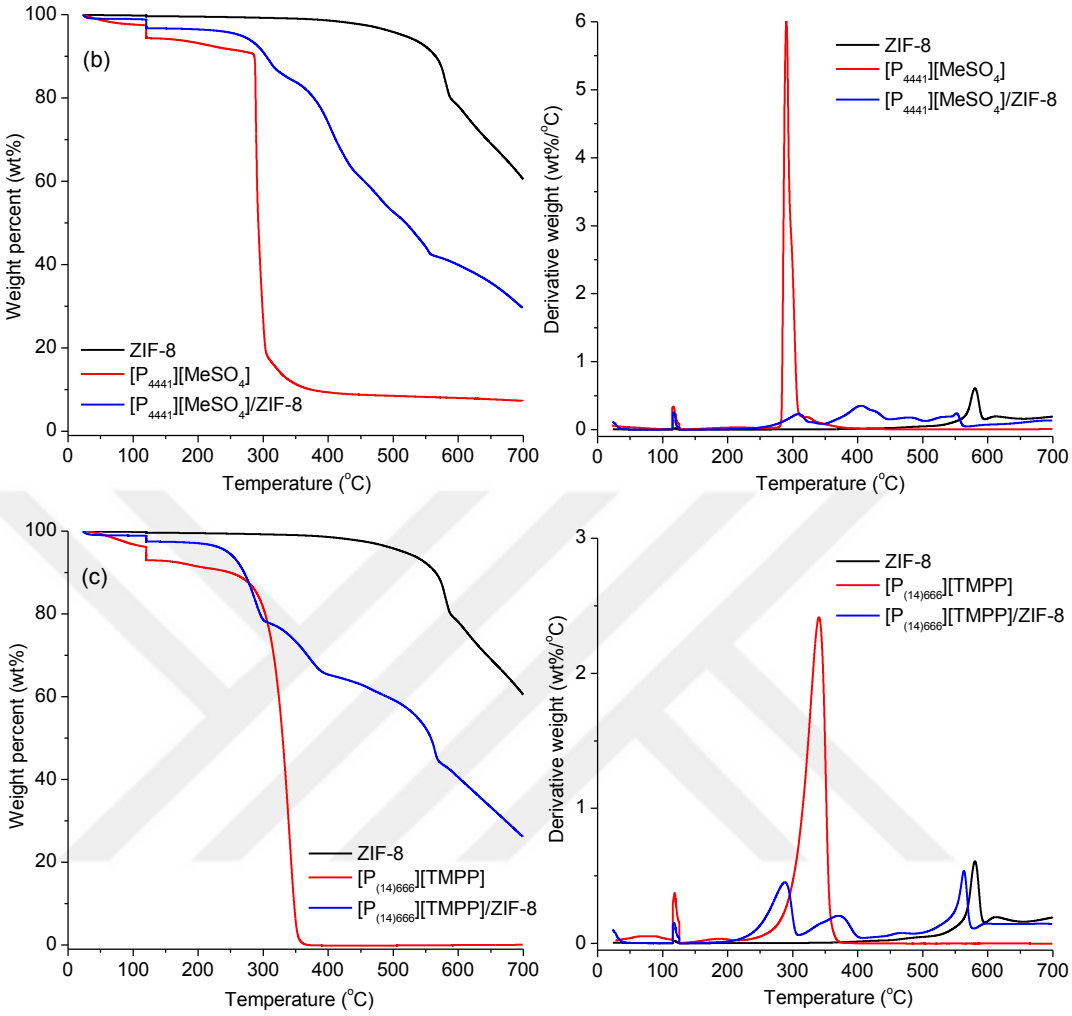
(b)
Weight percent (wt%)
Temperature (°C)
ZIF-8
[P4441][MeSO4]
[P4441][MeSO4]/ZIF-8
Derivative weight (wt%/°C)
Temperature (°C)
ZIF-8
[P4441][MeSO4]
[P4441][MeSO4]/ZIF-8
(c)
Weight percent (wt%)
Temperature (°C)
ZIF-8
[P(14)666][TMPP]
[P(14)666][TMPP]/ZIF-8
Derivative weight (wt%/°C)
Temperature (°C)
ZIF-8
[P(14)666][TMPP]
[P(14)666][TMPP]/ZIF-8

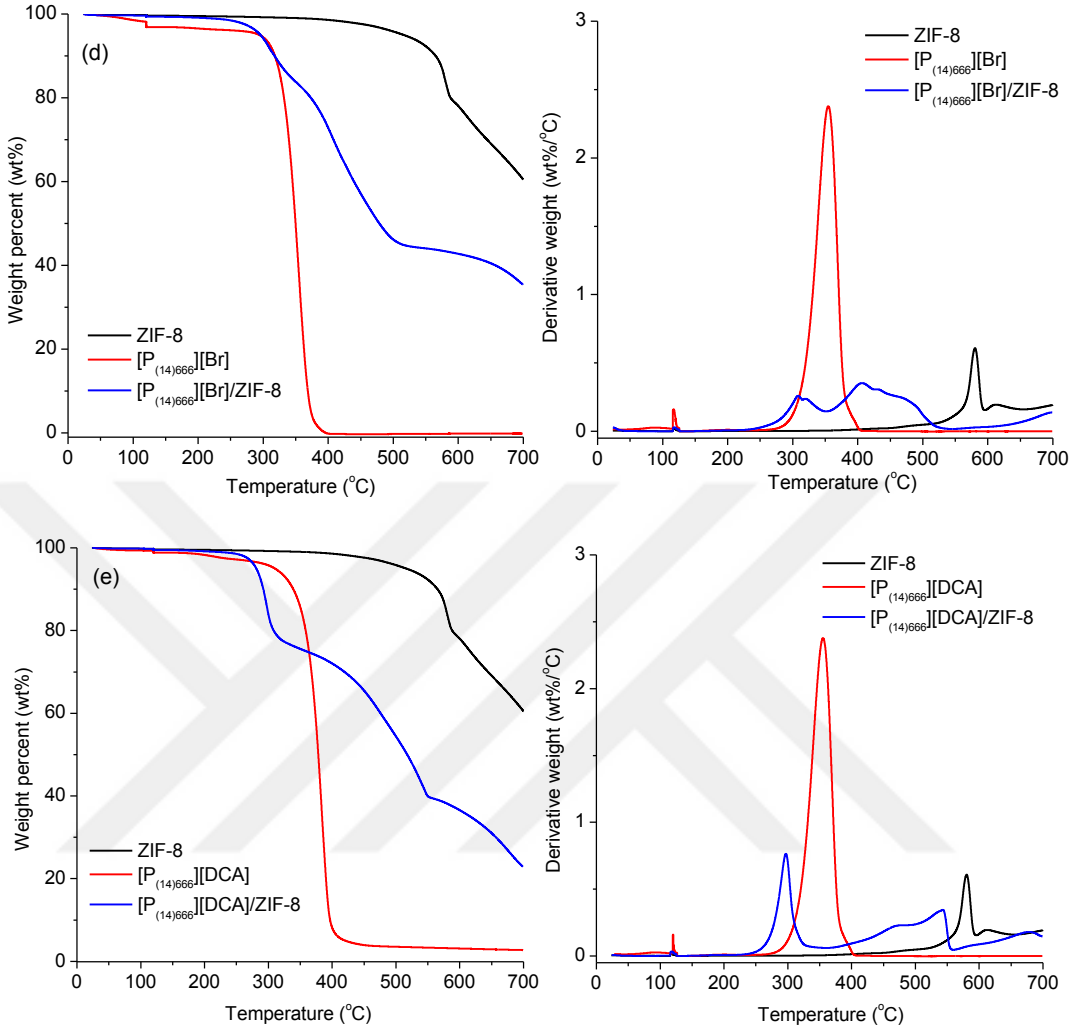

Figure 5.13. TGA results of ZIF-8, phosphonium-based ILs, and phosphonium-based IL/ZIF-8 composites regarding to the change of weight percent with increasing temperature and the change of derivative weight percent with increasing temperature: (a) $[P_{4444}][TOS]$/ZIF-8; (b) $[P_{4441}][MeSO_4]$/ZIF-8; (c) $[P_{(14)666}][TMPP]$/ZIF-8; (d) $[P_{(14)666}][Br]$/ZIF-8; (e) $[P_{(14)666}][DCA]$/ZIF-8.

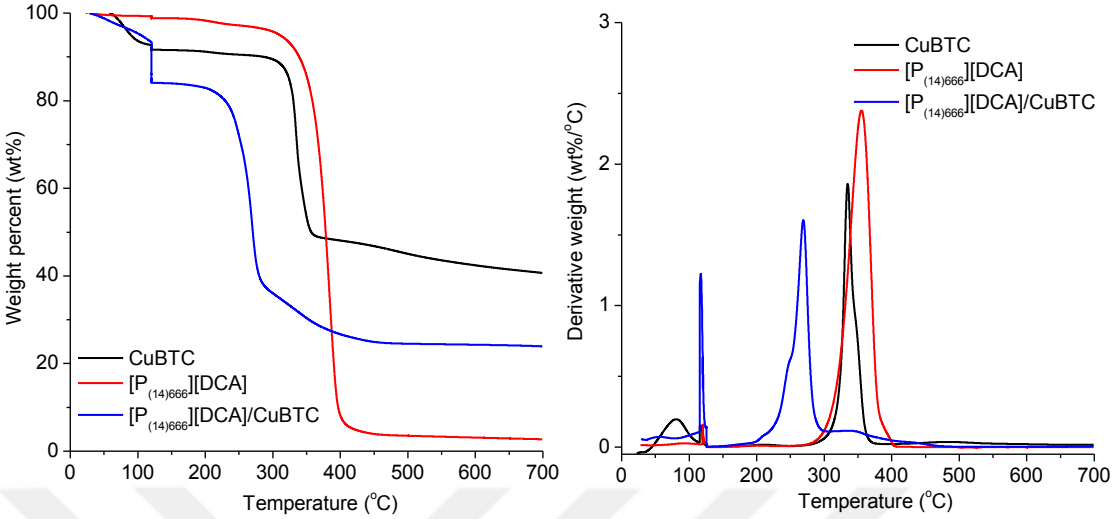

Figure 5.14. TGA results of CuBTC, $[P_{(14)666}][DCA]$, and $[P_{(14)666}][DCA]$/CuBTC composites regarding to the change of weight percent with increasing temperature and the change of derivative weight percent with increasing temperature.

Table 5.2. Onset temperatures and weight losses for ZIF-8, CuBTC, phosphonium-based ILs and phosphonium-based IL/MOF composites calculated from TGA measurements.

Sample	T_{onset} (°C)	T'_{onset} (°C)	Weight loss (%)
ZIF-8	382	375	40.3
CuBTC	316	312	42.5
$[P_{4444}][TOS]$	338	329	100
$[P_{4441}][MeSO_4]$	288	282	92.5
$[P_{(14)666}][TMPP]$	295	284	100
$[P_{(14)666}][Br]$	316	309	100
$[P_{(14)666}][DCA]$	331	328	95.5
$[P_{4444}][TOS]$/ZIF-8	327	311	65.4
$[P_{4441}][MeSO_4]$/ZIF-8	257	250	70.6

$[P_{(14)666}][TMPP]$/ZIF-8	236	222	73.4
$[P_{(14)666}][Br]$/ZIF-8	255	244	65.5
$[P_{(14)666}][DCA]$/ZIF-8	269	260	77.1
$[P_{(14)666}][DCA]$/CuBTC	220	212	76.1

5.1.3.5. Fourier Transform Infrared (FTIR) Spectroscopy Results of Phosphonium-Based IL/MOF Composites

As in Chapter 4, the existence of phosphonium-based ILs into IL/MOF composites is confirmed by Fourier transform infrared (FTIR) spectroscopy. Data for the bulk phosphonium-based ILs, ZIF-8, CuBTC, and phosphonium-based IL/ZIF-8 and phosphonium-based IL/CuBTC composites are presented in two different frequency regions, 3300-2800 cm^{-1} (for $[P_{(14)666}][DCA]$/ZIF-8 and $[P_{(14)666}][DCA]$/CuBTC, 3200-2000 and 1700-500 cm^{-1}) as can be seen from Figure 5.15 and Figure 5.16.

In every phosphonium-based IL/MOF composite, there are some peaks belonging to phosphonium-based ILs which shows that IL incorporation can be observed from the IR spectrum. Although the assignment of the IR peaks belonging to phosphonium-based ILs were not fully accomplished in the literature, some of the peaks were assigned using the information in the literature. For all samples, the peaks between 2800-3000 cm^{-1} are resulting from CH stretching or CH_3 stretching.[198] For $[P_{4444}][TOS]$/ZIF-8, the peaks at 1383 and 752 cm^{-1} were assigned to P–C stretching,[198-199] 1189 and 573 cm^{-1} were assigned to O=S=O bending[200] and 1283 cm^{-1} was assigned to P-C_4H_9 deformation band of the IL.[198] For $[P_{4441}][MeSO_4]$/ZIF-8, the peaks at 1215, 1248, 1091, 1017, and 911 cm^{-1} were assigned to C–O–SO_3[201] stretching and the peak at 722 cm^{-1} was assigned to P–C stretching of the IL.[198] For $[P_{(14)666}][TMPP]$/ZIF-8, the peaks at 1200 and 722 cm^{-1} were assigned to P–C stretching[198] and the peak at 1150 cm^{-1} was assigned to P=O stretching of the IL.[202] For $[P_{(14)666}][DCA]$/ZIF-8 and $[P_{(14)666}][DCA]$/CuBTC, the peaks at 2190 and 2127 cm^{-1} were assigned to C≡N stretching and 830 cm^{-1} was assigned to

symmetric/asymmetric C-N-C vibration of the IL.[203] As a result, the incorporation of all phosphonium-based ILs were investigated and their presence in composite materials was proved with FTIR analysis.

For the further investigation of IL-MOF interactions in the composites, the IR spectra of phosphonium-based ILs, MOFs and phosphonium-based IL/MOF composites were deconvoluted by employing Voigt function with Fityk[132] software. The deconvoluted spectra of the materials are given in Appendix B. As discussed in Chapter 4, the interactions between ILs and MOFs cause some shifts in the IR bands of ILs. First, the IR spectra of the materials in the range of 500-1750 cm^{-1} were investigated. The IR bands of $[P_{4444}][TOS]$ at 661, 677, 1345, 1413, 1589, and 1656 cm^{-1} showed some red and blue shifts (by 5, 7, -10, -10, 6, and 9 cm^{-1}, respectively) in $[P_{4444}][TOS]$/ZIF-8. For $[P_{4441}][MeSO_4]$, the peaks at 668, 1046, 1268, and 1417 cm^{-1} were shifted to 660, 1053, 1263, and 1426 cm^{-1} in $[P_{4441}][MeSO_4]$/ZIF-8 by showing some red and blue shifts. The IR bands of $[P_{(14)666}][TMPP]$ at 704, 734, 774, 1342, 1449, and 1650 cm^{-1} presented red and blue shifts (by -10, 8, -14, -7, -12, and 6 cm^{-1}, respectively) in $[P_{(14)666}][TMPP]$/ZIF-8. The vibration bands of $[P_{(14)666}][Br]$ at 734, 743, 1013, 1298, 1322, 1357, and 1469 cm^{-1} showed red and blue shifts (by 5, 5, -10, -12, -6, -6, -7, and 7 cm^{-1}) after it was incorporated into ZIF-8. For $[P_{(14)666}][DCA]$, the peaks at 606, 786, 892, 1045, 1159, 1247, 1291, 1304, 1341, 1378, 1467, 1600 and 1690 cm^{-1} were shifted in $[P_{(14)666}][DCA]$/ZIF-8 composite to 618, 777, 899, 1052, 1150, 1241, 1285, 1297, 1336, 1373, 1476, 1594, and 1680 cm^{-1}, respectively. For the same IL, the peaks at 668, 697, 709, 786, 1368, 1378 cm^{-1} showed red shifts (by -5, -11, -5, -6, -5, -5, 5) and the peak at 1600 shifted to 1605 cm^{-1} by presenting blue shift. In the case of $[P_{(14)666}][DCA]$, the peak at 1600 cm^{-1} showed red shift (by -6 cm^{-1}) in $[P_{(14)666}][DCA]$/ZIF-8 composite while it showed blue shift (by 5 cm^{-1}) in $[P_{(14)666}][DCA]$/CuBTC composite. This result indicate that the interaction between phosphonium-based ILs and MOFs may be different according to the types of the MOFs.

The IR vibrations of the composites in the region 2800-3300 cm^{-1} were also investigated. No significant shifts were observed in this region for $[P_{4444}][TOS]$/ZIF-8

and $[P_{4441}][MeSO_4]$/ZIF-8 composites. The peaks of $[P_{(14)666}][TMPP]$ at 2815 and 2988 cm^{-1} were shifted to 2810 and 2983 cm^{-1} in $[P_{(14)666}][TMPP]$/ZIF-8, respectively. For $[P_{(14)666}][Br]$, the IR bands of 2853, 2871, and 2955 cm^{-1} presented red shifts (by -6, -5, and -11 cm^{-1}) in $[P_{(14)666}][Br]$/ZIF-8. The vibration bands of $[P_{(14)666}][DCA]$ at 2138, 2178, 2211, 2224, 2854, and 2925 cm^{-1} showed red and blue shifts (by 10, -9, 10, 8, -6, and -9 cm^{-1}) in $[P_{(14)666}][DCA]$/ZIF-8 composite while the bands at 2871 and 2893 cm^{-1} shifted to 2863 and 2901 cm^{-1} in $[P_{(14)666}][DCA]$/CuBTC, respectively. According to these shifts, it can be said that ILs can interact in different ways with different kinds of MOFs. These shifts in the IR regions show that there are some interactions between phosphonium-based ILs and MOFs.

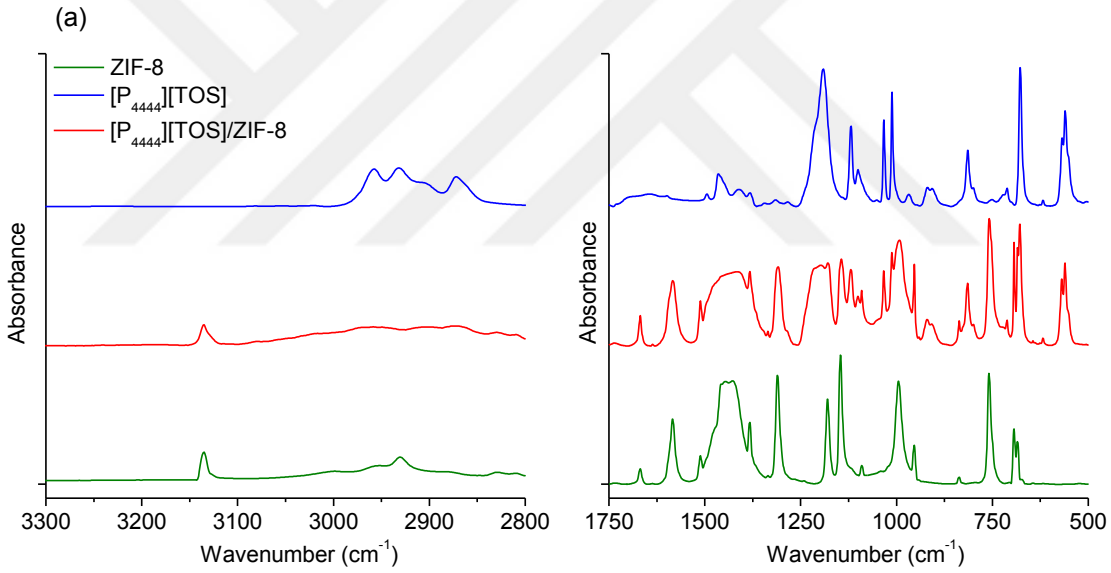

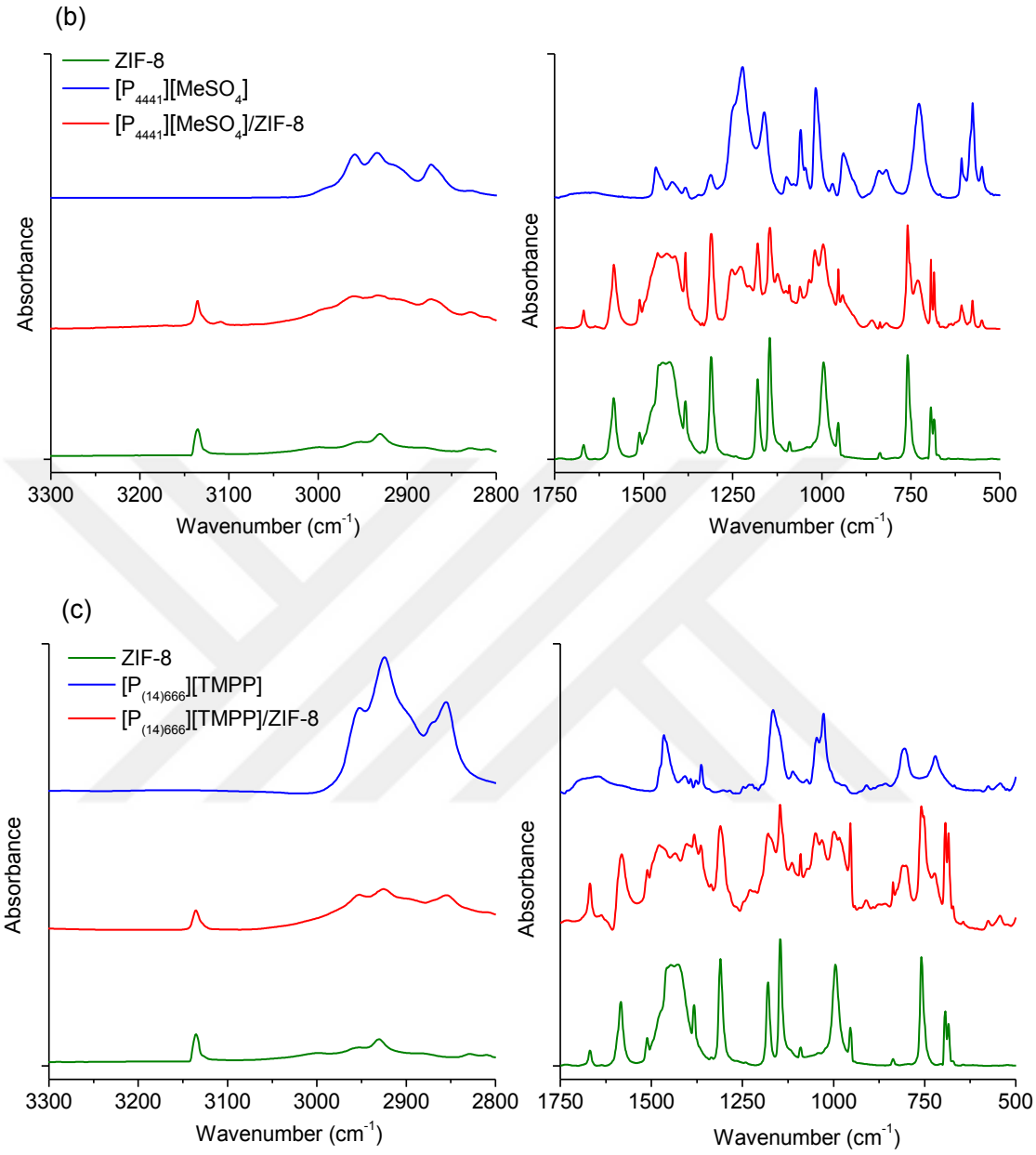
(b)
ZIF-8
[P4441][MeSO4]
[P4441][MeSO4]/ZIF-8
Absorbance
3300
3200
3100
3000
2900
2800
Wavenumber (cm-1)
1750
1500
1250
1000
750
500
Wavenumber (cm-1)
(c)
ZIF-8
[P(14)666][TMPP]
[P(14)666][TMPP]/ZIF-8
Absorbance
3300
3200
3100
3000
2900
2800
Wavenumber (cm-1)
1750
1500
1250
1000
750
500
Wavenumber (cm-1)

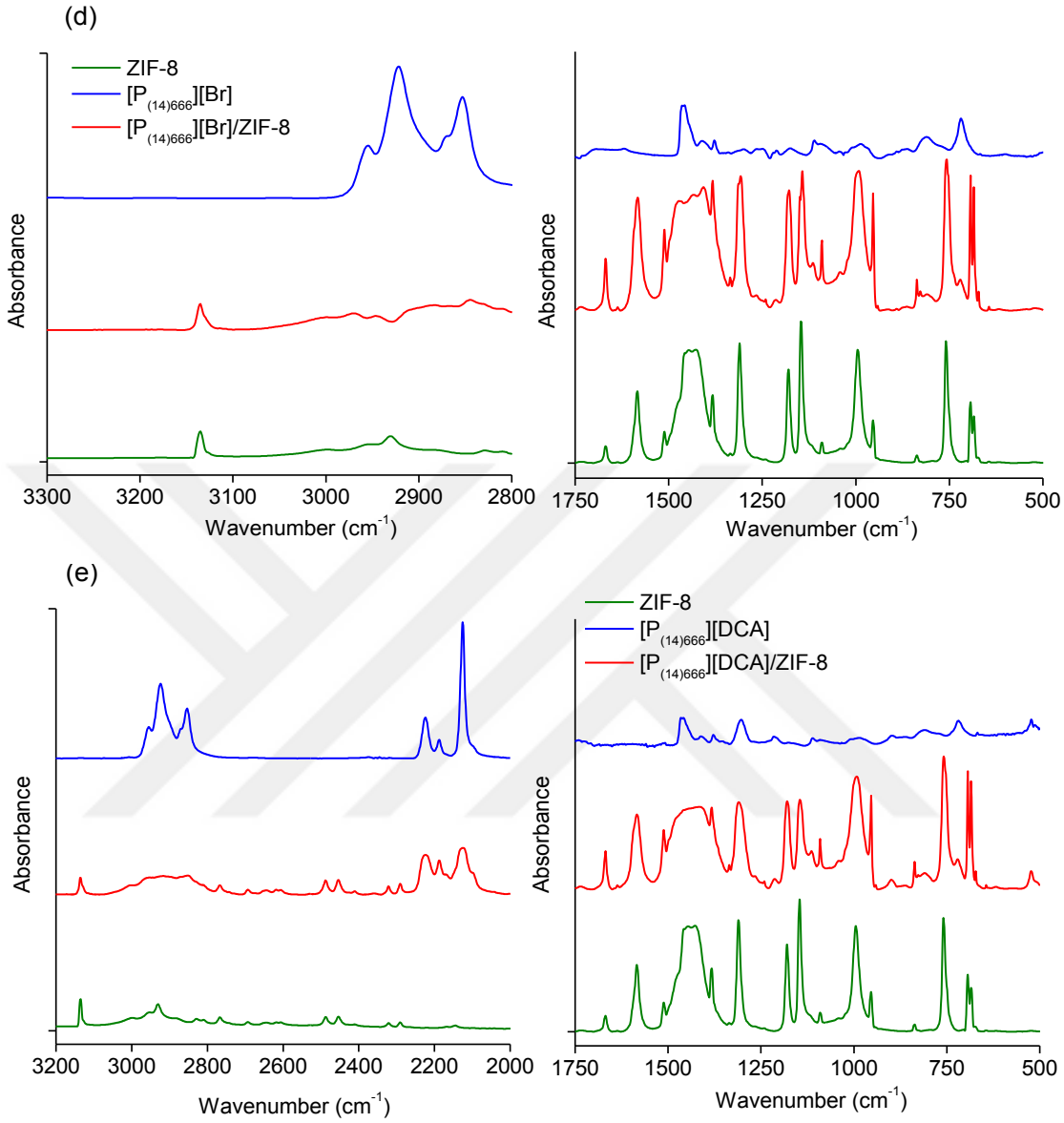

Figure 5.15. FTIR spectra of ZIF-8, IL/ZIF-8 samples, and phosphonium-based ILs between 3300-2800 cm^{-1} (for $[P_{(14)666}][DCA]$/ZIF-8, 3200-2000 cm^{-1}) and 1700-500 cm^{-1}. Samples are given respectively: (a) $[P_{4444}][TOS]$/ZIF-8; (b) $[P_{4441}][MeSO_4]$/ZIF-8; (c) $[P_{(14)666}][TMPP]$/ZIF-8; (d) $[P_{(14)666}][Br]$/ZIF-8; (e) $[P_{(14)666}][DCA]$/ZIF-8.

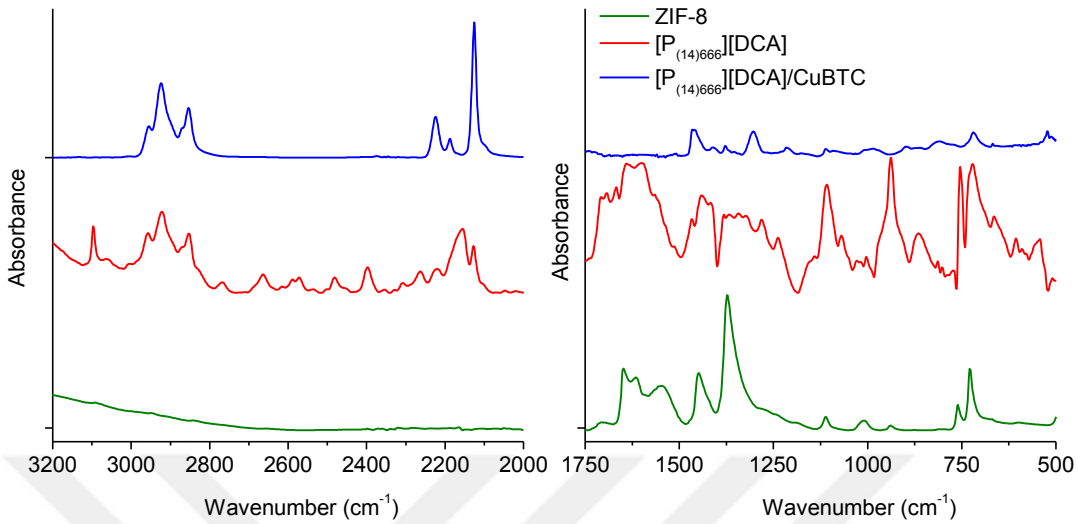

Figure 5.16. FTIR spectra of CuBTC, $[P_{(14)666}][DCA]$/CuBTC composite, and $[P_{(14)666}][DCA]$ between 3200-2000 cm^{-1} and 1700-500 cm^{-1}.

5.2. Gas Adsorption Measurements

Gas adsorption measurements were conducted experimentally using the same gases and the pressure range considered in Chapter 4. The aim was to investigate the effect of incorporation of phosphonium-based ILs instead of imidazolium-based ILs on the gas adsorption and separation performance of pristine MOFs. The comparison of gas adsorption performance of ZIF-8 obtain in this study and in the literature was also given in Chapter 4. In this part, first all gas uptakes of CuBTC are given and compared with the ones in the literature. Then, adsorption measurements were performed for phosphonium-based IL/ZIF-8 and phosphonium-based IL/CuBTC composites with the same gases in Chapter 4. Ideal gas selectivity for all gas pairs were calculated by dividing the single-component gas uptake data and CO_2/CH_4, CO_2/N_2, and CH_4/N_2 selectivity for all phosphonium-based IL/MOF composites were obtained.

5.2.1. Gas Adsorption Analysis of ZIF-8

Gas adsorption measurements performed for ZIF-8 were given in Chapter 4 and discussed in detail. CH_4, CO_2, and N_2 isotherms obtained for ZIF-8 can be found in Figure 4.16, Figure 4.17, and Figure 4.18, respectively.

5.2.2. Gas Adsorption Analysis of CuBTC

Gas adsorption measurements for CuBTC were performed experimentally according to the procedure explained in Chapter 3. CuBTC was activated at 150 °C overnight under high vacuum (10^{-6} bar) to eliminate all the adsorbed molecules (especially water molecules) on the surface of the pores. CO_2, CH_4, and N_2 gas uptakes were obtained between 0.1-30 bar as shown in Figure 5.17.

Experimental gas uptakes obtained in this study were also compared with the literature data as shown in Figure 5.18. Results obtained in this study are in a good agreement with the adsorption data in the literature[204-206] especially in the low pressure region (between 0-1 bar). While the CH_4 and CO_2 adsorption isotherms in the literature were obtained at almost the same temperature with our study, the temperature is slightly higher in the work by Moellmer et al.[206] Therefore, the difference in the N_2 adsorption isotherms is more obvious compared to CH_4 and CO_2 measurements.

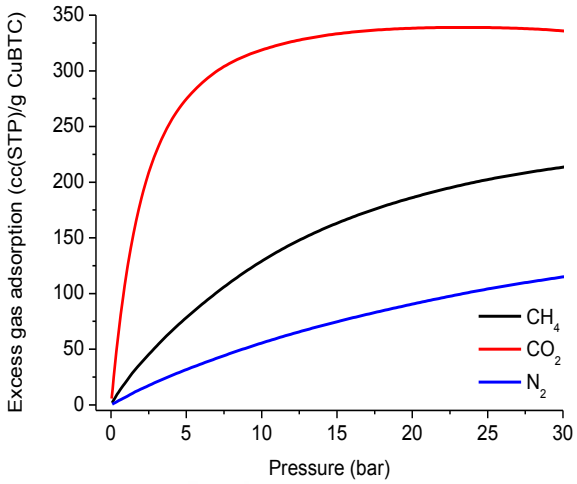

Figure 5.17. Single-component adsorption isotherms of CO_2, CH_4, and N_2 in CuBTC

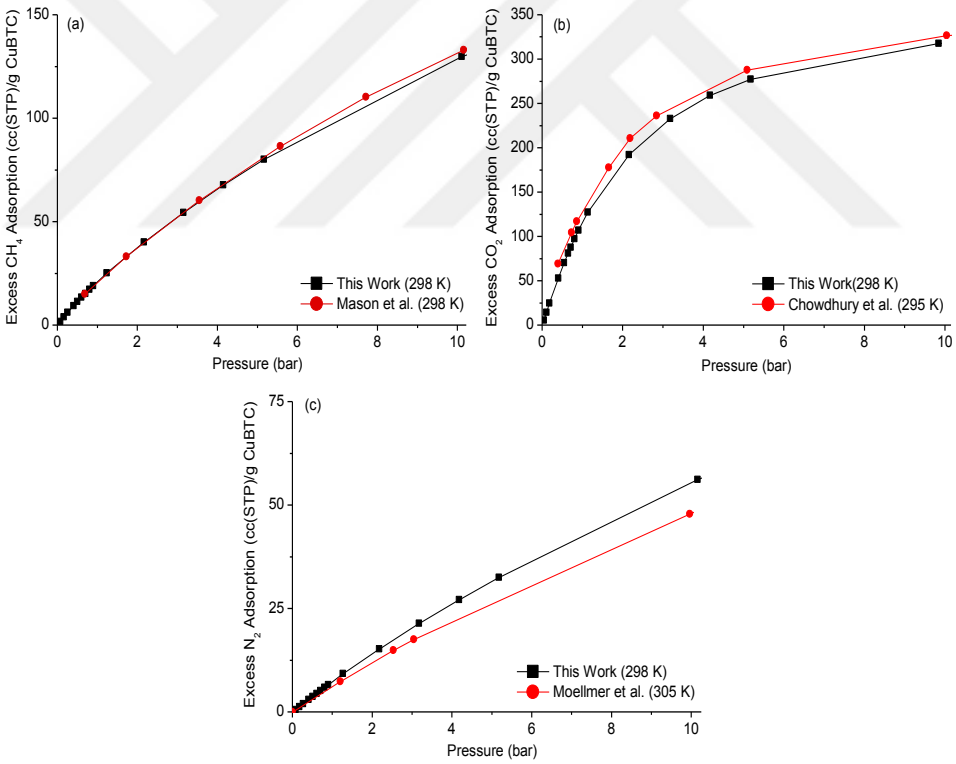

Figure 5.18. Comparison of the gas adsorption isotherms of CuBTC with the literature for (a) CH_4[204]; (b) CO_2[205]; (c); N_2[206]. Analysis temperatures are indicated in the legends of the plots.

5.2.3. Gas Adsorption Analysis of Phosphonium-Based IL/MOF Composites

Gas adsorption measurements were conducted for phosphonium-based IL/ZIF-8 and phosphonium-based IL/CuBTC composites up to 30 bar as shown in Figure 5.19. Gas uptakes are given for per gram of ZIF-8 and CuBTC in order to compare the performances of composites with the pristine MOFs. The aim is to improve the gas adsorption amount of 1 gram of pristine MOF material, therefore it is needed to calculate excess adsorption amounts of composites per gram of MOF. Gas adsorption results per gram of composite materials are also provided in Appendix B. Although [BMIM][PF_6] incorporation could increase only CO_2 gas uptake of ZIF-8 up to 0.4 bar, impregnation of phosphonium-based IL molecules could improve the gas adsorption performances of pristine MOFs. CH_4 adsorption measurements showed that [P_{4444}][TOS]/ZIF-8 and [$P_{(14)666}$][TMPP]/ZIF-8 composites could surpass the CH_4 uptake of pristine ZIF-8 after 1 bar. The difference in the uptakes of pristine ZIF-8 and [P_{4444}][TOS]/ZIF-8 is more obvious especially at higher pressures that ZIF-8 has 88.62 g/cm^3 CH_4 uptake while [P_{4444}][TOS]/ZIF-8 has 100.35 g/cm^3 at 30 bar. Similarly, [P_{4444}][TOS]/ZIF-8, [$P_{(14)666}$][TMPP]/ZIF-8, and [P_{4444}][Br]/ZIF-8 composites have also higher CO_2 and N_2 adsorption capacities compared to pristine ZIF-8 while [$P_{(14)666}$][TMPP]/ZIF-8 showed better N_2 adsorption capacity compared to pristine ZIF-8. Only [P_{4441}][$MeSO_4$]/ZIF-8 showed no remarkable enhancement in gas adsorptions compared to those of pristine ZIF-8. Results show that phosphonium-based ILs have the potential for creating new adsorption sites for CH_4, CO_2, and N_2 gases. This result is probably originated from the presence of IL into MOF structure and its interactions with the framework.

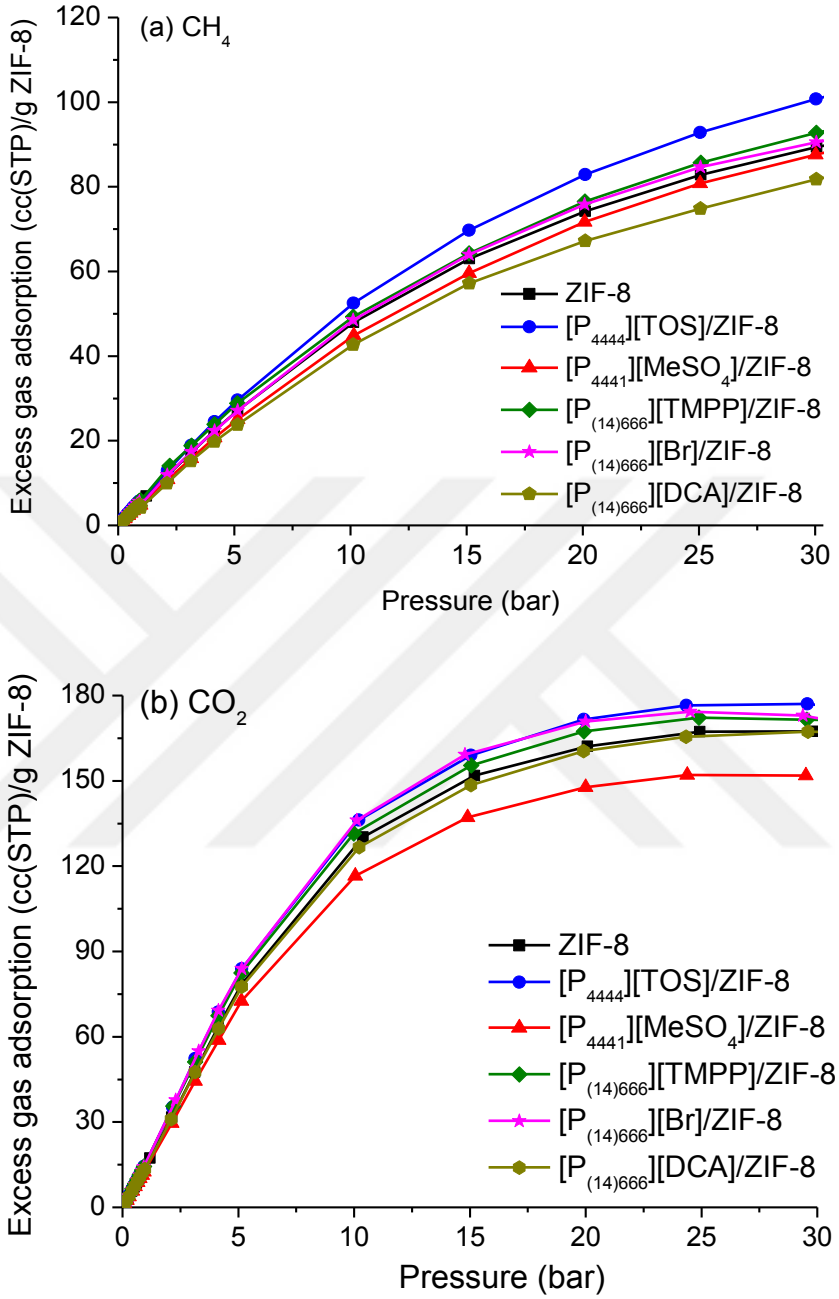
(a) CH4
Excess gas adsorption (cc(STP)/g ZIF-8)
Pressure (bar)
ZIF-8
[P4444][TOS]/ZIF-8
[P4441][MeSO4]/ZIF-8
[P(14)666][TMPP]/ZIF-8
[P(14)666][Br]/ZIF-8
[P(14)666][DCA]/ZIF-8
(b) CO2
Excess gas adsorption (cc(STP)/g ZIF-8)
Pressure (bar)
ZIF-8
[P4444][TOS]/ZIF-8
[P4441][MeSO4]/ZIF-8
[P(14)666][TMPP]/ZIF-8
[P(14)666][Br]/ZIF-8
[P(14)666][DCA]/ZIF-8

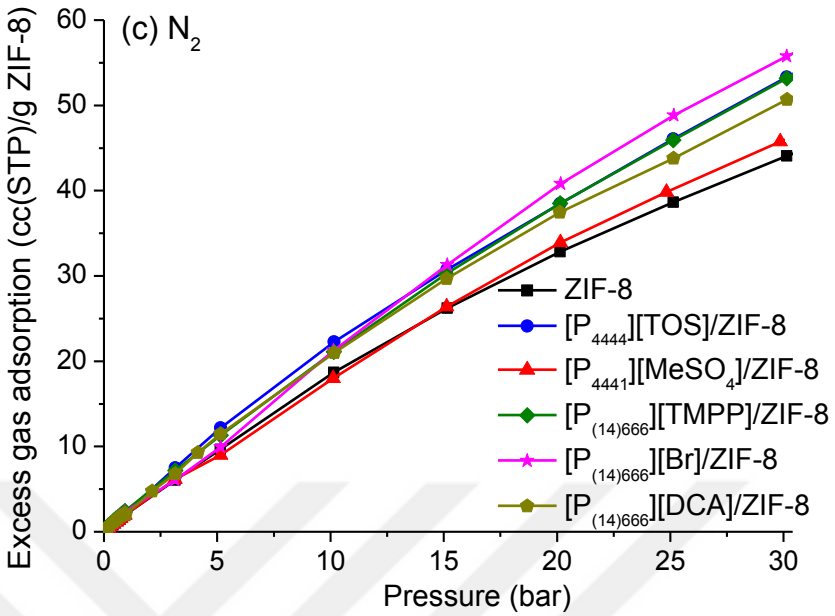

Figure 5.19. Comparison of the adsorption isotherms for (a) CO_2, (b) CH_4, and (c) N_2 for both pristine ZIF-8 and phosphonium-based IL/ZIF-8 composites.

For investigating the effect of phosphonium-based IL impregnation on different types of MOFs, CuBTC was selected as the second support material. The same gas measurements were also performed for $[P_{(14)666}][DCA]$/CuBTC composite as shown in Figure 5.20. Unlike ZIF-8, none of the gas uptakes of CuBTC was improved with phosphonium-based IL impregnation. In this case, IL impregnation could not create gas adsorption sites for gas molecules. Because of the partial occupancy of the pores of CuBTC by IL molecules, available pore volume for gas adsorption was reduced. Sezginel et al.[93] reported a similar behavior in CuBTC that when $[BMIM][BF_4]$ was impregnated into CuBTC structure, all gas uptakes (CH_4, CO_2, N_2, and H_2) decreased compared to those of pristine CuBTC.

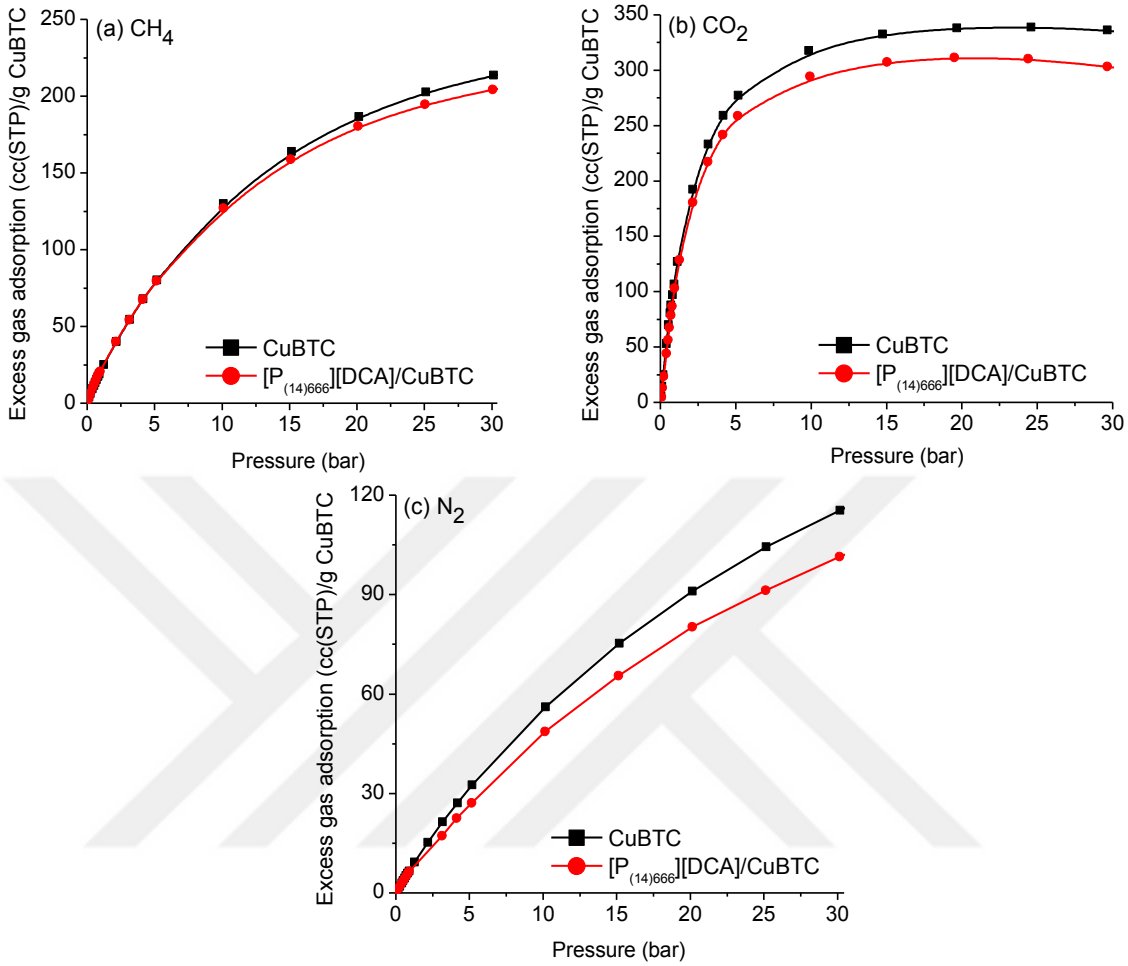

Figure 5.20. Comparison of the adsorption isotherms for (a) CO_2, (b) CH_4, and (c) N_2 for both pristine CuBTC and phosphonium-based IL/CuBTC composite**.**

The adsorption performances of phosphonium-based IL/MOF composites are different for each gas, therefore these materials may have potential to be used in gas separation applications. With this aim, gas selectivities were calculated for phosphonium-based IL/ZIF-8 and phosphonium-based IL/CuBTC composite materials. Ideal gas selectivities were calculated by dividing adsorption isotherms after they were fitted using dual site Langmuir and Freundlich models as in the Chapter 4. The fit parameters are given in Appendix B. CO_2/CH_4, CO_2/N_2, and CH_4/N_2 separations at room temperature up

to 5 bar are given for phosphonium-based IL/ZIF-8 and phosphonium-based IL/CuBTC composites in Figure 5.21 and Figure 5.22, respectively.

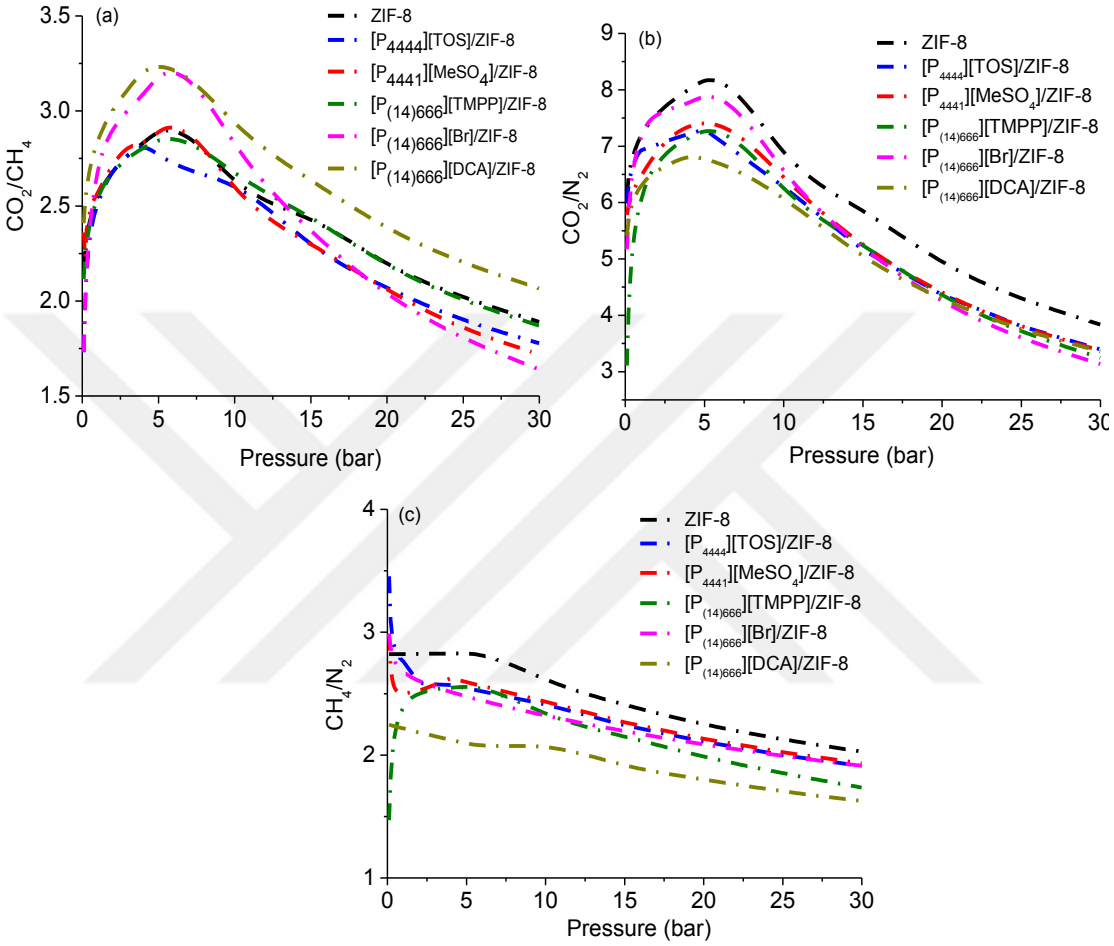

Figure 5.21. Ideal adsorption selectivities from Langmuir and Freundlich fits of ZIF-8 and phosphonium-based IL/ZIF-8 samples for (a) CO_2/CH_4, (b) CO_2/N_2, and (c) CH_4/N_2 at room temperature up to 5 bar.

For phosphonium-based IL/ZIF-8 composites, there are no significant enhancements in the selectivities by contrast with imidazolium-based IL/ZIF-8 composite. For CO_2/CH_4 separation, only $[P_{(14)666}][Br]/ZIF-8$ and $[P_{(14)666}][DCA]/ZIF-8$ composites has slightly higher selectivities compared to pristine ZIF-8 as shown in Figure

5.21(a). At 5 bar, CO_2/CH_4 selectivities are 2.88, 3.18, and 3.23 for ZIF-8, $[P_{(14)666}][Br]$/ZIF-8, and $[P_{(14)666}][DCA]$/ZIF-8, respectively. In the case of $[BMIM][PF_6]$/ZIF-8, the composite material was more than 2 times selective towards CO_2 over CH_4 than pure ZIF-8 up to 1 bar. Therefore, it can be concluded that phosphonium-based ILs are less advantageous than imidazolium-based ILs for improving the CO_2/CH_4 separation of ZIF-8. Similarly, a slight increase was obtained in the CH_4/N_2 selectivity of ZIF-8 that $[P_{4444}][TOS]$/ZIF-8 composite has 1.25 times of pure ZIF-8 at 0.1 bar. CO_2/N_2 selectivity of ZIF-8 was not improved with the impregnation of any of the phosphonium-based ILs as can be seen in Figure 5.21(b) while the most noticeable enhancement was observed for CO_2/N_2 selectivity in $[BMIM][PF_6]$/ZIF-8 composite as discussed in Chapter 4. These observations show that phosphonium-based ILs are disadvantageous for the incorporation into ZIF-8 when they are compared with imidazolium-based ILs, which exhibit remarkable gas separation performances combined with different MOFs as reported in different studies.[35, 43, 93]

Similar measurements were performed on the composite material which was prepared with most promising IL for improving the CO_2/CH_4 separation of ZIF-8, $[P_{(14)666}][DCA]$, and CuBTC as the support material. The aim was to understand whether phosphonium-based ILs works better with a different type of MOF in terms of gas separation performance. Results in Figure 5.22 show that only a slight improvement was obtained in CH_4/N_2 separation with IL incorporation into CuBTC structure. For example, selectivity was enhanced from 2.84 to 3.33 with $[P_{(14)666}][DCA]$ confinement. Surprisingly, $[P_{(14)666}][DCA]$/CuBTC composite did not show better CO_2/CH_4 selectivity than that of CuBTC. This result shows that the behavior of IL changes when it is incorporated into different types of MOFs, thus there are infinite number of possibilities to obtain remarkable gas separation performances.

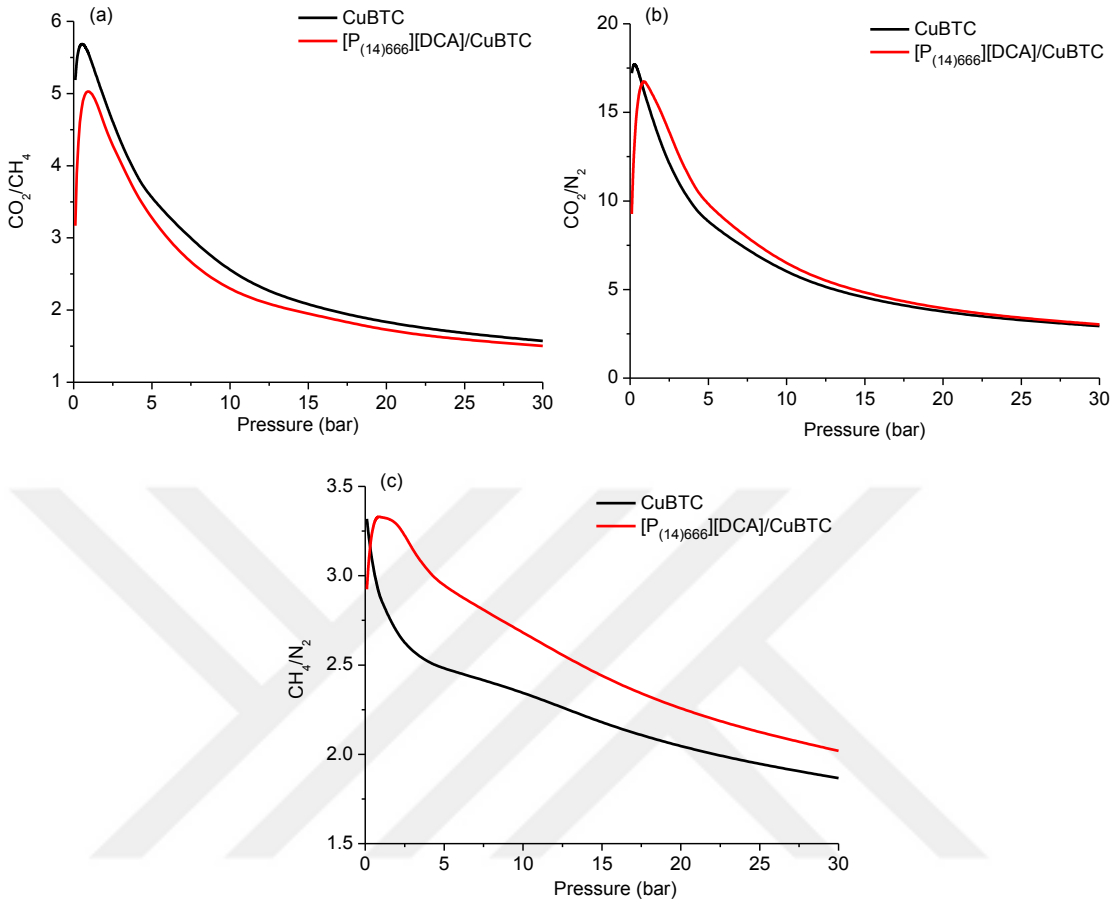

Figure 5.22. Ideal adsorption selectivities from Langmuir and Freundlich fits of CuBTC and phosphonium-based IL/CuBTC samples for (a) CO_2/CH_4, (b) CO_2/N_2, and (c) CH_4/N_2 at room temperature up to 5 bar.

In summary, data presented here illustrate that while phosphonium-based IL incorporation can enhance the gas adsorption amount of per gram of MOF, it slightly effects the gas separation performance. When compared to imidazolium-based ILs, phosphonium-based ILs are less effective for gas separation applications although they can be considered for gas storage purposes. However, the gas selectivities of some of the phosphonium-based IL/MOF composites are still higher than those of other materials reported in the literature. For example, while CO_2/CH_4 selectivity of $[P_{(14)666}][DCA]$/CuBTC is 5.02 at 1 bar, it is around 4.43 for MOF-177.[168] Similarly,

CO_2/N_2 selectivities of $[P_{(14)666}][Br]$/ZIF-8 (7.18) and $[P_{(14)666}][DCA]$/CuBTC (16.7) are higher compared to that of mesoporous carbon (2.9) reported in the literature.[184] The most remarkable difference between phosphonium-based IL/MOF composites and the materials reported in the literature is obtained in CH_4/N_2 selectivities. MOF-5 (1.13)[168] and Zeolite 5A (0.94)[168] have lower CH_4/N_2 selectivities compared to $[P_{4444}][TOS]$/ZIF-8 and $[P_{(14)666}][DCA]$/CuBTC, which have CH_4/N_2 selectivities of 2.77 and 3.3, respectively.

Chapter 6: Conclusions and Outlook

In this study, computational and experimental analyses have been conducted to investigate the gas adsorption and separation performances of imidazolium and phosphonium-based IL-incorporated MOF composites. In the first part, experiments were combined with atomically-detailed simulations and DFT calculations to investigate the improvement of gas separation properties of ZIF-8 upon incorporation of an imidazolium-based IL, [BMIM][PF_6]. Detailed characterization based on XRD, BET, TGA and FTIR complemented with DFT calculations illustrated strong interactions between IL and MOF. These interactions lead to generation of new adsorption sites with different gas affinities compared to their counterparts in pristine MOF. Adsorption isotherms for CO_2, CH_4, and N_2 gases for ZIF-8 and [BMIM][PF_6]/ZIF-8 were experimentally measured and GCMC simulations were performed to predict these results. Both CO_2/CH_4 and CO_2/N_2 selectivities of ZIF-8 were more than doubled at low pressures. For instance, at 0.1 bar, ideal and mixture selectivities of ZIF-8 for CO_2/N_2 selectivity increased from 7.82 and 7.85 to 24.21 and 28.02, respectively, upon [BMIM][PF_6] incorporation. This improvement in gas selectivities was evaluated based on the isosteric heats of adsorption values provided from the GCMC simulations. The increase in selectivities at low pressures was explained by an increase in the difference of isosteric heat of adsorption of individual gases. These results illustrate that [BMIM][PF_6]/ZIF-8 is a promising material for gas separation applications, especially for CO_2 separation processes, such as natural gas sweetening and removal of CO_2 from power plant flue gas. Here, it is important to note that adsorption properties of IL/MOF composites were solely focused on to support the separation improvement. In addition to improvements in adsorption-based separation performance of ZIF-8, its kinetic-based separation performance may improve because of the creation of new sorption sites by IL.

In the second part, the effect of phosphonium-based IL impregnation on the gas adsorption and separation performances of different MOFs was investigated. Five different phosphonium-based ILs ([P_{4444}][TOS], [P_{4441}][$MeSO_4$], [$P_{(14)666}$][TMPP], [$P_{(14)666}$][Br], and [$P_{(14)666}$][DCA]) were incorporated into ZIF-8 and [$P_{(14)666}$][DCA] was incorporated into CuBTC for the first time in the literature. It was aimed to extend the understanding about IL/MOF composites and the effect of a different IL family on gas uptakes and selectivities. Characterization studies were complemented with adsorption measurements of CO_2, CH_4, and N_2 gases in ZIF-8, CuBTC, and phosphonium-based IL/MOF samples which were obtained using volumetric methods. Single adsorption isotherms were fitted using dual site Langmuir and Freundlich model and selectivity for CO_2/CH_4, CO_2/N_2, and CH_4/N_2 gas pairs were calculated. While phosphonium-based IL impregnation may increase the gas adsorption capacity of pristine MOF, it has very slight effect on improving the gas separation performances of MOFs.

As a conclusion, IL/MOF composites are considered as promising adsorbent materials for gas storage and separation applications. It is important to note that there are thousands of MOFs and hundreds of ILs available with a range of physicochemical properties and gas affinities. Thus, it is possible to design new IL/MOF materials which can outstandingly perform as an energy efficient and low cost material for gas storage and separation processes. These findings will trigger extensive research in the way of developing new IL/MOF materials with exceptional performance in a variety of applications. To create promising IL/MOF adsorbent materials for gas adsorption and separation applications, there are many things to do as the future work which are briefly addressed below:

Large scale screening of ILs and MOFs: There are limitless number of ILs and MOFs in the literature offering several opportunities for gas adsorption and separation applications. However, experimental methods may be insufficient for performance measurements of each material and identifying the most promising ones because of time restrictions. It is possible to screen large numbers of materials using computational methods and create a database. Up to date, most of the computational studies have

focused on only one MOF and a few ILs at a time. Computational studies can be used to identify the most promising IL/MOF pairs for desired gas adsorption/separation applications by saving the experimental effort, time, and resources. By using the information obtained from the simulations, the best performing IL/MOF composites can be prepared in laboratory scale and gas adsorption measurements can be performed experimentally.

Investigation of the regenerability of IL/MOF composites: In an adsorption process, working capacity is highly important to evaluate the performance of an adsorbent material. Working capacity can be defined as the difference between the amount of gas adsorbed at the adsorption pressure and the amount of adsorbed gas at desorption/evacuation pressure.[185] When the working capacity of an adsorbent for a specific gas is higher, the gas can be recovered effectively and the adsorbent can be used for another adsorption measurement. Moreover, a smaller adsorber volume is required for the desired gas adsorption/separation application.[185] Up to date, none of the studies in the literature have focused on investigation of working capacities of IL/MOF composites and the reusability of these materials. This issue is highly important especially for the applicability of IL/MOF composites in real processes, therefore future work can be focused on this topic.

Testing IL/MOF composites for mixed gas separations: In almost all experimental studies related with gas storage and separation, single-component gas adsorption measurements of IL/MOF composites were carried out rather than mixtures. Therefore, these studies reported ideal selectivities instead of mixture selectivities. However, gases are in the mixture form in real applications and purification of these mixtures is crucial regarding process efficiency and environmental issues. For example, although experimental studies which were discussed in Chapter 2 reported ideal selectivities of CO_2, CO_2 practically exists together with various gases (e.g. CH_4, N_2, and CO etc.) and impurities (e.g. SO_x, NO_x, and water).[6] It is required to test IL/MOF composites with gas mixtures to understand how these materials actually behave as well as to validate the single-component gas adsorption approach which have been used widely. More research

in this field will be useful to see the real potential of these adsorbents in industrial gas separation processes.

Existing experimental studies used IL/MOF adsorbents at the lab-scale and computational studies examined the performance of composites at the molecular level. It would be very valuable to simulate the whole adsorption process at the large-scale and optimize the process. In other words, studies that employ multi-scale modeling approaches from micro (molecular) scale to macro (industrial) scale will be very useful for the design and development of IL/MOF composites for industrial adsorption processes.

Preparing IL/MOF composites using MOFs including defects: Recent studies showed that it is possible to create defect sites on MOFs during the synthesis or by post-synthetic treatment.[186] The density of CUSs in MOFs in addition to porosity and surface areas of MOFs can be changed by defect engineering.[186] For example, Wu et al.[187] reported that missing-linker defects in UiO-66 leaded to increases in the pore volume and BET surface area by 150% and 60%, respectively compared to defect-free UiO-66 crystal. These defects also increased CO_2 and CH_4 uptake especially at high pressures. Therefore, different types of MOFs can be modified in order to create defects in the structure before IL incorporation as a future study. By this way, it may be possible to incorporate more IL molecules in the structure and tune the cavities to enhance the gas uptake and selectivity of IL/MOF composites.

Applicability of IL/MOF composites in real processes: Industrial conditions are generally different than the lab-scale measurement conditions, which may be a challenge in the application of IL/MOF composites. For example, an IL/MOF composite can give high selectivity for a specific gas separation, however the presence of water may affect the performance due to the moisture sensitivity of the MOF. CuBTC is a well-known MOF which has been widely examined in gas separation studies and it was reported that water at a certain weight fraction may lead to the collapse of the framework. Therefore, IL/CuBTC material may not be applicable for the separation of gas mixtures which has water content (e.g. natural gas). The pH and impurities have also important effects on the

performance of IL/MOF composites. In future studies, these effects should be investigated to understand the optimum conditions for the industrial applications of the composites.

BIBLIOGRAPHY

1. Rackley, S., *Carbon Capture and Storage*. Gulf Professional Publishing: 2009.
2. Kampa, M.; Castanas, E., Human Health Effects of Air Pollution. *Environmental Pollution* **2008,** *151* (2), 362-367.
3. Bae, Y. S.; Snurr, R. Q., Development and Evaluation of Porous Materials for Carbon Dioxide Separation and Capture. *Angewandte Chemie International Edition* **2011,** *50* (49), 11586-11596.
4. Li, J.-R.; Kuppler, R. J.; Zhou, H.-C., Selective Gas Adsorption and Separation in Metal-Organic Frameworks. *Chemical Society Reviews* **2009,** *38* (5), 1477-1504.
5. Li, J.-R.; Sculley, J.; Zhou, H.-C., Metal-Organic Frameworks for Separations. *Chemical Reviews* **2011,** *112* (2), 869-932.
6. Adatoz, E.; Avci, A. K.; Keskin, S., Opportunities and Challenges of MOF-Based Membranes in Gas Separations. *Separation and Purification Technology* **2015,** *152*, 207-237.
7. Chen, B.; Liang, C.; Yang, J.; Contreras, D. S.; Clancy, Y. L.; Lobkovsky, E. B.; Yaghi, O. M.; Dai, S., A Microporous Metal-Organic Framework for Gas-Chromatographic Separation of Alkanes. *Angewandte Chemie* **2006,** *118* (9), 1418-1421.
8. Rosi, N. L.; Eckert, J.; Eddaoudi, M.; Vodak, D. T.; Kim, J.; O'Keeffe, M.; Yaghi, O. M., Hydrogen Storage in Microporous Metal-Organic Frameworks. *Science* **2003,** *300* (5622), 1127-1129.
9. Sumida, K.; Rogow, D. L.; Mason, J. A.; McDonald, T. M.; Bloch, E. D.; Herm, Z. R.; Bae, T.-H.; Long, J. R., Carbon Dioxide Capture in Metal-Organic Frameworks. *Chemical Reviews* **2011,** *112* (2), 724-781.
10. Ma, L.; Abney, C.; Lin, W., Enantioselective Catalysis with Homochiral Metal-Organic Frameworks. *Chemical Society Reviews* **2009,** *38* (5), 1248-1256.
11. Yoon, M.; Srirambalaji, R.; Kim, K., Homochiral Metal-Organic Frameworks for Asymmetric Heterogeneous Catalysis. *Chemical Reviews* **2011,** *112* (2), 1196-1231.
12. Allendorf, M. D.; Houk, R. J.; Andruszkiewicz, L.; Talin, A. A.; Pikarsky, J.; Choudhury, A.; Gall, K. A.; Hesketh, P. J., Stress-Induced Chemical Detection Using Flexible Metal-Organic Frameworks. *Journal of the American Chemical Society* **2008,** *130* (44), 14404-14405.
13. Lan, A.; Li, K.; Wu, H.; Olson, D. H.; Emge, T. J.; Ki, W.; Hong, M.; Li, J., A Luminescent Microporous Metal-Organic Framework for the Fast and Reversible Detection of High Explosives. *Angewandte Chemie International Edition* **2009,** *48* (13), 2334-2338.
14. Kreno, L. E.; Leong, K.; Farha, O. K.; Allendorf, M.; Van Duyne, R. P.; Hupp, J. T., Metal-Organic Framework Materials as Chemical Sensors. *Chemical Reviews* **2011,** *112* (2), 1105-1125.
15. Horcajada, P.; Chalati, T.; Serre, C.; Gillet, B.; Sebrie, C.; Baati, T.; Eubank, J. F.; Heurtaux, D.; Clayette, P.; Kreuz, C., Porous Metal-Organic-Framework Nanoscale Carriers as a Potential Platform for Drug Delivery and Imaging. *Nature Materials* **2010,** *9* (2), 172-178.

16. Givaja, G.; Amo-Ochoa, P.; Gómez-García, C. J.; Zamora, F., Electrical Conductive Coordination Polymers. *Chemical Society Reviews* **2012,** *41* (1), 115-147.
17. Narayan, T. C.; Miyakai, T.; Seki, S.; Dincă, M., High Charge Mobility in a Tetrathiafulvalene-Based Microporous Metal-Organic Framework. *Journal of the American Chemical Society* **2012,** *134* (31), 12932-12935.
18. Della Rocca, J.; Liu, D.; Lin, W., Nanoscale Metal-Organic Frameworks for Biomedical Imaging and Drug Delivery. *Accounts of Chemical Research* **2011,** *44* (10), 957-968.
19. Liu, J.; Thallapally, P. K.; McGrail, B. P.; Brown, D. R.; Liu, J., Progress in Adsorption-Based CO_2 Capture by Metal-Organic Frameworks. *Chemical Society Reviews* **2012,** *41* (6), 2308-2322.
20. Keskin, S.; van Heest, T. M.; Sholl, D. S., Can Metal-Organic Framework Materials Play a Useful Role in Large-Scale Carbon Dioxide Separations? *ChemSusChem* **2010,** *3* (8), 879-891.
21. An, J.; Rosi, N. L., Tuning MOF CO_2 Adsorption Properties via Cation Exchange. *Journal of the American Chemical Society* **2010,** *132* (16), 5578-5579.
22. Ban, Y.; Li, Y.; Peng, Y.; Jin, H.; Jiao, W.; Liu, X.; Yang, W., Metal-Substituted Zeolitic Imidazolate Framework ZIF-108: Gas-Sorption and Membrane-Separation Properties. *Chemistry - A European Journal* **2014,** *20* (36), 11402-11409.
23. Karagiaridi, O.; Lalonde, M. B.; Bury, W.; Sarjeant, A. A.; Farha, O. K.; Hupp, J. T., Opening ZIF-8: A Catalytically Active Zeolitic Imidazolate Framework of Sodalite Topology with Unsubstituted Linkers. *Journal of the American Chemical Society* **2012,** *134* (45), 18790-18796.
24. Thompson, J. A.; Brunelli, N. A.; Lively, R. P.; Johnson, J.; Jones, C. W.; Nair, S., Tunable CO_2 Adsorbents by Mixed-Linker Synthesis and Postsynthetic Modification of Zeolitic Imidazolate Frameworks. *The Journal of Physical Chemistry C* **2013,** *117* (16), 8198-8207.
25. Thompson, J. A.; Vaughn, J. T.; Brunelli, N. A.; Koros, W. J.; Jones, C. W.; Nair, S., Mixed-Linker Zeolitic Imidazolate Framework Mixed-Matrix Membranes for Aggressive CO_2 Separation from Natural Gas. *Microporous and Mesoporous Materials* **2014,** *192*, 43-51.
26. Wang, Z.; Cohen, S. M., Postsynthetic Modification of Metal-Organic Frameworks. *Chemical Society Reviews* **2009,** *38* (5), 1315-1329.
27. Zhu, Q.-L.; Xu, Q., Metal-Organic Framework Composites. *Chemical Society Reviews* **2014,** *43* (16), 5468-5512.
28. Uzun, A.; Keskin, S., Site Characteristics in Metal Organic Frameworks for Gas Adsorption. *Progress in Surface Science* **2014,** *89* (1), 56-79.
29. Cohen, S. M., Postsynthetic Methods for the Functionalization of Metal–Organic Frameworks. *Chemical Reviews* **2011,** *112* (2), 970-1000.
30. Bae, Y.-S.; Farha, O. K.; Hupp, J. T.; Snurr, R. Q., Enhancement of CO_2/N_2 Selectivity in a Metal-Organic Framework by Cavity Modification. *Journal of Materials Chemistry* **2009,** *19* (15), 2131-2134.

31. Gutowski, K. E.; Holbrey, J. D.; Rogers, R. D.; Dixon, D. A., Prediction of The Formation and Stabilities of Energetic Salts and Ionic Liquids Based on Ab Initio Electronic Structure Calculations. *The Journal of Physical Chemistry B* **2005,** *109* (49), 23196-23208.
32. Welton, T., Room-Temperature Ionic Liquids. Solvents for Synthesis and Catalysis. *Chemical Reviews* **1999,** *99* (8), 2071-2083.
33. Fatemi, S. M.; Foroutan, M., Recent Findings About Ionic Liquids Mixtures Obtained by Molecular Dynamics Simulation. *Journal of Nanostructure in Chemistry* **2015,** *5* (3), 243-253.
34. Wasserscheid, P.; Keim, W., Ionic Liquids—New "Solutions" for Transition Metal Catalysis. *Angewandte Chemie International Edition* **2000,** *39* (21), 3772-3789.
35. Ban, Y.; Li, Z.; Li, Y.; Peng, Y.; Jin, H.; Jiao, W.; Guo, A.; Wang, P.; Yang, Q.; Zhong, C., Confinement of Ionic Liquids in Nanocages: Tailoring the Molecular Sieving Properties of ZIF-8 for Membrane-Based CO_2 Capture. *Angewandte Chemie* **2015,** *127* (51), 15703-15707.
36. Zhu, M.; Venna, S. R.; Jasinski, J. B.; Carreon, M. A., Room-Temperature Synthesis of ZIF-8: The Coexistence of ZnO Nanoneedles. *Chemistry of Materials* **2011,** *23* (16), 3590-3592.
37. Venna, S. R.; Carreon, M. A., Highly Permeable Zeolite Imidazolate Framework-8 Membranes for CO_2/CH_4 Separation. *Journal of the American Chemical Society* **2009,** *132* (1), 76-78.
38. Huddleston, J. G.; Visser, A. E.; Reichert, W. M.; Willauer, H. D.; Broker, G. A.; Rogers, R. D., Characterization and Comparison of Hydrophilic and Hydrophobic Room Temperature Ionic Liquids Incorporating the Imidazolium Cation. *Green Chemistry* **2001,** *3* (4), 156-164.
39. Chen, Y.; Hu, Z.; Gupta, K. M.; Jiang, J., Ionic Liquid/Metal-Organic Framework Composite for CO_2 Capture: a Computational Investigation. *The Journal of Physical Chemistry C* **2011,** *115* (44), 21736-21742.
40. Kumelan, J.; Kamps, Á. P.-S.; Tuma, D.; Maurer, G., Solubility of CO_2 in the Ionic Liquids [BMIM][CH_3SO_4] and [BMIM][PF_6]. *Journal of Chemical Engineering Data* **2006,** *51* (5), 1802-1807.
41. Krungleviciute, V.; Lask, K.; Migone, A.; Lee, J. Y.; Li, J., Kinetics and Equilibrium of Gas Adsorption on RPM1-Co and Cu-BTC Metal-Organic Frameworks: Potential for Gas Separation Applications. *AIChE Journal* **2008,** *54* (4), 918-923.
42. Kinik, P.; Uzun, A.; Keskin, S., Ionic Liquid/Metal Organic Framework Composites: From Synthesis to Applications. *ChemSusChem*.
43. Kinik, F. P.; Altintas, C.; Balci, V.; Koyuturk, B.; Uzun, A.; Keskin, S., [BMIM][PF_6] Incorporation Doubles CO_2 Selectivity of ZIF-8: Elucidation of Interactions and Their Consequences on Performance. *ACS Applied Materials and Interfaces* **2016**.
44. Makal, T. A.; Li, J.-R.; Lu, W.; Zhou, H.-C., Methane Storage in Advanced Porous Materials. *Chemical Society Reviews* **2012,** *41* (23), 7761-7779.
45. Morris, R. E.; Wheatley, P. S., Gas Storage in Nanoporous Materials. *Angewandte Chemie International Edition* **2008,** *47* (27), 4966-4981.

46. Qiu, S. L.; Xue, M.; Zhu, G. S., Metal-Organic Framework Membranes: From Synthesis to Separation Application. *Chemical Society Reviews* **2014,** *43* (16), 6116-6140.
47. Meek, S. T.; Greathouse, J. A.; Allendorf, M. D., Metal-Organic frameworks: A Rapidly Growing Class of Versatile Nanoporous Materials. *Advanced Materials* **2011,** *23* (2), 249-267.
48. Furukawa, H.; Cordova, K. E.; O'Keeffe, M.; Yaghi, O. M., The Chemistry and Applications of Metal-Organic Frameworks. *Science* **2013,** *341* (6149), 1230444.
49. Feng, X.; Ding, X.; Jiang, D., Covalent Organic Frameworks. *Chemical Society Reviews* **2012,** *41* (18), 6010-6022.
50. Keskin, S.; Kızılel, S., Biomedical Applications of Metal Organic Frameworks. *Industrial & Engineering Chemistry Research* **2011,** *50* (4), 1799-1812.
51. Liu, Y.; Liu, D.; Yang, Q.; Zhong, C.; Mi, J., Comparative Study of Separation Performance of COFs and MOFs for $CH_4/CO_2/H_2$ Mixtures. *Industrial & Engineering Chemistry Research* **2010,** *49* (6), 2902-2906.
52. Sun, P.; Armstrong, D. W., Ionic Liquids in Analytical Chemistry. *Analytica Chimica Acta* **2010,** *661* (1), 1-16.
53. Vidal, L.; Riekkola, M.-L.; Canals, A., Ionic Liquid-Modified Materials for Solid-Phase Extraction and Separation: A Review. *Analytica Chimica Acta* **2012,** *715*, 19-41.
54. Plechkova, N. V.; Seddon, K. R., Applications of Ionic Liquids in the Chemical Industry. *Chemical Society Reviews* **2008,** *37* (1), 123-150.
55. Kulkarni, P. S.; Branco, L. C.; Crespo, J. G.; Nunes, M. C.; Raymundo, A.; Afonso, C. A., Comparison of Physicochemical Properties of New Ionic Liquids Based on Imidazolium, Quaternary Ammonium, and Guanidinium Cations. *Chemistry–A European Journal* **2007,** *13* (30), 8478-8488.
56. Rogers, R. D.; Seddon, K. R., Ionic Liquids - Solvents of the Future ? *Science* **2003,** *302* (5646), 792-793.
57. Wishart, J. F., Energy Applications of Ionic Liquids. *Energy & Environmental Science* **2009,** *2* (9), 956-961.
58. Marsh, K.; Boxall, J.; Lichtenthaler, R., Room Temperature Ionic Liquids and Their Mixtures - A Review. *Fluid Phase Equilibria* **2004,** *219* (1), 93-98.
59. MacFarlane, D. R.; Tachikawa, N.; Forsyth, M.; Pringle, J. M.; Howlett, P. C.; Elliott, G. D.; Davis, J. H.; Watanabe, M.; Simon, P.; Angell, C. A., Energy Applications of Ionic Liquids. *Energy & Environmental Science* **2014,** *7* (1), 232-250.
60. Zhang, S.; Zhang, J.; Zhang, Y.; Deng, Y., Nanoconfined Ionic Liquids. *Chemical Reviews* **2016**.
61. Yaghi, O. M.; O'keeffe, M.; Ockwig, N. W.; Chae, H. K.; Eddaoudi, M.; Kim, J., Reticular Synthesis and the Design of New Materials. *Nature* **2003,** *423* (6941), 705-714.
62. First, E. L.; Floudas, C. A., MOFomics: Computational Pore Characterization of Metal–Organic Frameworks. *Microporous and Mesoporous Materials* **2013,** *165*, 32-39.
63. Eddaoudi, M.; Kim, J.; Rosi, N.; Vodak, D.; Wachter, J.; O'keeffe, M.; Yaghi, O. M., Systematic Design of Pore Size and Functionality in Isoreticular MOFs and Their Application in Methane Storage. *Science* **2002,** *295* (5554), 469-472.

64. Frost, H.; Snurr, R. Q., Design Requirements for Metal-Organic Frameworks as Hydrogen Storage Materials. *The Journal of Physical Chemistry C* **2007,** *111* (50), 18794-18803.
65. Düren, T.; Millange, F.; Férey, G.; Walton, K. S.; Snurr, R. Q., Calculating Geometric Surface Areas as a Characterization Tool for Metal−Organic Frameworks. *The Journal of Physical Chemistry C* **2007,** *111* (42), 15350-15356.
66. Sels, B.; Kustov, L., *Zeolites and Zeolite-Like Materials*. Elsevier: 2016.
67. Alshammari, A.; Jiang, Z.; Cordova, K. E., Metal Organic Frameworks as Emerging Photocatalysts. In *Semiconductor Photocatalysis-Materials, Mechanisms and Applications*, InTech: 2016.
68. Park, K. S.; Ni, Z.; Côté, A. P.; Choi, J. Y.; Huang, R.; Uribe-Romo, F. J.; Chae, H. K.; O'Keeffe, M.; Yaghi, O. M., Exceptional Chemical and Thermal Stability of Zeolitic Imidazolate Frameworks. *Proceedings of the National Academy of Sciences* **2006,** *103* (27), 10186-10191.
69. Jiang, D.; Keenan, L. L.; Burrows, A. D.; Edler, K. J., Synthesis and Post-Synthetic Modification of MIL-101(Cr)-NH_2 via A Tandem Diazotisation Process. *Chemical Communications* **2012,** *48* (99), 12053-12055.
70. Hassan, H. M.; Betiha, M. A.; Mohamed, S. K.; El-Sharkawy, E.; Ahmed, E. A., Salen-Zr (IV) Complex Grafted Into Amine-Tagged MIL-101(Cr) As a Robust Multifunctional Catalyst for Biodiesel Production and Organic Transformation Reactions. *Applied Surface Science* **2017,** *412*, 394-404.
71. Khutia, A.; Janiak, C., Programming MIL-101(Cr) for Selective and Enhanced CO_2 Adsorption at Low Pressure by Postsynthetic Amine Functionalization. *Dalton Transactions* **2014,** *43* (3), 1338-1347.
72. Zhao, T.; Jeremias, F.; Boldog, I.; Nguyen, B.; Henninger, S. K.; Janiak, C., High-Yield, Fluoride-Free and Large-Scale Synthesis of MIL-101(Cr). *Dalton Transactions* **2015,** *44* (38), 16791-16801.
73. Chavan, S.; Vitillo, J. G.; Gianolio, D.; Zavorotynska, O.; Civalleri, B.; Jakobsen, S.; Nilsen, M. H.; Valenzano, L.; Lamberti, C.; Lillerud, K. P., H_2 Storage in Isostructural UiO-67 and UiO-66 MOFs. *Physical Chemistry Chemical Physics* **2012,** *14* (5), 1614-1626.
74. Yang, D.-A.; Cho, H.-Y.; Kim, J.; Yang, S.-T.; Ahn, W.-S., CO_2 Capture and Conversion Using Mg-MOF-74 Prepared by a Sonochemical Method. *Energy & Environmental Science* **2012,** *5* (4), 6465-6473.
75. Japip, S.; Wang, H.; Xiao, Y.; Chung, T. S., Highly Permeable Zeolitic Imidazolate Framework (ZIF)-71 Nano-Particles Enhanced Polyimide Membranes for Gas Separation. *Journal of Membrane Science* **2014,** *467*, 162-174.
76. Nalaparaju, A.; Zhao, X.; Jiang, J., Molecular Understanding for the Adsorption of Water and Alcohols in Hydrophilic and Hydrophobic Zeolitic Metal- Organic Frameworks. *The Journal of Physical Chemistry C* **2010,** *114* (26), 11542-11550.
77. Chen, C.; Kim, J.; Yang, D.-A.; Ahn, W.-S., Carbon Dioxide Adsorption over Zeolite-Like Metal Organic Frameworks (ZMOFs) Having a SOD Topology: Structure and Ion-Exchange Effect. *Chemical Engineering Journal* **2011,** *168* (3), 1134-1139.

78. Gupta, K. M.; Chen, Y.; Jiang, J., Ionic Liquid Membranes Supported by Hydrophobic and Hydrophilic Metal–Organic Frameworks for CO_2 Capture. **2013**.
79. Huo, S.-H.; Yan, X.-P., Metal-Organic Framework MIL-100(Fe) for the Adsorption of Malachite Green from Aqueous Solution. *Journal of Materials Chemistry* **2012,** *22* (15), 7449-7455.
80. Dhakshinamoorthy, A.; Alvaro, M.; Garcia, H., Commercial Metal-Organic Frameworks as Heterogeneous Catalysts. *Chemical Communications* **2012,** *48* (92), 11275-11288.
81. Jin, H.; Li, Y.; Liu, X.; Ban, Y.; Peng, Y.; Jiao, W.; Yang, W., Recovery of HMF from Aqueous Solution by Zeolitic Imidazolate Frameworks. *Chemical Engineering Science* **2015,** *124*, 170-178.
82. Zhang, Y.-B.; Su, J.; Furukawa, H.; Yun, Y.; Gándara, F.; Duong, A.; Zou, X.; Yaghi, O. M., Single-Crystal Structure of a Covalent Organic Framework. *Journal of the American Chemical Society* **2013,** *135* (44), 16336-16339.
83. Yaghi, O. M.; Goddard III, W. A., A Joint Theory and Experimental Project in the Synthesis and Testing of Porous COFs for On-Board Vehicular Hydrogen Storage. **2012**.
84. Morris, R. E., Ionothermal Synthesis-Ionic Liquids as Functional Solvents in the Preparation of Crystalline Materials. *Chemical Communications* **2009,** (21), 2990-2998.
85. Xu, L.; Liu, B.; Liu, S.-X.; Jiao, H.; de Castro, B.; Cunha-Silva, L., The Influence of 1-Alkyl-3-Methyl Imidazolium Ionic Liquids on a Series of Cobalt-1,4-Benzenedicarboxylate Metal-Organic Frameworks. *CrystEngComm* **2014,** *16* (46), 10649-10657.
86. Jin, K.; Huang, X.; Pang, L.; Li, J.; Appel, A.; Wherland, S., [Cu(I)(bpp)]BF_4: The First Extended Coordination Network Prepared Solvothermally in an Ionic Liquid Solvent. *Chemical Communications* **2002,** (23), 2872-2873.
87. Dybtsev, D. N.; Chun, H.; Kim, K., Three-Dimensional Metal-Organic Framework with (3,4)-Connected Net, Synthesized from an Ionic Liquid Medium. *Chemical Communications* **2004,** (14), 1594-1595.
88. Parnham, E. R.; Morris, R. E., Ionothermal Synthesis of Zeolites, Metal-Organic Frameworks, and Inorganic-Organic Hybrids. *Accounts of Chemical Research* **2007,** *40* (10), 1005-1013.
89. Freudenmann, D.; Wolf, S.; Wolff, M.; Feldmann, C., Ionic Liquids: New Perspectives for Inorganic Synthesis ? *Angewandte Chemie International Edition* **2011,** *50* (47), 11050-11060.
90. Fujie, K.; Kitagawa, H., Ionic Liquid Transported into Metal-Organic Frameworks. *Coordination Chemistry Reviews* **2016,** *307*, 382-390.
91. Khan, N. A.; Hasan, Z.; Jhung, S. H., Ionic Liquids Supported on Metal-Organic Frameworks: Remarkable Adsorbents for Adsorptive Desulfurization. *Chemistry - A European Journal* **2014,** *20* (2), 376-380.
92. Luo, Q.-X.; Song, X.-D.; Ji, M.; Park, S.-E.; Hao, C.; Li, Y.-Q., Molecular Size-and Shape-Selective Knoevenagel Condensation over Microporous $Cu_3(BTC)_2$ Immobilized Amino-Functionalized Basic Ionic Liquid Catalyst. *Applied Catalysis A* **2014,** *478*, 81-90.

93. Sezginel, K. B.; Keskin, S.; Uzun, A., Tuning the Gas Separation Performance of CuBTC by Ionic Liquid Incorporation. *Langmuir* **2016,** *32* (4), 1139-1147.
94. Luo, Q.-X.; An, B.-W.; Ji, M.; Park, S.-E.; Hao, C.; Li, Y.-Q., Metal-Organic Frameworks HKUST-1 as Porous Matrix for Encapsulation of Basic Ionic Liquid Catalyst: Effect of Chemical Behaviour of Ionic Liquid in Solvent. *Journal of Porous Materials* **2015,** *22* (1), 247-259.
95. Chen, C.; Wu, Z.; Que, Y.; Li, B.; Guo, Q.; Li, Z.; Wang, L.; Wan, H.; Guan, G., Immobilization of a Thiol-Functionalized Ionic Liquid onto HKUST-1 Through Thiol Compounds as the Chemical Bridge. *RSC Advances* **2016,** *6* (59), 54119-54128.
96. Ma, J.; Ying, Y.; Guo, X.; Huang, H.; Liu, D.; Zhong, C., Fabrication of Mixed-Matrix Membrane Containing Metal-Organic Framework Composite with Task-Specific Ionic Liquid for Efficient CO_2 Separation. *Journal of Materials Chemistry A* **2016,** *4* (19), 7281-7288.
97. Da Silva, F.; Magalhães, G.; Jardim, E.; Silvestre-Albero, J.; Sepúlveda-Escribano, A.; de Azevedo, D.; de Lucena, S., CO_2 Adsorption on Ionic Liquid-Modified Cu-BTC: Experimental and Simulation Study. *Adsorption Science and Technology* **2015,** *33* (2), 223-242.
98. Wan, H.; Chen, C.; Wu, Z.; Que, Y.; Feng, Y.; Wang, W.; Wang, L.; Guan, G.; Liu, X., Encapsulation of Heteropolyanion-Based Ionic Liquid within the Metal-Organic Framework MIL-100(Fe) for Biodiesel Production. *ChemCatChem* **2015,** *7* (3), 441-449.
99. Han, M.; Gu, Z.; Chen, C.; Wu, Z.; Que, Y.; Wang, Q.; Wan, H.; Guan, G., Efficient Confinement of Ionic Liquids in MIL-100(Fe) Frameworks by the "Impregnation-Reaction-Encapsulation" Strategy for Biodiesel Production. *RSC Advances* **2016,** *6* (43), 37110-37117.
100. Nasrollahpour, A.; Moradi, S.; Baniamerian, M., Vortex-Assisted Dispersive Solid-Phase Microextraction Using Ionic Liquid-Modified Metal-Organic Frameworks of PAHs from Environmental Water, Vegetable, and Fruit Juice Samples. *Food Analysis Methods* **2017**, 1-12.
101. Koyuturk, B.; Altintas, C.; Kinik, F. P.; Keskin, S.; Uzun, A., Improving Gas Separation Performance of ZIF-8 by [BMIM][BF_4] Incorporation: Interactions and Their Consequences on Performance. *The Journal of Physical Chemistry C* **2017**.
102. Abednatanzi, S.; Leus, K.; Derakhshandeh, P. G.; Nahra, F.; De Keukeleere, K.; Van Hecke, K.; Van Driessche, I.; Abbasi, A.; Nolan, S. P.; Van Der Voort, P., POM@IL-MOFs-Inclusion of POMs in Ionic Liquid Modified MOFs to Produce Recyclable Oxidation Catalysts. *Catalysis Science & Technology* **2017**.
103. Hassan, H. M.; Betiha, M. A.; Mohamed, S. K.; El-Sharkawy, E.; Ahmed, E. A., Stable and Recyclable MIL-101(Cr)-Ionic Liquid Based Hybrid Nanomaterials as Heterogeneous Catalyst. *Journal of Molecular Liquids* **2017**.
104. Li, H.; Tuo, L.; Yang, K.; Jeong, H.-K.; Dai, Y.; He, G.; Zhao, W., Simultaneous Enhancement of Mechanical Properties and CO_2 Selectivity of ZIF-8 Mixed Matrix Membranes: Interfacial Toughening Effect of Ionic Liquid. *Journal of Membrane Science* **2016,** *511*, 130-142.
105. Wu, J.; Gao, Y.; Zhang, W.; Tan, Y.; Tang, A.; Men, Y.; Tang, B., Deep Desulfurization by Oxidation Using an Active Ionic Liquid-Supported Zr Metal-Organic Framework as Catalyst. *Applied Organometallic Chemistry* **2015,** *29* (2), 96-100.

106. Fujie, K.; Yamada, T.; Ikeda, R.; Kitagawa, H., Introduction of an Ionic Liquid into the Micropores of a Metal-Organic Framework and Its Anomalous Phase Behavior. *Angewandte Chemie International Edition* **2014,** *53* (42), 11302-11305.
107. Fujie, K.; Ikeda, R.; Otsubo, K.; Yamada, T.; Kitagawa, H., Lithium Ion Diffusion in a Metal-Organic Framework Mediated by an Ionic Liquid. *Chemistry of Materials* **2015,** *27* (21), 7355-7361.
108. Dhumal, N. R.; Singh, M. P.; Anderson, J. A.; Kiefer, J.; Kim, H. J., Molecular Interactions of a Cu-Based Metal-Organic Framework with a Confined Imidazolium-Based Ionic Liquid: A Combined Density Functional Theory and Experimental Vibrational Spectroscopy Study. *The Journal of Physical Chemistry C* **2016,** *120* (6), 3295-3304.
109. Sun, X. L.; Deng, W. H.; Chen, H.; Han, H. L.; Taylor, J. M.; Wan, C. Q.; Xu, G., A Metal-Organic Framework Impregnated with a Binary Ionic Liquid for Safe Proton Conduction Above 100 °C. *Chemistry - A European Journal* **2016**.
110. Xin, Y.; Wang, C.; Wang, Y.; Sun, J.; Gao, Y., Encapsulation of an Ionic Liquid into the Nanopores of a 3D Covalent Organic Framework. *RSC Advances* **2017,** *7* (3), 1697-1700.
111. Ahmed, I.; Panja, T.; Khan, N. A.; Sarker, M.; Yu, J.-S.; Jhung, S. H., Nitrogen-Doped Porous Carbons from Ionic Liquids@MOF: Remarkable Adsorbents for Both Aqueous and Nonaqueous Media. *ACS Applied Materials and Interfaces* **2017**.
112. Khan, N. A.; Hasan, Z.; Jhung, S. H., Ionic Liquid@MIL-101 Prepared via the Ship-in-Bottle Technique: Remarkable Adsorbents for the Removal of Benzothiophene from Liquid Fuel. *Chemical Communications* **2016,** *52* (12), 2561-2564.
113. Luo, Q.-X.; Ji, M.; Lu, M.-h.; Hao, C.; Qiu, J.-S.; Li, Y.-Q., Organic Electron-Rich N-Heterocyclic Compound as a Chemical Bridge: Building a Brönsted Acidic Ionic Liquid Confined in MIL-101 Nanocages. *Journal of Materials Chemistry A* **2013,** *1* (22), 6530-6534.
114. Li, Z.; Wang, W.; Chen, Y.; Xiong, C.; He, G.; Cao, Y.; Wu, H.; Guiver, M. D.; Jiang, Z., Constructing Efficient Ion Nanochannels in Alkaline Anion Exchange Membranes by the In Situ Assembly of a Poly(Ionic Liquid) in Metal-Organic Frameworks. *Journal of Materials Chemistry A* **2016,** *4* (6), 2340-2348.
115. Abroshan, H.; Kim, H. J., On the Structural Stability of Ionic Liquid-IRMOF Composites: A Computational Study. *Physical Chemistry Chemical Physics* **2015,** *17* (9), 6248-6254.
116. Gupta, K. M.; Chen, Y.; Hu, Z.; Jiang, J., Metal-Organic Framework Supported Ionic Liquid Membranes for CO_2 Capture: Anion Effects. *Physical Chemistry Chemical Physics* **2012,** *14* (16), 5785-5794.
117. Li, J.-R.; Ma, Y.; McCarthy, M. C.; Sculley, J.; Yu, J.; Jeong, H.-K.; Balbuena, P. B.; Zhou, H.-C., Carbon Dioxide Capture-Related Gas Adsorption and Separation in Metal-Organic Frameworks. *Coordination Chemistry Reviews* **2011,** *255* (15), 1791-1823.
118. Khan, N. A.; Hasan, Z.; Jhung, S. H., Adsorptive Removal of Hazardous Materials Using Metal-Organic Frameworks (MOFs): A Review. *Journal of Hazardous Materials* **2013,** *244*, 444-456.

119. Britt, D.; Tranchemontagne, D.; Yaghi, O. M., Metal-Organic Frameworks with High Capacity and Selectivity for Harmful Gases. *Proceedings of the National Academy of Sciences* **2008,** *105* (33), 11623-11627.
120. Lei, Z.; Dai, C.; Chen, B., Gas Solubility in Ionic Liquids. *Chemical Reviews* **2013,** *114* (2), 1289-1326.
121. Lei, Z.; Dai, C.; Song, W., Adsorptive Absorption: A Preliminary Experimental and Modeling Study on CO_2 Solubility. *Chemical Engineering Science* **2015,** *127*, 260-268.
122. Ding, L.-G.; Yao, B.-J.; Jiang, W.-L.; Li, J.-T.; Fu, Q.-J.; Li, Y.-A.; Liu, Z.-H.; Ma, J.-P.; Dong, Y.-B., Bifunctional Imidazolium-Based Ionic Liquid Decorated UiO-67 Type MOF for Selective CO_2 Adsorption and Catalytic Property for CO_2 Cycloaddition with Epoxides. *Inorganic Chemistry* **2017,** *56* (4), 2337-2344.
123. Sumer, Z.; Keskin, S., Ranking of MOF Adsorbents for CO_2 Separations: A Molecular Simulation Study. *Ind. Chem. Eng. Res.* **2016**.
124. Chen, Y.; Hu, Z.; Gupta, K. M.; Jiang, J., Ionic Liquid/Metal–Organic Framework Composite for CO_2 Capture: A Computational Investigation. *J. Phys. Chem. C* **2011,** *115* (44), 21736-21742.
125. Anthony, J. L.; Anderson, J. L.; Maginn, E. J.; Brennecke, J. F., Anion Effects on Gas Solubility in Ionic Liquids. *Journal of Physical Chemistry B* **2005,** *109* (13), 6366-6374.
126. Vicent-Luna, J. M.; Gutiérrez-Sevillano, J. J.; Anta, J. A.; Calero, S., Effect of Room-Temperature Ionic Liquids on CO_2 Separation by a Cu-BTC Metal–Organic Framework. *J. Phys. Chem. C* **2013,** *117* (40), 20762-20768.
127. Odoh, S. O.; Cramer, C. J.; Truhlar, D. G.; Gagliardi, L., Quantum-Chemical Characterization of the Properties and Reactivities of Metal–Organic Frameworks. *Chemical Reviews* **2015,** *115* (12), 6051-6111.
128. Xue, W.; Li, Z.; Huang, H.; Yang, Q.; Liu, D.; Xu, Q.; Zhong, C., Effects of Ionic Liquid Dispersion in Metal-Organic Frameworks and Covalent Organic Frameworks on CO_2 Capture: A Computational Study. *Chemical Engineering Science* **2016,** *140*, 1-9.
129. Cadena, C.; Anthony, J. L.; Shah, J. K.; Morrow, T. I.; Brennecke, J. F.; Maginn, E. J., Why is CO_2 So Soluble in Imidazolium-Based Ionic Liquids? *Journal of the American Chemical Society* **2004,** *126* (16), 5300-5308.
130. Available from: https://chem.libretexts.org/Core/Physical_and_Theoretical_Chemistry/Spectroscopy/Vibrational_Spectroscopy/Infrared_Spectroscopy/Infrared%3A_Theory. (accessed June 12, 2017).
131. Garhwal, S., Fourier Transform Infrared (FT-IR) Spectroscopy in An-Overview. *Research Journal of Medicinal Plant* **2011,** *5* (2), 127-135.
132. Wojdyr, M., Fityk: A General-Purpose Peak Fitting Program. *J. Appl. Crystallogr*. **2010,** *43* (5 Part 1), 1126-1128.
133. Bunaciu, A. A.; Udriştioiu, E. g.; Aboul-Enein, H. Y., X-Ray Diffraction: Instrumentation and Applications. *Critical Reviews in Analytical Chemistry* **2015,** *45* (4), 289-299.
134. Available from: http://serc.carleton.edu/research_education/geochemsheets/techniques/SEM.html (accessed June 12, 2017).

135. Hwang, N.; Barron, A., BET Surface Area Analysis of Nanoparticles. *The Connexions Project* **2011**, 1-11.
136. Brunauer, S.; Emmett, P. H.; Teller, E., Adsorption of Gases in Multimolecular Layers. *Journal of the American Chemical Society* **1938,** *60* (2), 309-319.
137. Jacquemin, J.; Husson, P.; Majer, V.; Gomes, M. F. C., Low-Pressure Solubilities and Thermodynamics of Solvation of Eight Gases in 1-Butyl-3-Methylimidazolium Hexafluorophosphate. *Fluid Phase Equilibria* **2006,** *240* (1), 87-95.
138. Zhang, S.; Li, L.; Kumar, A., *Materials Characterization Techniques*. CRC press: 2008.
139. Banerjee, R.; Furukawa, H.; Britt, D.; Knobler, C.; O'Keeffe, M.; Yaghi, O. M., Control of Pore Size and Functionality in Isoreticular Zeolitic Imidazolate Frameworks and Their Carbon Dioxide Selective Capture Properties. *Journal of the American Chemical Society* **2009,** *131* (11), 3875-3877.
140. Akçay, A.; Balci, V.; Uzun, A., Structural Factors Controlling Thermal Stability of Imidazolium Ionic Liquids with 1-n-Butyl-3-Methylimidazolium Cation on γ-Al_2O_3. *Thermochimica Acta* **2014,** *589*, 131-136.
141. Akçay, A.; Babucci, M.; Balci, V.; Uzun, A., A Model to Predict Maximum Tolerable Temperatures of Metal-Oxide-Supported 1-n-Butyl-3-Methylimidazolium Based Ionic Liquids. *Chemical Engineering Science* **2015,** *123*, 588-595.
142. Brouwer, P., Theory of XRF. *Almelo, Netherlands: PANalytical BV* **2006**.
143. Available from: http://archaeometry.missouri.edu/xrf_overview.html (accessed June 12, 2017)
144. Available from: http://particulatesystems.com/Products/HPVA-II-High-Pressure-Volumetric-Analyzer.aspx (accessed June 22, 2016).
145. Yang, Z.; Peng, X.; Cao, D., Carbon Dioxide Capture by PAFs and an Efficient Strategy to Fast Screen Porous Materials for Gas Separation. *The Journal of Physical Chemistry C* **2013,** *117* (16), 8353-8364.
146. Frisch, M.; Trucks, G.; Schlegel, H. B.; Scuseria, G.; Robb, M.; Cheeseman, J.; Scalmani, G.; Barone, V.; Mennucci, B.; Petersson, G.; Nakatsuji, H.; Caricato, M.; Li, X.; Hratchian, H. P.; Izmaylov, A. F.; Bloino, J.; Zheng, G.; Sonnenberg, J. L.; Hada, M.; Ehara, M.; Toyota, K.; Fukuda, R.; Hasegawa, J.; Ishida, M.; Nakajima, T.; Honda, Y.; Kitao, O.; Nakai, H.; Vreven, T.; Montgomery Jr., J. A.; Peralta, J. E.; Ogliaro, F.; Bearpark, M. J.; Heyd, J.; Brothers, E. N.; Kudin, K. N.; Staroverov, V. N.; Kobayashi, R.; Normand, J.; Raghavachari, K.; Rendell, A. P.; Burant, J. C.; Iyengar, S. S.; Tomasi, J.; Cossi, M.; Rega, N.; Millam, N. J.; Klene, M.; Knox, J. E.; Cross, J. B.; Bakken, V.; Adamo, C.; Jaramillo, J.; Gomperts, R.; Stratmann, R. E.; Yazyev, O.; Austin, A. J.; Cammi, R.; Pomelli, C.; Ochterski, J. W.; Martin, R. L.; Morokuma, K.; Zakrzewski, V. G.; Voth, G. A.; Salvador, P.; Dannenberg, J. J.; Dapprich, S.; Daniels, A. D.; Farkas, Ö.; Foresman, J. B.; Ortiz, J. V.; Cioslowski, J.; Fox, D. J., Gaussian 09, Revision A. 02, Gaussian. *Inc., Wallingford, CT* **2009,** *200*.
147. Becke, A. D., Density-Functional Thermochemistry. III. The Role of Exact Exchange. *Journal of Chemical Physics* **1993,** *98* (7), 5648-5652.
148. Lee, C.; Yang, W.; Parr, R. G., Development of the Colle-Salvetti Correlation-Energy Formula into a Functional of the Electron Density. *Physical Review B, PRB* **1988,** *37* (2), 785.

149. Balci, V.; Uzun, A., Understanding Spectroscopic Features of Trihexyltetradecylphosphonium Chloride. *ChemistrySelect* **2016,** *1* (4), 741-747.
150. Allen, F. H., The Cambridge Structural Database: A Quarter of a Million Crystal Structures and Rising. *Acta Crystallogaphica., Section B: Structure Science* **2002,** *58* (3), 380-388.
151. Wu, H.; Zhou, W.; Yildirim, T., Hydrogen Storage in a Prototypical Zeolitic Imidazolate Framework-8. *Journal of the American Chemical Society* **2007,** *129* (17), 5314-5315.
152. Merrick, J. P.; Moran, D.; Radom, L., An Evaluation of Harmonic Vibrational Frequency ScaleFactors. *Journal of Physical Chemistry A* **2007,** *111* (45), 11683-11700.
153. Foster, J.; Weinhold, F., Natural Hybrid Orbitals. *Journal of the American Chemical Society* **1980,** *102* (24), 7211-7218.
154. Grimme, S.; Ehrlich, S.; Goerigk, L., Effect of the Damping Function in Dispersion Corrected Density Functional Theory. *Journal of Computational Chemistry* **2011,** *32* (7), 1456-1465.
155. Akkermans, R. L.; Spenley, N. A.; Robertson, S. H., Monte Carlo Methods in Materials Studio. *Molecular Simulations* **2013,** *39* (14-15), 1153-1164.
156. Materials Studio v8.0; Biovia Software Inc., **2007**.
157. Mercado, R.; Vlaisavljevich, B.; Lin, L.-C.; Lee, K.; Lee, Y.; Mason, J. A.; Xiao, D. J.; Gonzalez, M. I.; Kapelewski, M. T.; Neaton, J. B.; Smit, B., Force Field Development from Periodic Density Functional Theory Calculations for Gas Separation Applications Using Metal–Organic Frameworks. *The Journal of Physical Chemistry C* **2016,** *120* (23), 12590-12604.
158. Rappé, A. K.; Casewit, C. J.; Colwell, K.; Goddard Iii, W.; Skiff, W., UFF, A Full Periodic Table Force Field for Molecular Mechanics and Molecular Dynamics Simulations. *Journal of the American Chemical Society* **1992,** *114* (25), 10024-10035.
159. Pérez-Pellitero, J.; Amrouche, H.; Siperstein, F. R.; Pirngruber, G.; Nieto-Draghi, C.; Chaplais, G.; Simon-Masseron, A.; Bazer-Bachi, D.; Peralta, D.; Bats, N., Adsorption of CO_2, CH_4, and N_2 on zeolitic imidazolate frameworks: experiments and simulations. *Chem. Eur. J.* **2010,** *16* (5), 1560-1571.
160. Goodbody, S. J.; Watanabe, K.; MacGowan, D.; Walton, J. P.; Quirke, N., Molecular Simulation of Methane and Butane in Silicalite. *J. Chem. Soc., Faraday Trans.* **1991,** *87* (13), 1951-1958.
161. Galassi, G.; Tildesley, D., Phase Diagrams of Diatomic Molecules Using the Gibbs Ensemble Monte Carlo Method. *Molecular Simulation* **1994,** *13* (1), 11-24.
162. Simon, C. M.; Smit, B.; Haranczyk, M., pyIAST: Ideal Adsorbed Solution Theory (IAST) Python Package. *Computer Physics Communications* **2016,** *200*, 364-380.
163. Myers, A.; Prausnitz, J. M., Thermodynamics of Mixed-Gas Adsorption. *AIChE Journal* **1965,** *11* (1), 121-127.
164. Keskin, S., Atomistic Simulations for Adsorption, Diffusion, and Separation of Gas Mixtures in Zeolite Imidazolate Frameworks. *The Journal of Physical Chemistry C* **2010,** *115* (3), 800-807.

165. McEwen, J.; Hayman, J.-D.; Yazaydin, A. O., A Comparative Study of CO_2, CH_4 and N_2 Adsorption in ZIF-8, Zeolite-13X and BPL Activated Carbon. *Chemical Physics* **2013,** *412*, 72-76.
166. Zhang, Z.; Xian, S.; Xia, Q.; Wang, H.; Li, Z.; Li, J., Enhancement of CO_2 Adsorption and CO_2/N_2 Selectivity on ZIF-8 via Postsynthetic Modification. *AIChE Journal* **2013,** *59* (6), 2195-2206.
167. Bux, H.; Chmelik, C.; Krishna, R.; Caro, J., Ethene/Ethane Separation by the MOF Membrane ZIF-8: Molecular Correlation of Permeation, Adsorption, Diffusion. *Journal of Membrane Science* **2011,** *369* (1), 284-289.
168. Saha, D.; Bao, Z.; Jia, F.; Deng, S., Adsorption of CO_2, CH_4, N_2O, and N_2 on MOF-5, MOF-177, and Zeolite 5A. *Environmental Science & Technology* **2010,** *44* (5), 1820-1826.
169. Zhang, C.; Dai, Y.; Johnson, J. R.; Karvan, O.; Koros, W. J., High Performance ZIF-8/6FDA-DAM Mixed Matrix Membrane for Propylene/Propane Separations. *Journal of Membrane Science* **2012,** *389*, 34-42.
170. Tran, U. P.; Le, K. K.; Phan, N. T., Expanding Applications of Metal-Organic Frameworks: Zeolite Imidazolate Framework ZIF-8 as an Efficient Heterogeneous Catalyst for the Knoevenagel Reaction. *ACS Catalysis* **2011,** *1* (2), 120-127.
171. Babucci, M.; Balci, V.; Akçay, A.; Uzun, A., Interactions of [BMIM][BF_4] with Metal Oxides and Their Consequences on Stability Limits. *The Journal of Physical Chemistry C* **2016,** *120* (36), 20089-20102.
172. Eslava, S.; Zhang, L.; Esconjauregui, S.; Yang, J.; Vanstreels, K.; Baklanov, M. R.; Saiz, E., Metal-Organic Framework ZIF-8 Films as Low-κ Dielectrics in Microelectronics. *Chemistry of Materials* **2012,** *25* (1), 27-33.
173. Hu, Y.; Kazemian, H.; Rohani, S.; Huang, Y.; Song, Y., In Situ High Pressure Study of ZIF-8 by FTIR Spectroscopy. *Chemical Communications* **2011,** *47* (47), 12694-12696.
174. Huang, X. C.; Lin, Y. Y.; Zhang, J. P.; Chen, X. M., Ligand-Directed Strategy for Zeolite-Type Metal–Organic Frameworks: Zinc (II) Imidazolates with Unusual Zeolitic Topologies. *Angewandte Chemie* **2006,** *118* (10), 1587-1589.
175. Cravillon, J.; Münzer, S.; Lohmeier, S.-J.; Feldhoff, A.; Huber, K.; Wiebcke, M., Rapid Room-Temperature Synthesis and Characterization of Nanocrystals of a Prototypical Zeolitic Imidazolate Framework. *Chemistry of Materials* **2009,** *21* (8), 1410-1412.
176. Lee, Y.-R.; Jang, M.-S.; Cho, H.-Y.; Kwon, H.-J.; Kim, S.; Ahn, W.-S., ZIF-8: A Comparison of Synthesis Methods. *Chemical Engineering Journal* **2015,** *271*, 276-280.
177. Babucci, M.; Akçay, A.; Balci, V.; Uzun, A., Thermal Stability Limits of Imidazolium Ionic Liquids Immobilized on Metal-Oxides. *Langmuir* **2015,** *31* (33), 9163-9176.
178. Talaty, E. R.; Raja, S.; Storhaug, V. J.; Dölle, A.; Carper, W. R., Raman and Infrared Spectra and ab Initio Calculations of C2-4MIM Imidazolium Hexafluorophosphate Ionic Liquids. *The Journal of Physical Chemistry B* **2004,** *108* (35), 13177-13184.
179. Li, X.; Liu, L.; Schlegel, H. B., On the Physical Origin of Blue-Shifted Hydrogen Bonds. *Journal of the American Chemical Society* **2002,** *124* (32), 9639-9647.

180. Tripathi, A. K.; Verma, Y. L.; Singh, R. K., Thermal, Electrical and Structural Studies on Ionic Liquid Confined in Ordered Mesoporous MCM-41. *Journal of Materials Chemistry A* **2015,** *3* (47), 23809-23820.
181. Antony, J.; Sure, R.; Grimme, S., Using Dispersion-Corrected Density Functional Theory to Understand Supramolecular Binding Thermodynamics. *Chemical Communications* **2015,** *51* (10), 1764-1774.
182. Battisti, A.; Taioli, S.; Garberoglio, G., Zeolitic Imidazolate Frameworks for Separation of Binary Mixtures of CO_2, CH_4, N_2 and H_2: A Computer Simulation Investigation. *Microporous and Mesoporous Materials* **2011,** *143* (1), 46-53.
183. Zhou, W.; Wu, H.; Hartman, M. R.; Yildirim, T., Hydrogen and Methane Adsorption in Metal−Organic Frameworks: A High-Pressure Volumetric Study. *The Journal of Physical Chemistry C* **2007,** *111* (44), 16131-16137.
184. Yuan, B.; Wu, X.; Chen, Y.; Huang, J.; Luo, H.; Deng, S., Adsorption of CO_2, CH_4, and N_2 on Ordered Mesoporous Carbon: Approach for Greenhouse Gases Capture and Biogas Upgrading. *Environmental Science & Technology* **2013,** *47* (10), 5474-5480.
185. Ho, M. T.; Allinson, G. W.; Wiley, D. E., Reducing the Cost of CO_2 Capture From Flue Gases Using Pressure Swing Adsorption. *Industrial & Engineering Chemistry Research* **2008,** *47* (14), 4883-4890.
186. Fang, Z.; Bueken, B.; De Vos, D. E.; Fischer, R. A., Defect-Engineered Metal–Organic Frameworks. *Angewandte Chemie International Edition* **2015,** *54* (25), 7234-7254.
187. Wu, H.; Chua, Y. S.; Krungleviciute, V.; Tyagi, M.; Chen, P.; Yildirim, T.; Zhou, W., Unusual and Highly Tunable Missing-Linker Defects in Zirconium Metal–Organic Framework UiO-66 and Their Important Effects on Gas Adsorption. *Journal of the American Chemical Society* **2013,** *135* (28), 10525-10532.
188. Available from: http://www.sigmaaldrich.com/catalog/product/sial/18122?lang=en&region= TR (accessed July 10, 2017)
189. Nobar, S. N. Adsorption and Diffusion of Gases in Cu-BTC. 2012.
190. Sun, B.; Kayal, S.; Chakraborty, A., Study of HKUST (Copper Benzene-1,3,5-Tricarboxylate, Cu-BTC MOF)-1 Metal Organic Frameworks for CH_4 Adsorption: An Experimental Investigation with GCMC (Grand Canonical Monte-Carlo) Simulation. *Energy* **2014,** *76*, 419-427.
191. Czaja, A. U.; Trukhan, N.; Müller, U., Industrial Applications of Metal–Organic Frameworks. *Chemical Society Reviews* **2009,** *38* (5), 1284-1293.
192. Gimeno-Fabra, M.; Munn, A. S.; Stevens, L. A.; Drage, T. C.; Grant, D. M.; Kashtiban, R. J.; Sloan, J.; Lester, E.; Walton, R. I., Instant MOFs: Continuous Synthesis of Metal-Organic Frameworks by Rapid Solvent Mixing. *Chemical Communications* **2012,** *48* (86), 10642-10644.
193. Autie-Castro, G.; Autie, M.; Rodríguez-Castellón, E.; Aguirre, C.; Reguera, E., Cu-BTC and Fe-BTC Metal-Organic Frameworks: Role of the Materials Structural Features on Their Performance for Volatile Hydrocarbons Separation. *Colloids and Surfaces A: Physicochemical and Engineering Aspects* **2015,** *481*, 351-357.

194. Luo, Q.-x.; Ji, M.; Park, S.-E.; Hao, C.; Li, Y.-q., $PdCl_2$ Immobilized on Metal–Organic Framework CuBTC with the Aid of Ionic Liquids: Enhanced Catalytic Performance in Selective Oxidation of Cyclohexene. *RSC Advances* **2016,** *6* (39), 33048-33054.
195. Yang, Y.; Shukla, P.; Wang, S.; Rudolph, V.; Chen, X.-M.; Zhu, Z., Significant Improvement of Surface Area and CO_2 Adsorption of Cu-BTC via Solvent Exchange Activation. *RSC Advances* **2013,** *3* (38), 17065-17072.
196. Yoon, J. W.; Jang, I. T.; Lee, K.-Y.; Hwang, Y. K.; Chang, J.-S., Adsorptive Separation of Propylene and Propane on a Porous Metal-Organic Framework, Copper Trimesate. *Bulletin of Korean Chemical Society* **2010,** *31* (1), 220-223.
197. Majano, G.; Pérez-Ramírez, J., Scalable Room-Temperature Conversion of Copper(II) Hydroxide into HKUST-1 ($Cu_3(BTC)_2$). *Advanced Materials* **2013,** *25* (7), 1052-1057.
198. Ullah, Z. B., M. A.; Man, Z. and Khan, A. S., Phosphonium-Based Ionic Liquids and Their Application in Separation of Dye from Aqueous Solution. *Journal of Engineering and Applied Sciences* **2016,** *11* (3), 1653-1659.
199. Zhu, J.; Xin, F.; Sun, Y.; Dong, X., Phosphonium-Based Ionic Liquids Grafted onto Silica for CO Sorption. *Theoretical Foundations of Chemical Engineering* **2014,** *48* (6).
200. Murakami, S.; Matsumiya, M.; Yamada, T.; Tsunashima, K., Extraction of Pr (III), Nd (III), and Dy (III) from HTFSA Aqueous Solution by TODGA/Phosphonium-Based Ionic Liquids. *Solvent Extraction and Ion Exchange* **2016,** *34* (2), 172-187.
201. Kiefer, J.; Fries, J.; Leipertz, A., Experimental Vibrational Study of Imidazolium-Based Ionic Liquids: Raman and Infrared Spectra of 1-Ethyl-3-Methylimidazolium Bis(trifluoromethylsulfonyl)imide and 1-Ethyl-3-Methylimidazolium Ethylsulfate. *Applied Spectroscopy* **2007,** *61* (12), 1306-1311.
202. Battez, A. H.; Bartolomé, M.; Blanco, D.; Viesca, J.; Fernández-González, A.; González, R., Phosphonium Cation-Based Ionic Liquids as Neat Lubricants: Physicochemical and Tribological Performance. *Tribology International* **2016,** *95*, 118-131.
203. Li, P.; Paul, D.; Chung, T.-S., High Performance Membranes Based on Ionic Liquid Polymers for CO_2 Separation from the Flue Gas. *Green Chemistry* **2012,** *14* (4), 1052-1063.
204. Mason, J. A.; Veenstra, M.; Long, J. R., Evaluating Metal-Organic Frameworks for Natural Gas Storage. *Chemical Science* **2014,** *5* (1), 32-51.
205. Chowdhury, P.; Mekala, S.; Dreisbach, F.; Gumma, S., Adsorption of CO, CO_2 and CH_4 on Cu-BTC and MIL-101 Metal Organic Frameworks: Effect of Open Metal Sites and Adsorbate Polarity. *Microporous and Mesoporous Materials* **2012,** *152* (0), 246-252.
206. Moellmer, J.; Moeller, A.; Dreisbach, F.; Glaeser, R.; Staudt, R., High Pressure Adsorption of Hydrogen, Nitrogen, Carbon Dioxide and Methane on the Metal-Organic Framework HKUST-1. *Microporous and Mesoporous Materials* **2011,** *138* (1–3), 140-148.

APPENDIX A: Supplementary Computational Results[‡]

Table A.1. LJ parameters for ZIF-8 and [BMIM][PF_6]

ZIF-8		
For CO_2	**Energy (kJ/mol)**	**Distance (Å)**
C	0.44	3.85
H	0.18	2.89
N	0.29	3.66
Zn	0.52	2.76
ZIF-8*		
For CH_4 and N_2	**Energy (kJ/mol)**	**Distance (Å)**
C	0.18	3.66
H	0.13	2.74
N	0.20	3.48
Zn	0.35	2.63
[BMIM][PF_6]		
For CO_2	**Energy (kJ/mol)**	**Distance (Å)**
C	0.44	3.85
H	0.18	2.89
N	0.29	3.66
P	1.28	4.15
F	0.21	3.36
[BMIM][PF_6]		
For CH_4 and N_2	**Energy (kJ/mol)**	**Distance (Å)**
C	0.30	3.66
H	0.13	2.74
N	0.20	3.48
P	0.88	3.94
F	0.14	3.20

[‡] The results given in this chapter were published in ACS Applied Materials and Interfaces as the Supporting Information with following reference: Kinik, F. P.; Altintas, C.; Balci, V.; Koyuturk, B.; Uzun, A.; Keskin, S., [BMIM][PF_6] Incorporation Doubles CO_2 Selectivity of ZIF-8: Elucidation of Interactions and Their Consequences on Performance. ACS Applied Materials and Interfaces, **2016**, *8* (45), 30992–31005. This chapter is the reformatted version of the mentioned research paper

*Energy parameter of the carbon atoms of ZIF-8 are given as multiplied with a factor of 0.6 for CH_4 and N_2 adsorption simulations in [BMIM][PF_6]/ZIF-8 to have a better agreement with the experimental results.

Table A.2. LJ parameters and charges used for gas molecules

CO_2	**Energy (kJ/mol)**	**Distance (Å)**	**Charge**
O	0.25	3.50	-0.29
C	0.46	3.85	0.58
O	0.25	3.50	-0.29
CH_4	**Energy (kJ/mol)**	**Distance (Å)**	**Charge**
C	1.21	4.20	-
N_2	**Energy (kJ/mol)**	**Distance (Å)**	**Charge**
N	0.29	3.72	-
N	0.29	3.72	-

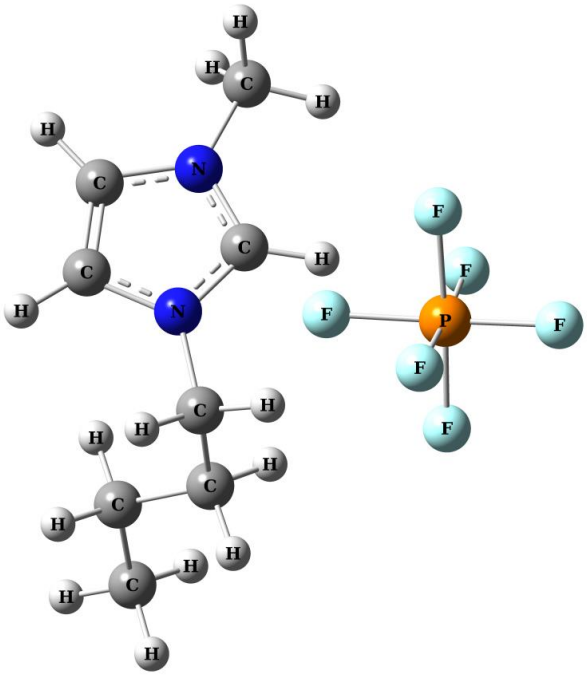

Figure A.1. The lowest energy equilibrium conformer (Conf-1) acquired for [BMIM][PF_6].

Table A.3. XYZ coordinates of the lowest energy equilibrium geometry (Conf-1) for [BMIM][PF_6] optimized at B3LYP/6-311+G(2d,p)

Atom	X	Y	Z
C	-0.96335500	1.38439700	0.61240400
C	-2.46574400	2.39107200	-0.64635500
C	-3.06456700	1.33126100	-0.04643000
N	-2.11002100	0.71505500	0.73842100
H	-0.02700800	1.11267400	1.07216300
H	-2.85465400	3.12329400	-1.33141700
H	-4.07377100	0.96639400	-0.11145900
H	-1.64059000	-0.45299300	2.38547400
C	-2.27647200	-0.53822000	1.50535100
C	-1.91353700	-1.79280000	0.71019100
H	-3.31564500	-0.55853100	1.83897200
C	-2.79575500	-2.07123500	-0.50800000
H	-1.98801700	-2.62847400	1.41450200
H	-0.86460100	-1.73020300	0.41543900
C	-2.42033200	-3.38215000	-1.20170100
H	-2.70203800	-1.25165000	-1.22763600
H	-3.84980300	-2.10506400	-0.20386300
H	-3.04979000	-3.56052800	-2.07602100
H	-1.38023400	-3.36200400	-1.53397900
H	-2.53776400	-4.23364000	-0.52629000
N	-1.15202100	2.40595900	-0.22178700
C	-0.11366200	3.34807000	-0.64954800
H	0.85185700	2.95740200	-0.33890700
H	-0.13410100	3.42295600	-1.73529500
H	-0.29642200	4.32574100	-0.20438800

P	2.16050700	-0.33772700	-0.01279700
F	2.07528800	1.28165000	0.36709700
F	1.14982800	-0.61916700	1.28060800
F	0.80568300	-0.12803400	-0.94648400
F	2.15244400	-1.91095200	-0.35999800
F	3.43646700	-0.49744100	0.94957400
F	3.08804700	0.00406200	-1.28160300

Table A.4. ZPVE-corrected binding energies (ΔEB) of all [BMIM][PF_6] conformers

Conformer ID	**ΔE_B (kJ/mol)**
Conf-1	-314.83
Conf-2	-313.68
Conf-3	-313.54
Conf-4	-284.27

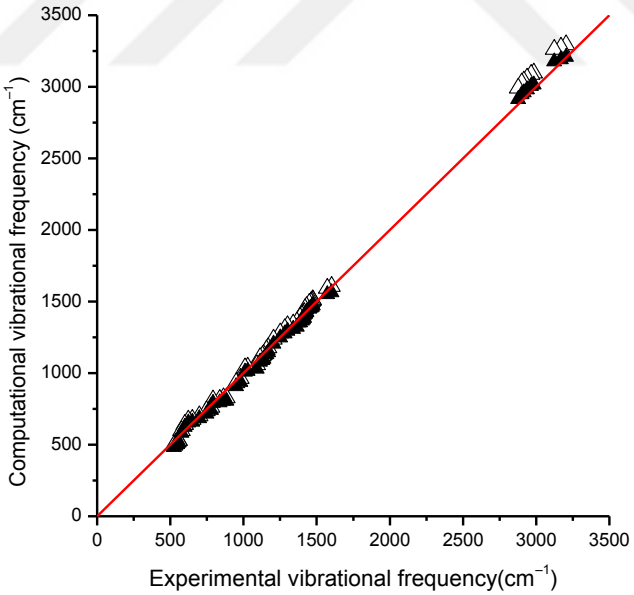

Figure A.2. The relationship between experimental and DFT-computed vibrational frequencies of [BMIM][PF_6]. Open and closed triangles represent unscaled and scaled (by a factor of 0.9742) vibrational frequencies, respectively (R^2=0.9993)

APPENDIX B: Supplementary Experimental Results[§]

Table B.1. The assignments of experimental and computational IR spectrum of [BMIM][PF_6]

Assignments	Vibrational frequencies (cm^{-1})		
	Exp.	**Comp.**	**Scaled Comp.**
C4,5-H symmetric stretching	3205	3294	3209
C4,5-H asymmetric stretching	3170	3277	3192
C2-H stretching	3124	3261	3177
CH_3 HCH asymmetric stretching and CH_2 HCH asymmetric stretching on butyl	2984	3095	3015
CH_3 HCH asymmetric stretching and CH_2CC(N) HCH asymmetric stretching on butyl	2965	3086	3006
CH_2(N) HCH symmetric stretching on butyl	2938	3061	2982
CH_3(N) HCH symmetric stretching on methyl	2938	3060	2981
CH_2CC(N) HCH asymmetric stretching and CH_2C(N) HCH symmetric stretching on butyl	2916	3039	2961
CH_3 HCH symmetric stretching on butyl	2901	3026	2948
CH_2CC(N) HCH symmetric stretching on butyl	2877	2991	2914
CH_3(N) HCH bending, ring in plane asymmetric stretching	1603	1605	1564
CH_3(N) HCH bending, CH_2(N) HCH scissoring, ring in plane asymmetric stretching	1572	1592	1551
CH_2CH_2C(N) and CH_3 HCH scissoring on butyl	1474	1512	1473
CH_3(N) HCH scissoring on methyl	1474	1510	1471

[§] The results given in this chapter were published in ACS Applied Materials and Interfaces as the Supporting Information with following reference: Kinik, F. P.; Altintas, C.; Balci, V.; Koyuturk, B.; Uzun, A.; Keskin, S., [BMIM][PF_6] Incorporation Doubles CO_2 Selectivity of ZIF-8: Elucidation of Interactions and Their Consequences on Performance. ACS Applied Materials and Interfaces, **2016**, *8* (45), 30992–31005. This chapter is the reformatted version of the mentioned research paper.

CH_3 HCH scissoring on butyl, CH_3(N) HCH scissoring on methyl	1468	1501	1462
CH_2CH_2C(N) HCH scissoring and CH_3 HCH scissoring on butyl	1461	1496	1457
CH_2(N) HCH scissoring	1461	1495	1456
CH_2CH_2C(N) HCH scissoring	1449	1487	1449
CH_3(N) HCH symmetric bending on methyl	1431	1465	1427
ring in plane asymmetric stretching, CH_2(N) HCH twist, CH_2C(N) HCH wagging, CH_3(N) HCH scissoring on methyl	1420	1449	1412
CH_3 HCH symmetric bending on butyl, CH_2C(N) HCH wagging	1414	1422	1385
CH_3 HCH symmetric bending on butyl, CH_2CH_2C(N) HCH wagging, ring in plane asymmetric stretching	1407	1411	1375
CH_2CH_2C(N) HCH wagging, CH_2(N) HCH twist, ring in plane asymmetric stretching, CH_3(N) HCH scissoring on methyl	1400	1403	1367
CH_2(N) HCH wagging, CH_2C(N) HCH twist	1387	1389	1353
CH_2CH_2(N) HCH twist, CH_2CC(N) HCH wagging, ring in plane symmetric stretching	1366	1358	1323
$CH_2CH_2CH_2$(N) HCH wagging, CH_3 HCH bending on butyl, ring in plane symmetric stretching	1339	1342	1307
$CH_2CH_2CH_2$(N) HCH twist, CH_3 HCH bending on butyl	1300	1330	1296
CH_2(N) HCH twist, CH_2CH_2C(N) HCH wagging, C4,5-H, and C2-H bending, CH_3(N) HCH bending on methyl	1282	1311	1277
$CH_2CH_2CH_2$(N) HCH twist, CH_3 HCH bending on butyl, C2-H bending	1252	1281	1248
CH_2(N) HCH twist, CH_2C(N) HCH wagging, CH_2CH_2C(N) HCH rocking, CH_3 HCH bending on butyl, C2-H bending	1205	1236	1204
C4,5-H and C2-H bending, CH_2(N) and CH_3(N) N-C stretching	1169	1176	1146
CH_3(N) HCH asymmetric bending	1158	1162	1132
CCCCC str, C4,5-H and C2-H bending, CH_3(N) HCH asymmetric bending	1138	1129	1100
C4,5-H symmetric bending	1130	1120	1091
C4,5-H and C2-H symmetric bending, CH_3(N) HCH asymmetric bending	1113	1108	1079

CCCCC stretching, ring in plane symmetric stretching	1092	1058	1031
ring in plane asymmetric stretching, CH_3(N) N-C stretching	1028	1041	1014
ring in plane symmetric stretching, CH_2(N) N-C stretching, $CH_3CH_2CH_2$ C-C stretching	1010	1036	1009
CH_2(N) HCH rocking, CH_2CH_2C(N) HCH twist, CH_3 HCH asymmetric bending on butyl	980	962	937
C2-H out of plane bending	950	932	908
PF_6 asymmetric stretching, CH_2(N) HCH bending, $CH_3CH_2CH_2$ C-C asymmetric bending	883	828	807
CH_2(N) HCH bending, $CH_3CH_2CH_2$ C-C asymmetric bending	864	827	806
PF_6 asymmetric stretching, C2-H and C4,5-H out of plane bending, CH_2(N) HCH rocking	837	816	795
PF_6 asymmetric stretching, C2-H out of plane bending, CH bending on butyl	792	812	791
CH_2CH_2C(N) HCH rocking and CH_3 HCH rocking on butyl	779	762	742
C4,5-H symmetric out of plane bending, C2-H out of plane bending	748	736	717
N-CH_3 and N-CH_2 N-C stretching, ring bending, CH_2CH_2C(N) HCH rocking	698	702	684
PF_6 symmetric stretching	651	677	660
$CH_2CH_2CH_2$(N) HCH rocking, ring out of plane bending	623	671	654
ring out of plane bending	599	641	624
CH_2C(N) HCH rocking, CH_2(N) and CH_3(N) N-C ring stretching	577	598	583
PF_6 asymmetric stretching	557	531	517
PF_6 asymmetric stretching	557	530	516
PF_6 asymmetric stretching	557	529	515
PF_6 asymmetric stretching	548	518	505
PF_6 asymmetric stretching	536	511	498
CCCC bending on butyl, ring out of plane bending	525	496	483

Table B.2. Shifts in corresponding IR peaks of ZIF-8 and IL/ZIF-8 composite[173]

Assignment	ZIF-8 (exp.)	IL/ZIF-8 (exp.)
Ring C-H stretching bonds	3175	3167
Ring C-H stretching bonds	3141	3147
Ring C-H stretching bonds	3112	3119
Ring C-H stretching bonds	3105	2998
Ring stretching	1486	1478
Ring stretching	1359	1372
In-plane bending of the ring	1173	1167
In-plane bending of the ring	1063	1070
In-plane bending of the ring	973	979
Out of plane bending of the ring	797	804
Out of plane bending of the ring	718	727
Out of plane bending of the ring	643	648
Out of plane bending of the ring	559	565

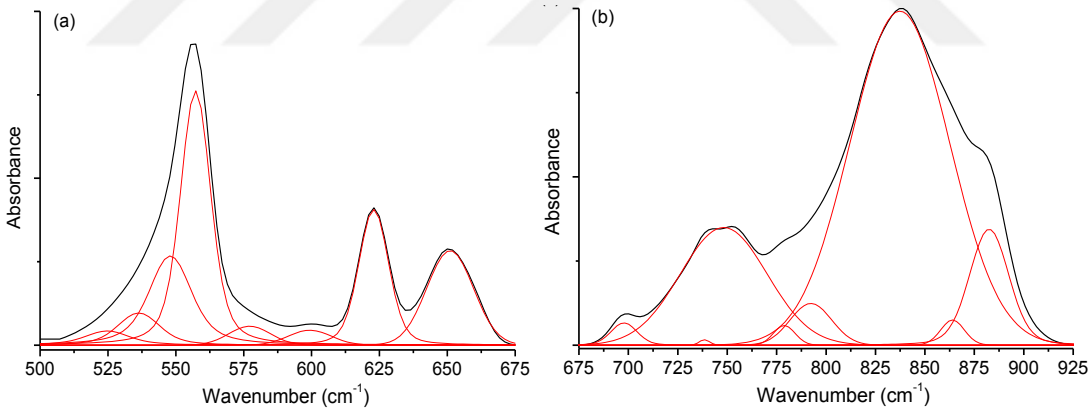

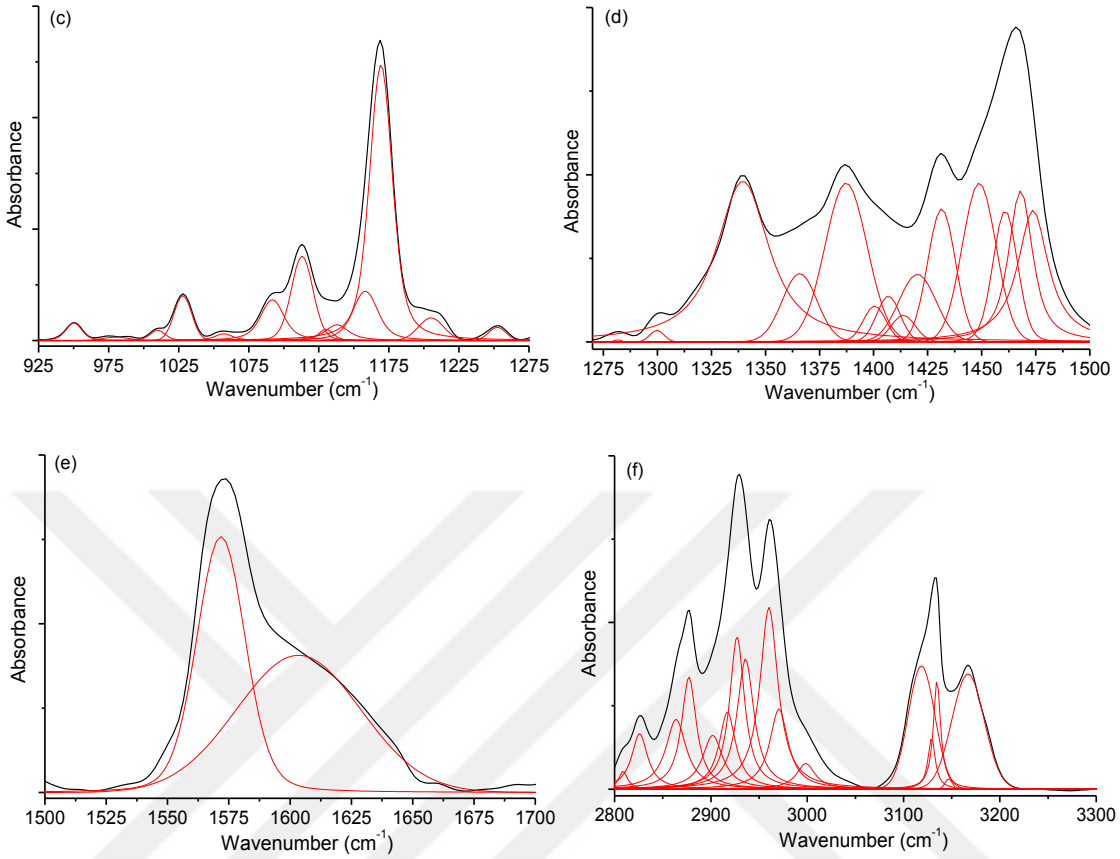

Figure B.1. Deconvoluted peaks of IR spectra of [BMIM][PF_6] in the regions (a) 500-675 cm^{-1}, (b) 675-925 cm^{-1}, (c) 925-1275 cm^{-1}, (d) 1275-1500 cm^{-1}, (e) 1500-1700 cm^{-1}, and (f) 2800-3300 cm^{-1}.

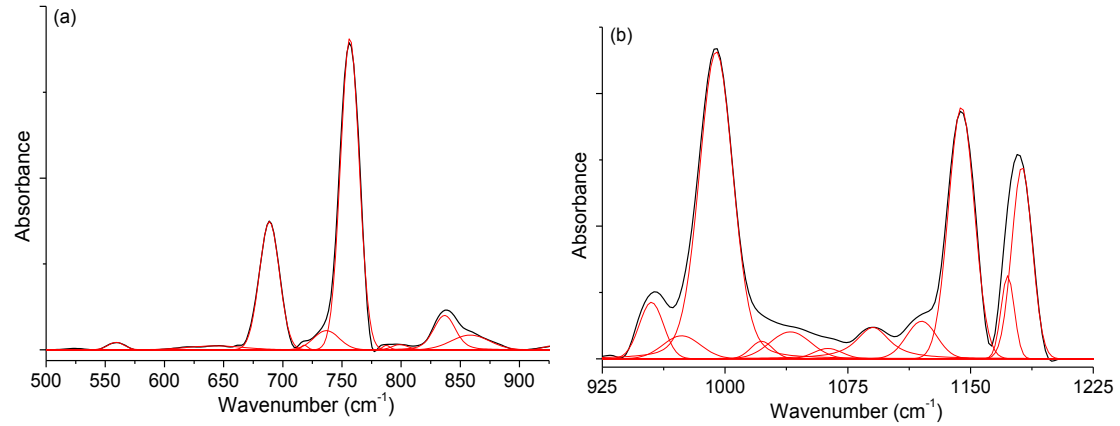

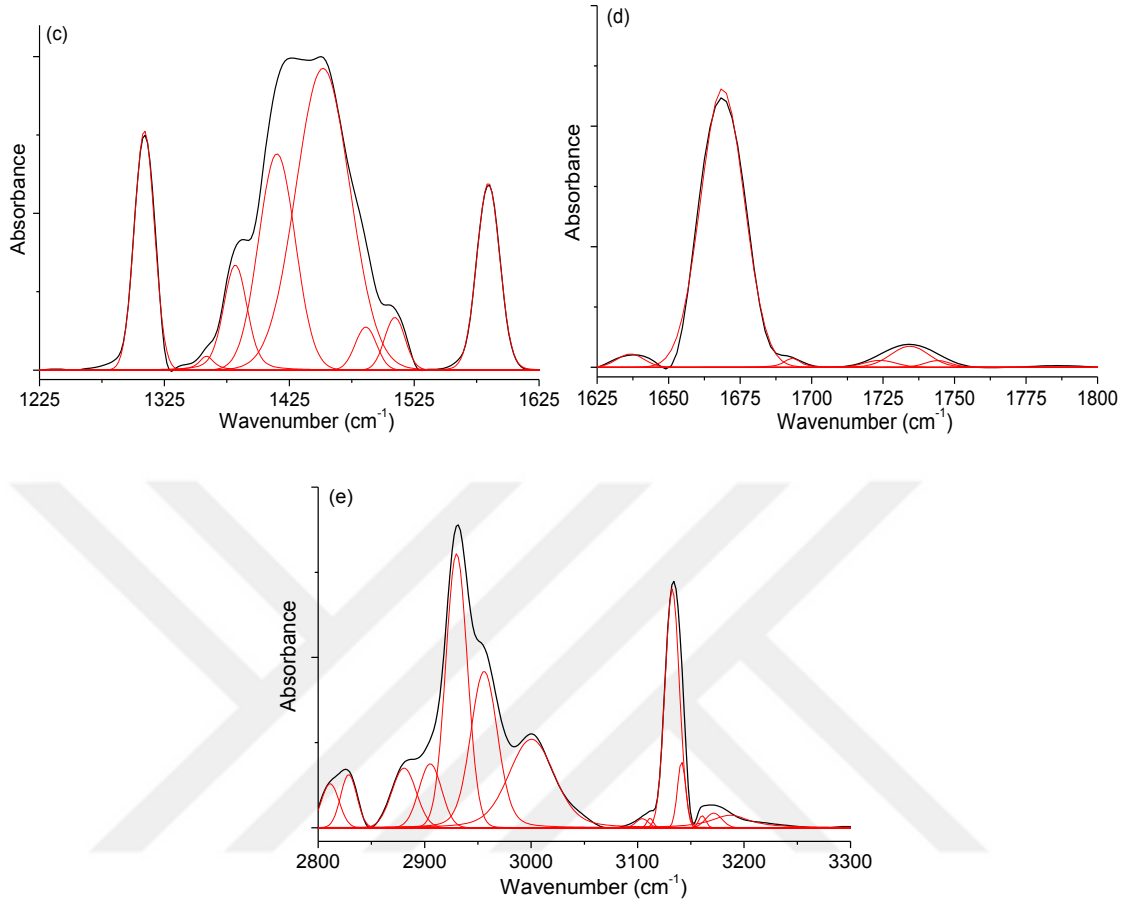

Figure B.2. Deconvoluted peaks of IR spectra of ZIF-8 in the regions (a) 500-925 cm^{-1}, (b) 925-1225 cm^{-1}, (c) 1225-1625 cm^{-1}, (d) 1625-1800 cm^{-1}, and (e) 2800-3300 cm^{-1}

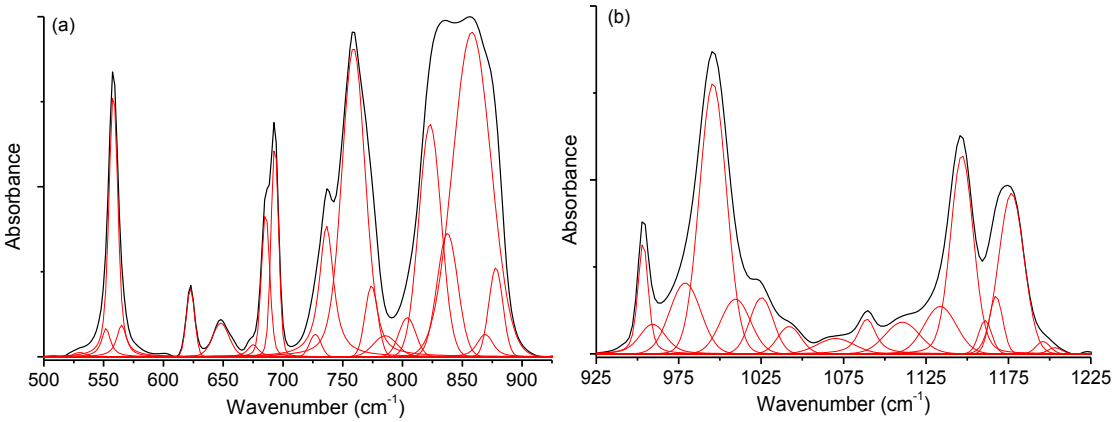

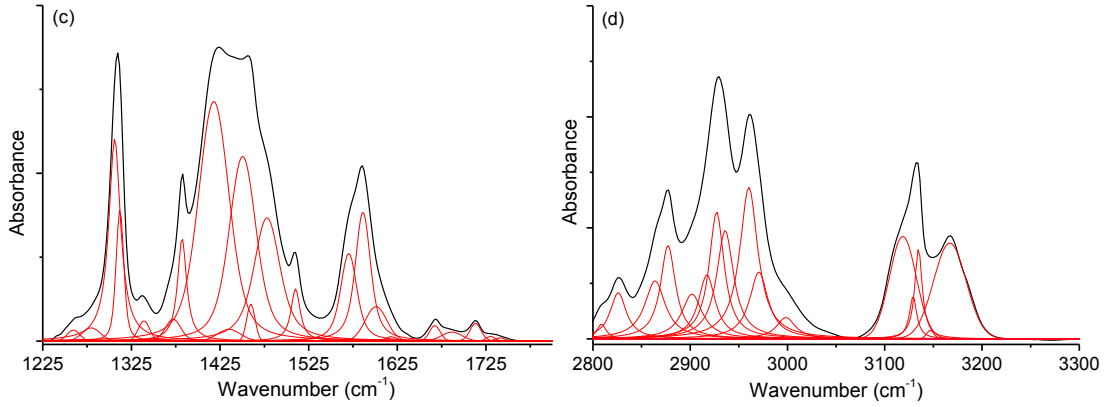

Figure B.3. Deconvoluted peaks of FTIR spectra of [BMIM][PF_6]/ZIF-8 in the regions (a) 500-925 cm^{-1}, (b) 925-1225 cm^{-1}, (c) 1225-1800 cm^{-1}, and (d) 2800-3300 cm^{-1}.

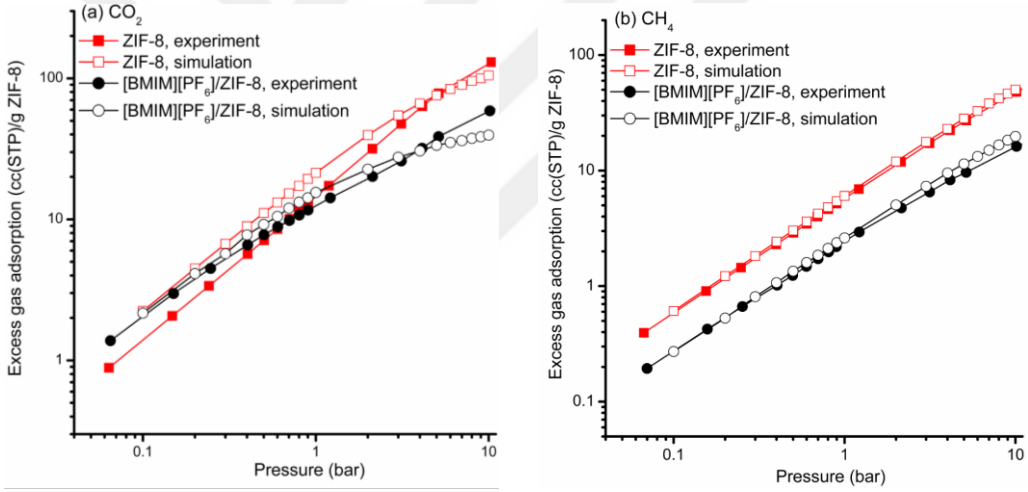

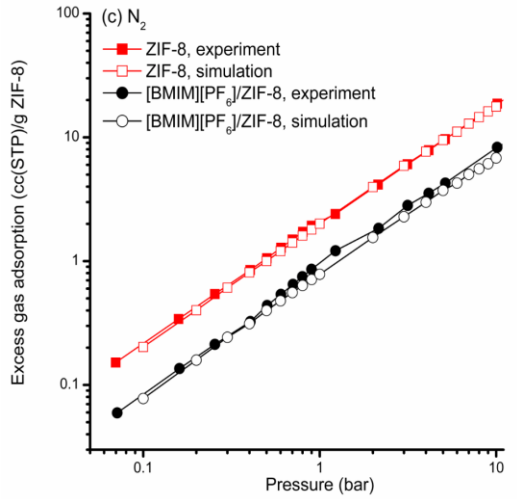

Figure B.4. Comparison of the adsorption isotherms for (a) CO_2, (b) CH_4, and (c) N_2 for both ZIF-8 and [BMIM][PF_6]/ZIF-8.

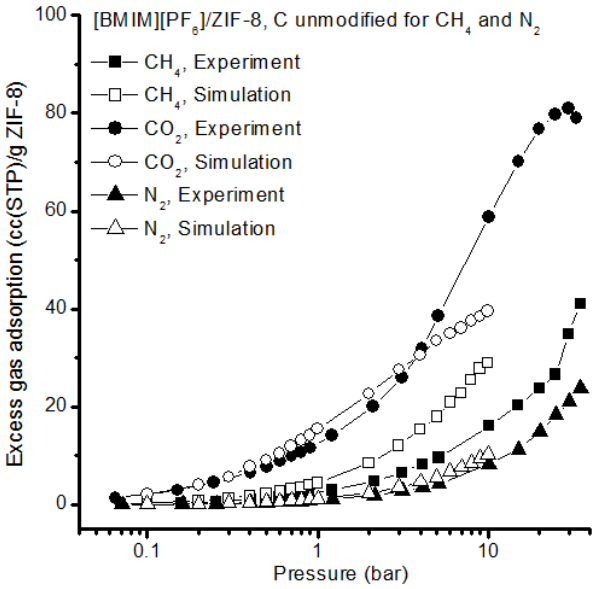

Figure B.5. Experimental single component excess adsorption isotherms of CO_2, CH_4, and N_2 in [BMIM][PF_6]/ZIF-8 up to 35 bar are shown with simulation results when energy parameter (ε) C atom of ZIF-8 is not multiplied with 0.6, measured at room temperature.

Table B.3. Dual site Langmuir parameters used for fitting the gas adsorption of ZIF-8

	Parameters			
Gases	**A**	**B**	**C**	**D**
CH_4	143.35	49.17	143.35	49.17
CO_2	500	61.90	500	61.91
N_2	50	50	49.55	46.44

Table B.4. Dual site Langmuir parameters used for fitting the gas adsorption of [BMIM][PF_6]/ZIF-8

	Parameters			
Gases	**A**	**B**	**C**	**D**
CH_4	17.61	13.60	17.61	13.60
CO_2	200	27.75	7.09	0.35
N_2	17.20	36.20	17.20	36.20

Table B.5. Dual site Langmuir parameters (for CH_4 and N_2) and Freundlich model parameters (for CO_2) used for fitting the gas adsorption of phosphonium-based IL/ZIF-8 composites

	Parameters				
Gases	**A**	**B**	**C**	**D**	
CH_4	377.11 (up to 4 bar) 69.45 (up to 30 bar)	85.05 (up to 4 bar) 27.08 (up to 30 bar)	0.14 (up to 4 bar) 69.43 (up to 30 bar)	0.01 (up to 4 bar) 27.08 (up to 30 bar)	$[P_{4444}][TOS]$/ ZIF-8
CO_2	500 (up to 3 bar) 138.94 (up to 30 bar)	43.09 (up to 3 bar) 18.18 (up to 30 bar)	1.07 (up to 3 bar) 1.63 (up to 30 bar)	-	
N_2	410 (up to 1 bar) 73 (up to 30 bar)	500 (up to 1 bar) 89.09 (up to 30 bar)	410 (up to 1 bar) 69.51 (up to 30 bar)	500 (up to 1 bar) 75.24 (up to 30 bar)	
CH_4	357.63 (up to 4 bar) 63.05 (up to 30 bar)	96.22 (up to 4 bar) 29.46 (up to 30 bar)	0.12 (up to 4 bar) 63.03 (up to 30 bar)	0.02 (up to 4 bar) 29.46 (up to 30 bar)	$[P_{4441}][MeSO_4]$/ ZIF-8

CO_2	13378.3 (up to 3 bar) 117.54 (up to 30 bar)	1361.35 (up to 3 bar) 21.44 (up to 30 bar)	1.03 (up to 3 bar) 1.74 (up to 30 bar)	-	
N_2	21.01 (up to 4 bar) 69.60 (up to 30 bar)	27.16 (up to 4 bar) 92.91 (up to 30 bar)	21.01 (up to 4 bar) 64.68 (up to 30 bar)	26.18 (up to 4 bar) 91.81 (up to 30 bar)	
CH_4	83.06 (up to 5 bar) 62.14 (up to 30 bar)	38.71 (up to 5 bar) 23.83 (up to 30 bar)	101.14 (up to 5 bar) 62.29 (up to 30 bar)	38.31 (up to 5 bar) 23.83 (up to 30 bar)	$[P_{(14)666}][TMPP]$/ ZIF-8
CO_2	479.56 (up to 5 bar) 133.22 (up to 30 bar)	39.52 (up to 5 bar) 76.79 (up to 30 bar)	1.07 (up to 5 bar) 2.33 (up to 30 bar)	-	
N_2	0.20 (up to 5 bar) 475.91 (up to 30 bar)	0.04 (up to 5 bar) 423.22 (up to 30 bar)	81.12 (up to 5 bar) 13.83 (up to 30 bar)	45.15 (up to 5 bar) 19.19 (up to 30 bar)	
CH_4	0.14	0.15	203.03	49.30	$[P_{(14)666}][Br]$/ ZIF-8
CO_2	208.75 (up to 2 bar) 133.07 (up to 30 bar)	17.78 (up to 2 bar) 19.92 (up to 30 bar)	1.16 (up to 2 bar) 1.73 (up to 30 bar)	-	
N_2	170.52	182.58	114.43	182.58	
CH_4	96.46 (up to 5 bar) 58.24 (up to 30 bar)	48.19 (up to 5 bar) 24.77 (up to 30 bar)	96.46 (up to 5 bar) 58.24 (up to 30 bar)	48.19 (up to 5 bar) 24.77 (up to 30 bar)	$[P_{(14)666}][DCA]$/ ZIF-8
CO_2	1199.77 (up to 4 bar) 140.47 (up to 30 bar)	106.80 (up to 4 bar) 21.86 (up to 30 bar)	1.06 (up to 5 bar) 1.70 (up to 30 bar)	-	
N_2	129.22 (up to 5 bar) 254.88 (up to 30 bar)	500 (up to 5 bar) 1000 (up to 30 bar)	129.22 (up to 5 bar) 254.88 (up to 30 bar)	500 (up to 5 bar) 1000 (up to 30 bar)	

Table B.6. Dual site Langmuir parameters (for CH_4 and N_2) and Freundlich model parameters (for CO_2) used for fitting the gas adsorption of phosphonium-based IL/CuBTC composite

	Parameters				
Gases	**A**	**B**	**C**	**D**	
CH_4	101.91 (up to 1 bar) 325.59 (up to 5 bar) 274.70 (up to 30 bar)	5.75 (up to 1 bar) 18.35 (up to 5 bar) 12.80 (up to 30 bar)	19.75 (up to 1 bar) 3.88 (up to 5 bar) 0.1 (up to 30 bar)	2.84 (up to 1 bar) 0.1 (up to 5 bar) 1.67 (up to 30 bar)	$[P_{4444}][TOS]$ / ZIF-8
CO_2	257.17 (up to 1 bar) 311.20 (up to 5 bar) 289.58 (up to 30 bar)	1.52 (up to 1 bar) 2.18 (up to 5 bar) 229.41 (up to 30 bar)	1.32 (up to 1 bar) 1.25 (up to 5 bar) 7.07 (up to 30 bar)	-	
N_2	396.94 (up to 1 bar) 207.33 (up to 30 bar)	81.39 (up to 1 bar) 38.35 (up to 30 bar)	1.81 (up to 1 bar) 10 (up to 30 bar)	0.43 (up to 1 bar) 38.47 (up to 30 bar)	

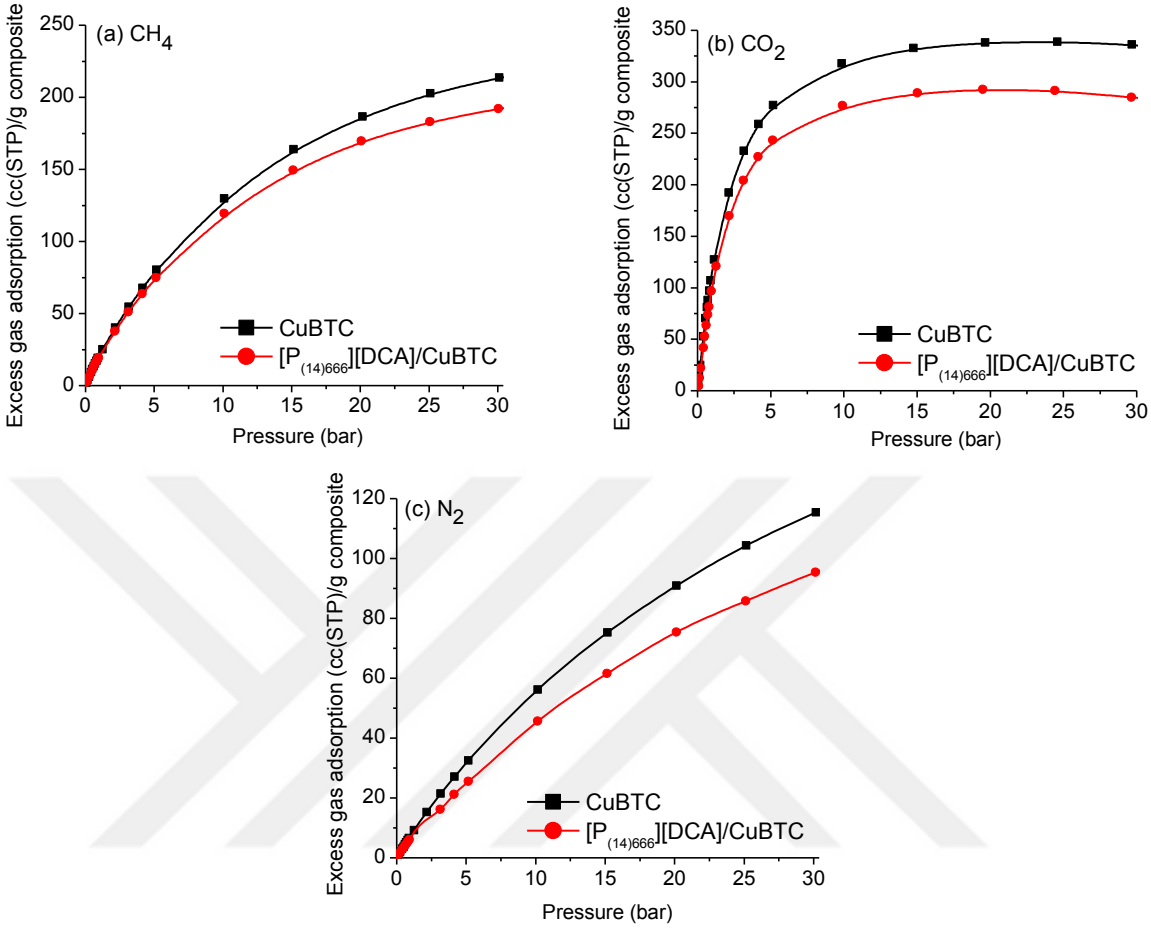

Figure B.6. Excess gas uptakes of $[P_{(14)666}][DCA]/CuBTC$ per gram of composite material

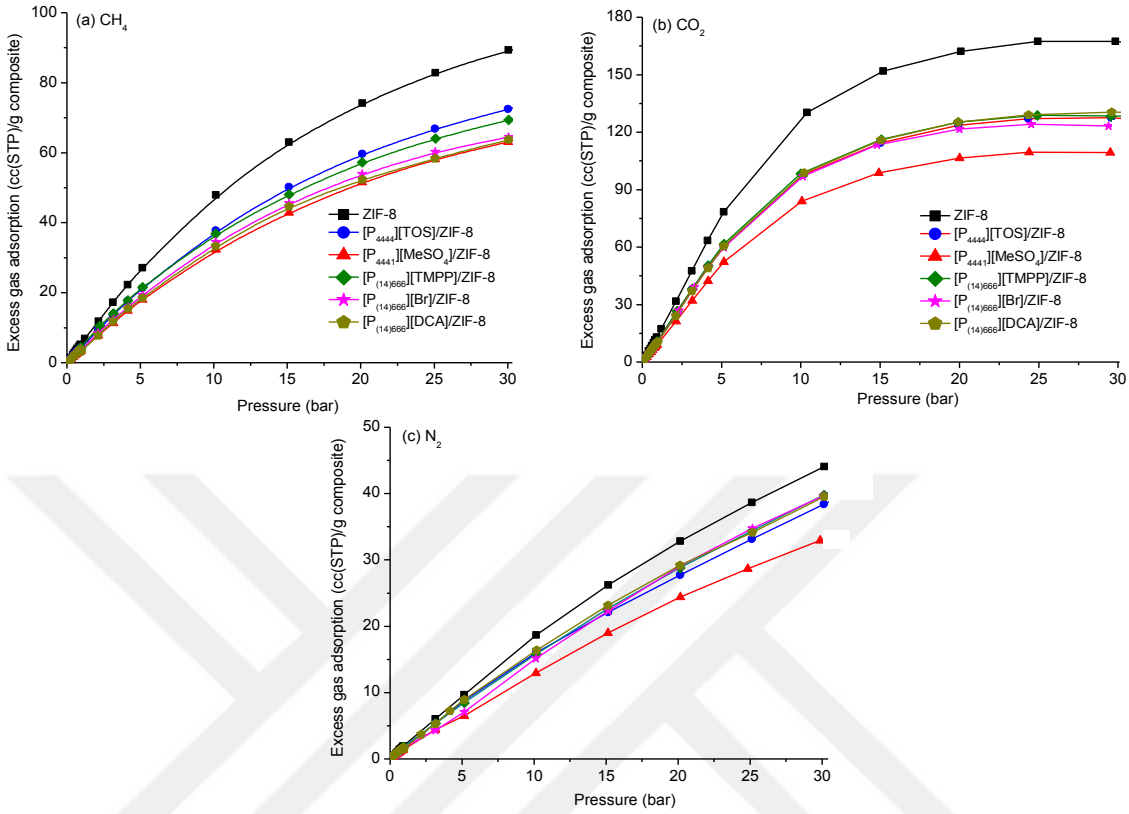

Figure B.7. Excess gas uptakes of phosphonium-based IL/ZIF-8 composites per gram of composite material

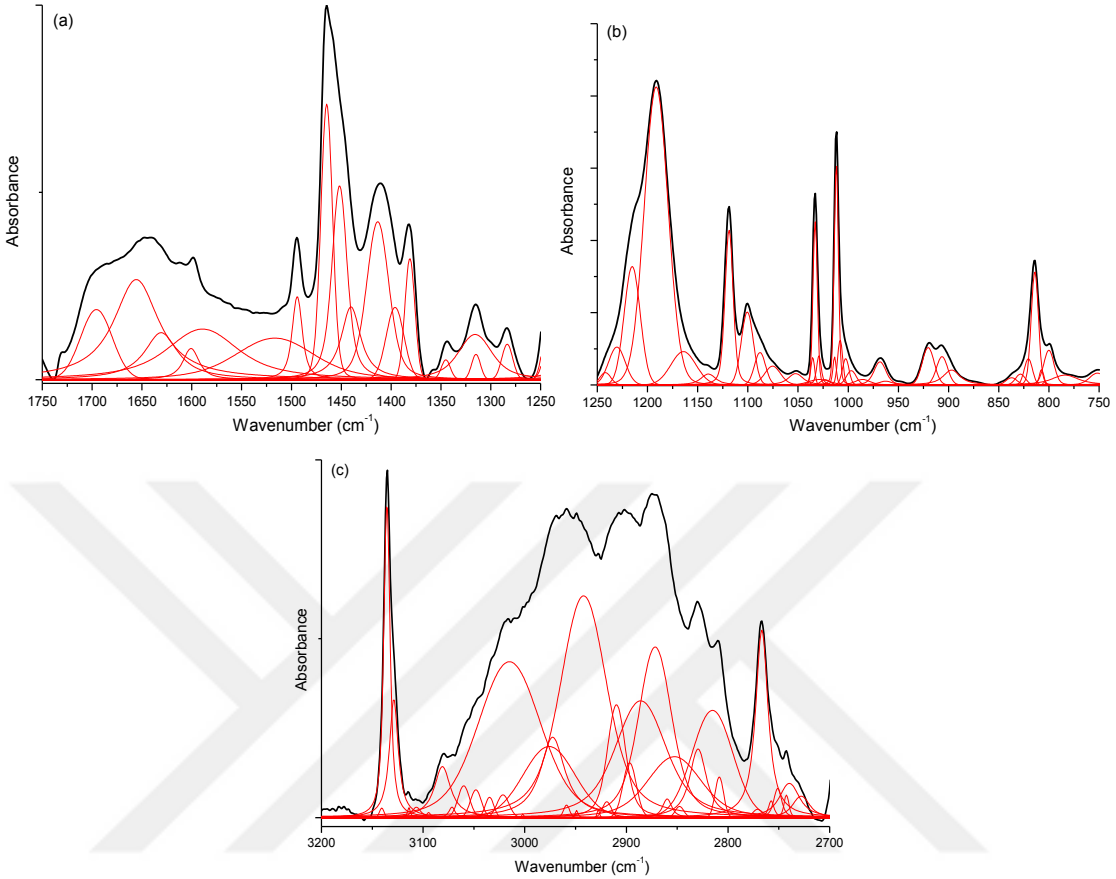

Figure B.8. Deconvoluted peaks of IR spectra of $[P_{4444}][TOS]$ in the regions (a) 1750-1250 cm^{-1}, (b) 1250-500 cm^{-1}, and (c) 3200-2700 cm^{-1}

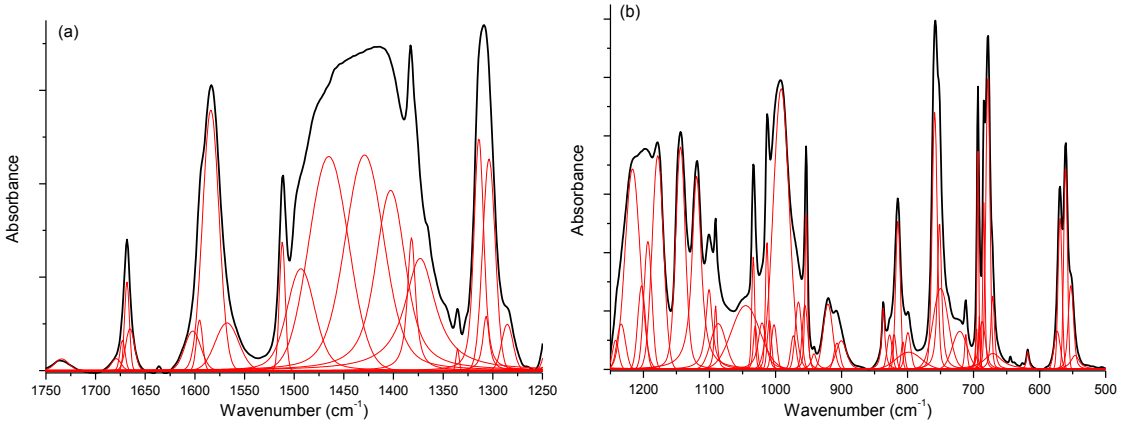

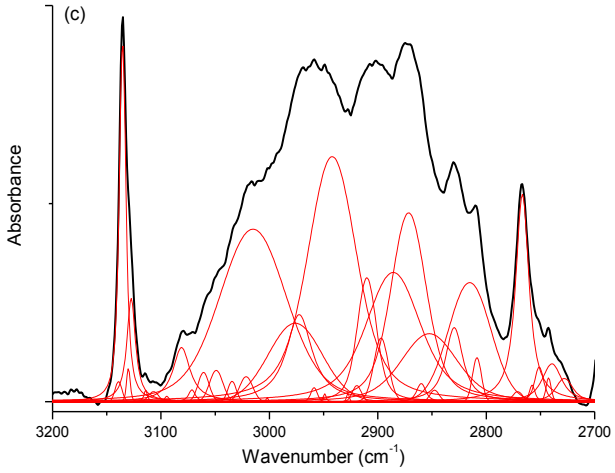

Figure B.9. Deconvoluted peaks of IR spectra of $[P_{4444}][TOS]$/ZIF-8 in the regions (a) 1750-1250 cm^{-1}, (b) 1250-500 cm^{-1}, and (c) 3200-2700 cm^{-1}

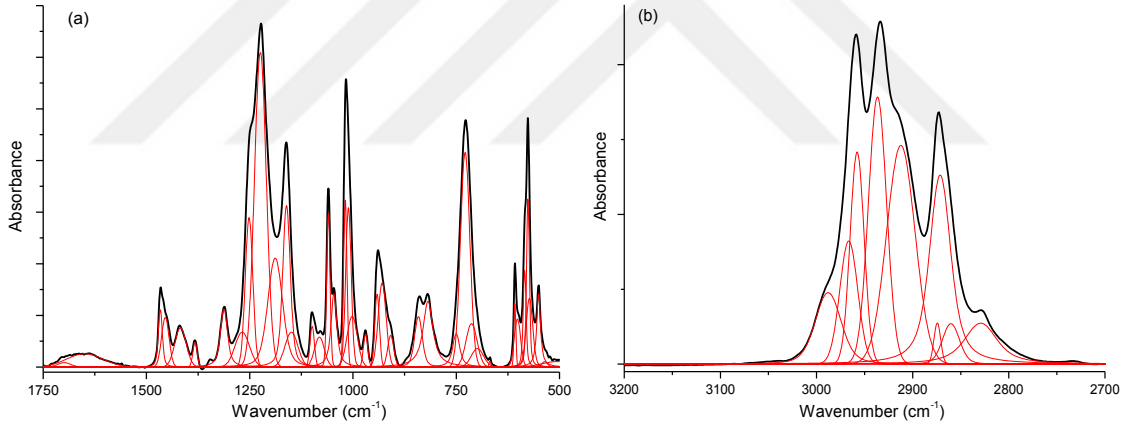

Figure B.10. Deconvoluted peaks of IR spectra of $[P_{4441}][MeSO_4]$ in the regions (a) 1750-500 cm^{-1}, and (b) 3200-2700 cm^{-1}

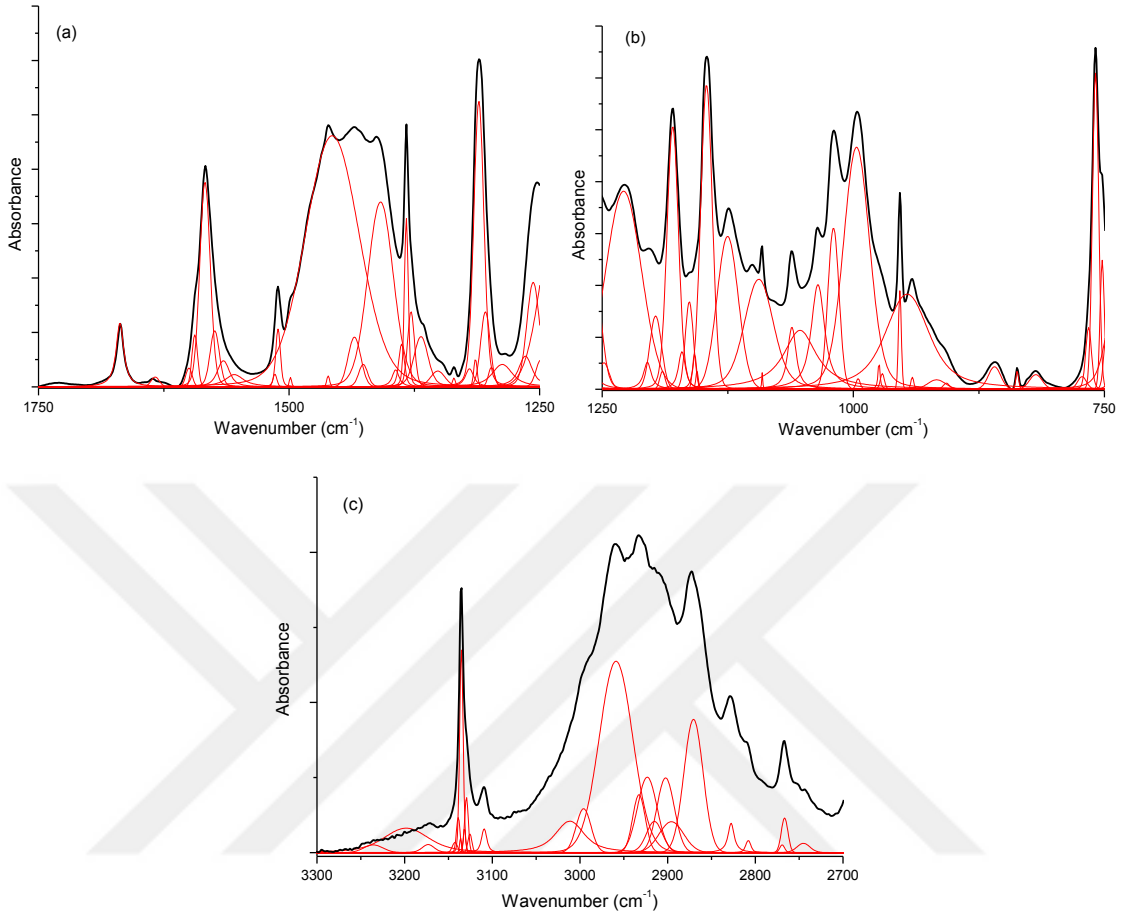

Figure B.11. Deconvoluted peaks of IR spectra of $[P_{4441}][MeSO_4]$/ZIF-8 in the regions (a) 1750-1250 cm^{-1}, (b) 1250-500 cm^{-1}, and (c) 3200-2700 cm^{-1}

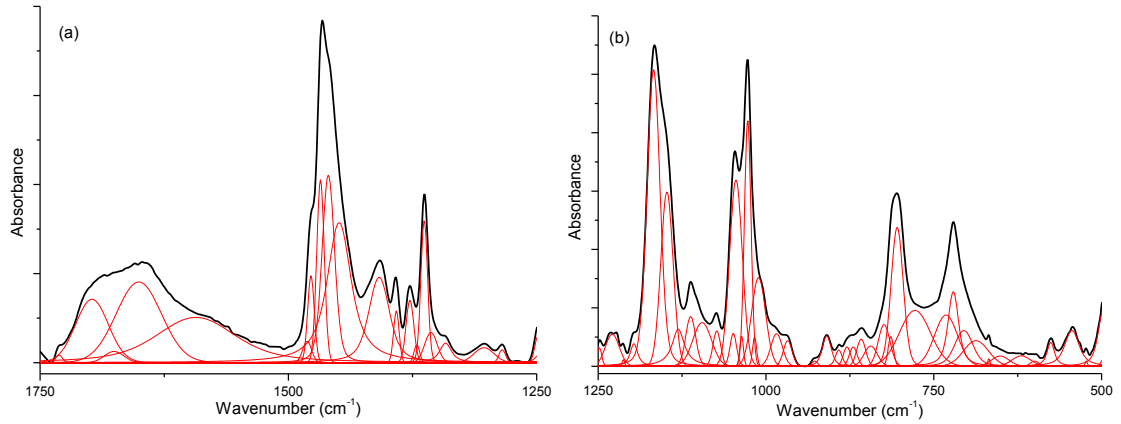

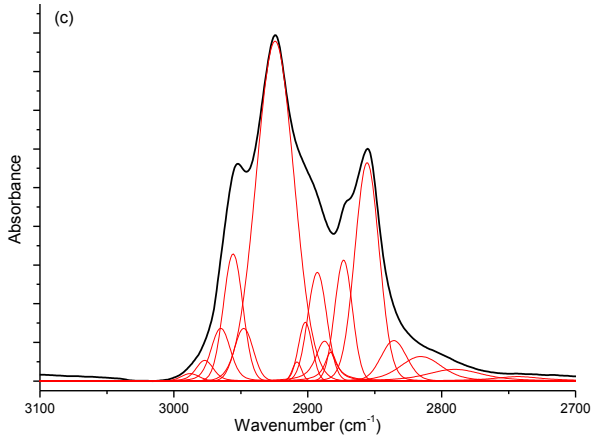

Figure B.12. Deconvoluted peaks of IR spectra of $[P_{(14)666}][TMPP]$ in the regions (a) 1750-1250 cm^{-1}, (b) 1250-500 cm^{-1}, and (c) 3100-2700 cm^{-1}

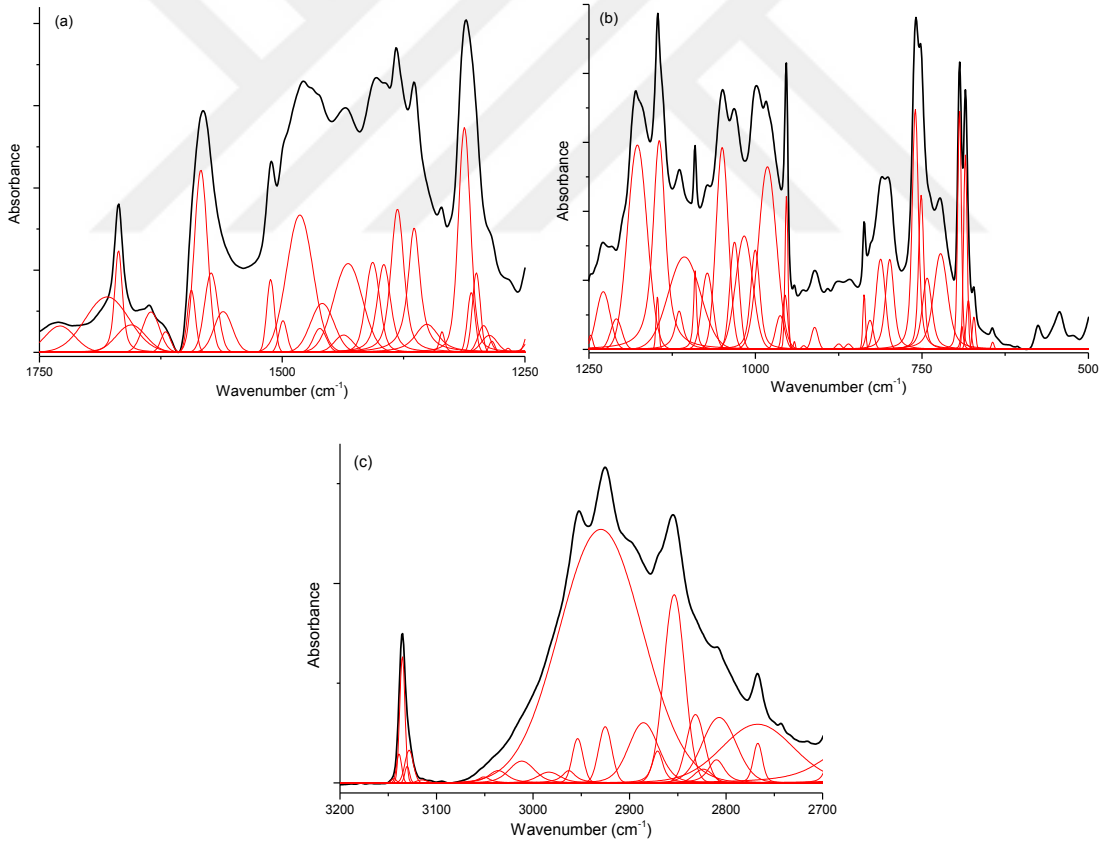

Figure B.13. Deconvoluted peaks of IR spectra of $[P_{(14)666}][TMPP]$/ZIF-8 in the regions (a) 1750-1250 cm^{-1}, (b) 1250-500 cm^{-1}, and (c) 3200-2700 cm^{-1}

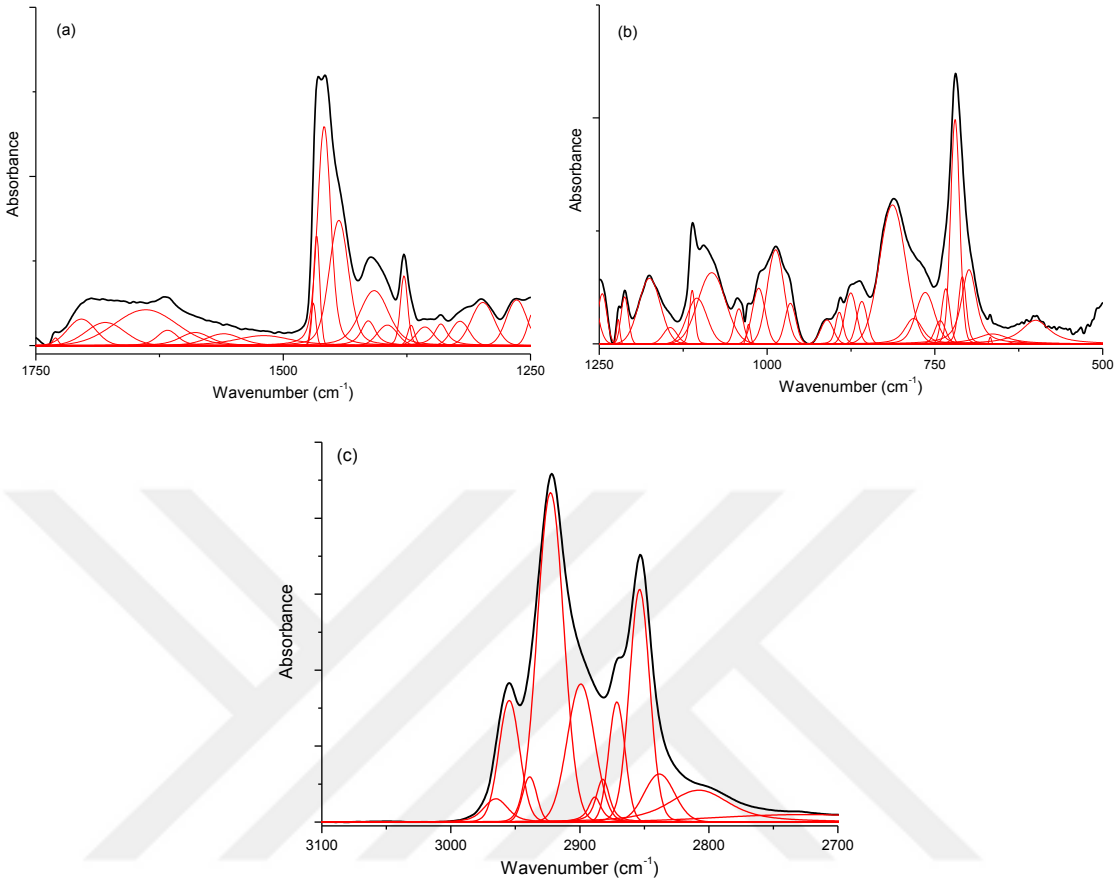

Figure B.14. Deconvoluted peaks of IR spectra of $[P_{(14)666}][Br]$ in the regions (a) 1750-1250 cm^{-1}, (b) 1250-500 cm^{-1}, and (c) 3100-2700 cm^{-1}

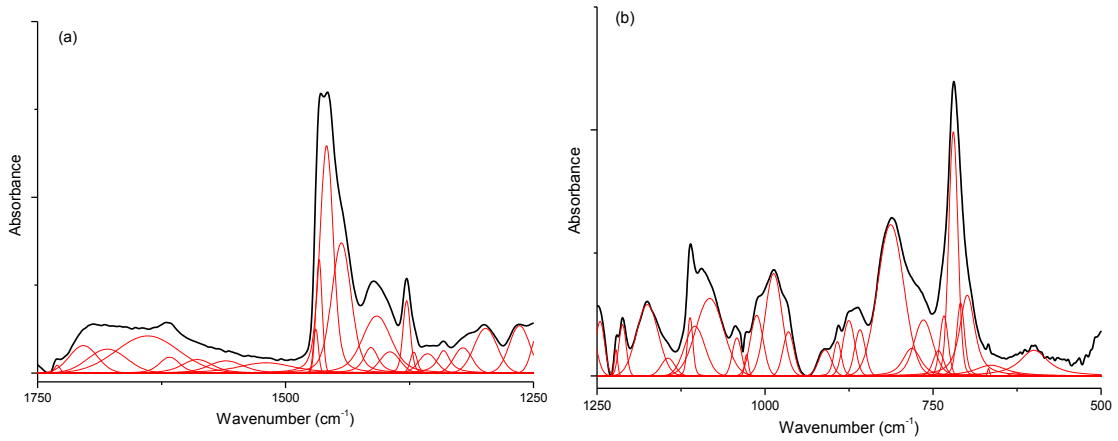

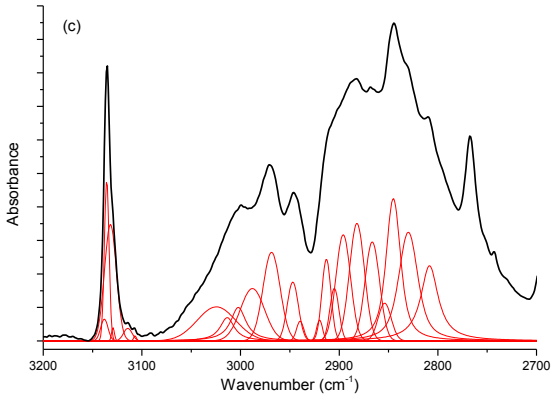

Figure B.15. Deconvoluted peaks of IR spectra of $[P_{(14)666}][Br]$/ZIF-8 in the regions (a) 1750-1250 cm^{-1}, (b) 1250-500 cm^{-1}, and (c) 3200-2700 cm^{-1}

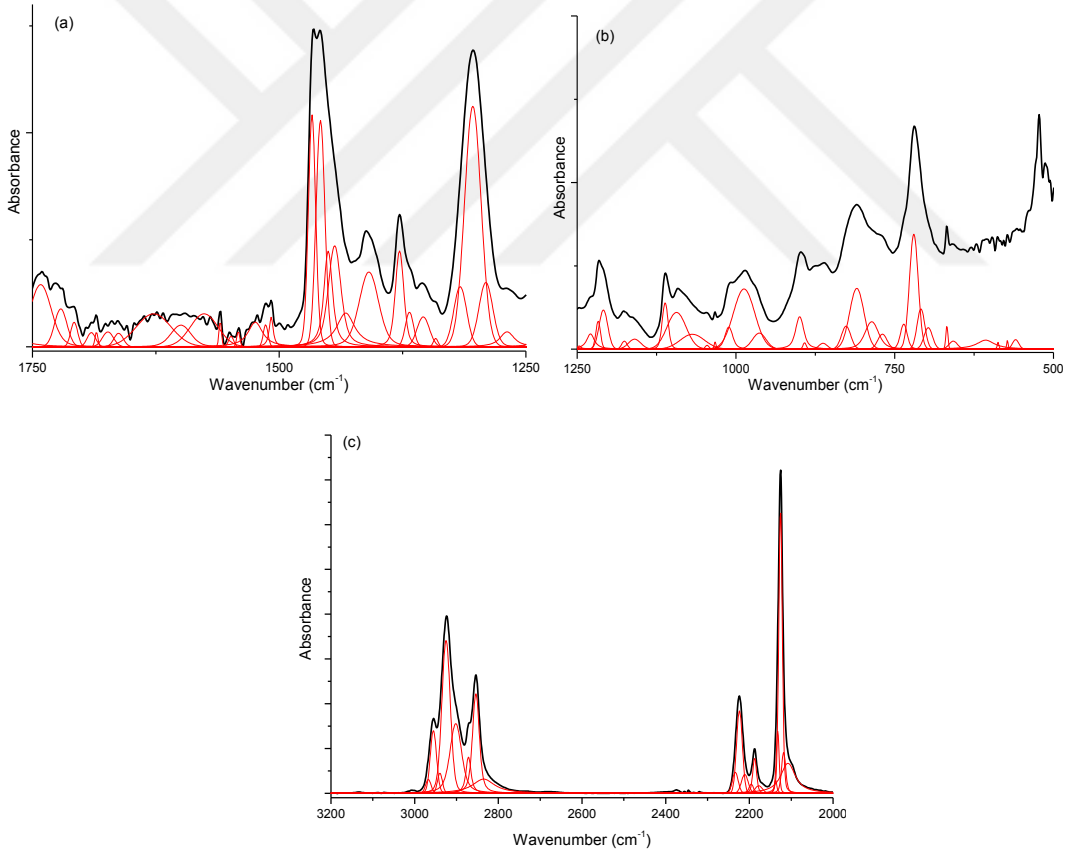

Figure B.16. Deconvoluted peaks of IR spectra of $[P_{(14)666}][DCA]$ in the regions (a) 1750-1250 cm^{-1}, (b) 1250-500 cm^{-1}, and (c) 3200-2700 cm^{-1}

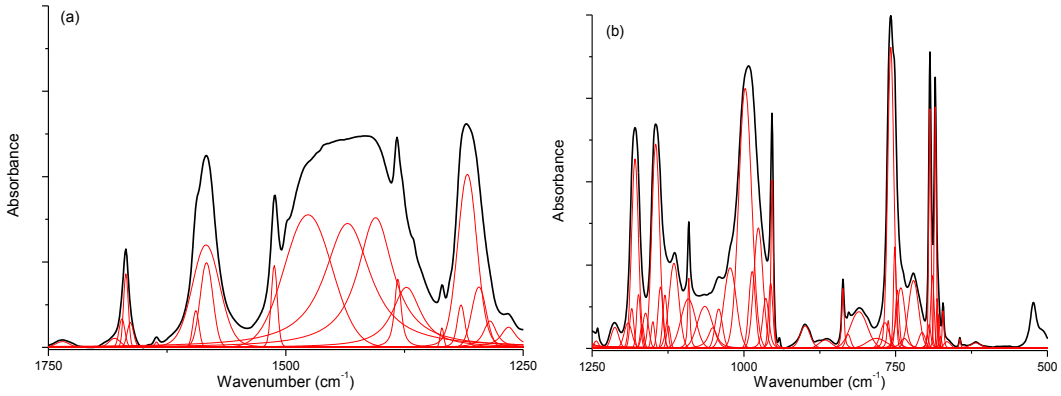

Figure B.17. Deconvoluted peaks of IR spectra of $[P_{(14)666}][DCA]$/ZIF-8 in the regions (a) 1750-1250 cm^{-1}, (b) 1250-500 cm^{-1}, and (c) 3200-2000 cm^{-1}

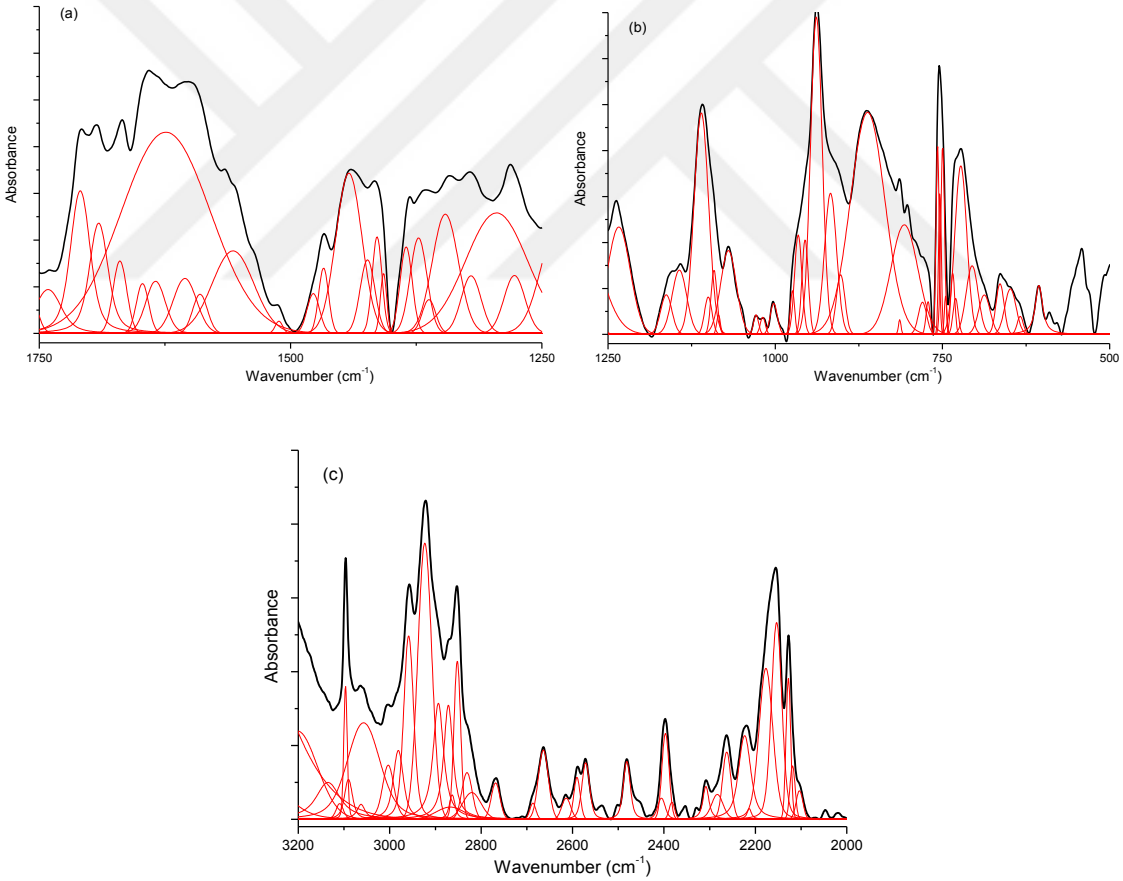

Figure B.18. Deconvoluted peaks of IR spectra of $[P_{(14)666}][DCA]$/CuBTC in the regions (a) 1750-1250 cm^{-1}, (b) 1250-500 cm^{-1}, and (c) 3200-2000 cm^{-1}

APPENDIX C: Full Names of Ionic Liquids

Table C.1. Full names of ionic liquids mentioned in this thesis.

IL Abbreviations	IL Full Name
[BMIM][BF_4]	1-butyl-3-methylimidazolium tetrafluoroborate
[BMIM][Tf_2N]	1-butyl-3-methylimidazolium bis(trifluoromethylsulfonyl)imide
[BMIM][PF_6]	1-butyl-3- methylimidazolium hexafluorophosphate
[BMIM][Cl]	1-butyl-3-methylimidazolium chloride
[BMIM][Br]	1-butyl-3-methylimidazolium bromide
[BMIM][DCA]	1-butyl-3-methylimidazolium dicyanamide
[BMIM][SCN]	1-ethyl-3-methylimidazolium thiocyanate
[EMIM][SCN]	1-ethyl-3-methylimidazolium thiocyanate
[EMIM][Tf_2N]	1-ethyl-3-methylimidazolium bis(trifluoromethylsulfonyl)imide
[EMIM][NO_3]	1-ethyl-3-methylimidazolium nitrate
[EMIM][$EtSO_4$]	1-ethyl-3-methylimidazolium ethyl sulfate
[EMIM][PF_6]	1-ethyl-3-methylimidazolium hexafluorophosphate
[EMIM][BF_4]	1-ethyl-3-methylimidazolium tetrafluoroborate
[P_{4444}][TOS]	tetrabutylphosphonium p-toluene sulfonate
[P_{4441}][$MeSO_4$]	tributylmethylphosphonium methyl sulfate
[$P_{(14)666}$][TMPP]	trihexyltetradecylphosphonium bis(2,4,4-trimethylpenthyl) phosphinate
[$P_{(14)666}$][Br]	trihexyltetradecylphosphonium bromide
[$P_{(14)666}$][DCA]	trihexyltetradecylphosphonium dicyanamide
[BuPy][Tf_2N]	n-butylpyridinium tetrafluoroborate

APPENDIX D: Full Names of Metal Organic Frameworks

Table D.1. Full names of metal organic frameworks mentioned in this thesis.

MOF Abbreviations	MOF Full Name
ZIF	Zeolitic imidazolate framework
CuBTC	Copper benzene-1,3,5-tricarboxylate
IRMOF	Isoreticular metal organic framework
UiO	Universitetet i Oslo
Cu-TPDAT	Copper-2,4,6-tris(3,5-dicarboxylphenylamino)-1,3,5-triazine
MIL	Materials Institute Lavoisier
ZMOF	Zeolite-like metal organic framework
Na-*rho*-ZMOF	Na-exchanged rho-ZMOF